ELECTRON BEAM SIZE DIAGNOSTICS USING DIFFRACTION AND TRANSITION RADIATION

By

Tamás Róbert Sashalmi

Dissertation

Submitted to the Faculty of the

Graduate School of Vanderbilt University

in partial fulfillment of the requirements

for the degree of

DOCTOR OF PHILOSOPHY

in

Physics

December, 2006

Nashville, Tennessee

Approved:

Prof. Steven E. Csorna

Prof. William E. Gabella

Prof. Thomas W. Kephart

Prof. Norman H. Tolk

ACKNOWLEDGEMENTS

First of all I would like to thank my advisor, prof. Steven E. Csorna, for his guidance and support during my graduate studies at Vanderbilt University. He is a great advisor not only in physics but in the field of the "real life".

I am grateful to Dr. Bibo Feng and Dr. William (Bill) E. Gabella for their help, comments and suggestions during my thesis work at the W.M. Keck FEL Center. They gave me an opportunity to study accelerator physics and they helped me to explore the field of beam diagnostics. This work would not have been possible without their support.

I am also grateful to the members of my PhD Committee, prof Thomas Kephart, prof Norman Tolk for their helpful comments, suggestions, and valuable questions.

I also thank all the members of the W. M. Keck FEL center for their help and support.

I also would like to thank everyone who made this part of my life possible and an enjoyable experience for me.

Finally, and most importantly, I would like to express my deepest gratitude to my fiancée, Gabi, for the constant support and love.

TABLE OF CONTENTS

LIST OF TABLES

LIST OF FIGURES

CHAPTER I

INTRODUCTION

1.1 Overview

This dissertation is a summary of our work on developing new beam monitoring methods for linear accelerators and free-electron lasers. We concentrated on the coherent diffraction radiation based beam monitoring technique and compare it with the well-known transition radiation method. We developed a movable slit to generate and to investigate the properties of diffraction radiation generated from various radiator configurations. In this thesis, we present a method to measure electron bunch length, longitudinal bunch profile, and we describe a few available methods to obtain transverse electron beam size and beam divergence using diffraction and transition radiation.

In Chapter I we detail the motivation behind our experiments and give a short overview of the existing techniques for beam size diagnostics: measuring longitudinal and transverse bunch sizes, beam divergence and beam energy.

Chapter II contains a review of the theoretical background of the transition and diffraction radiation processes used in our investigation. We overview the effects of the beam sizes on the angular distribution of diffraction radiation created by a single slit. We provide a description of coherent radiation as longitudinal bunch length measurement technique, and we give an introduction to Kramers-Kronig analysis

used to determine the longitudinal charge distribution of an electron bunch.

We introduce our test facility, the W.M Keck FEL Center at Vanderbilt University in Chapter III. We review the electron bunch generation along with Vanderbilt FEL beam properties. We describe our experimental setup of the bunch length measurement along with the setup of angular distribution measurement.

In Chapter IV we present our achievement in longitudinal bunch length measurements and our calculated longitudinal bunch profile of the Vanderbilt FEL. We demonstrate our method to reconstruct the charge distribution of the electron beam. We also show a quick method to obtain bunch length from the measured data.

Measured angular distribution of diffraction radiation generated from our movable slit is presented in Chapter V. The angular distribution of such radiation can be used to determine transverse beam sizes of electron beams. Our initial measurements of this method will be presented in this chapter.

Finally in Chapter VI we state our conclusion about coherent diffraction radiation based electron beam diagnostics and provide some ideas to improve and extend its usability.

1.2 Motivation

Modern experimental particle physics requires very high energy. At extreme energies, researchers anticipate significant discoveries that will lead to a radically new understanding of what the universe is made of and how it works. To provide this enormous, $\sim$TeV (10^{12} eV), energy there is a need for new particle colliders. In 2006

the new Large Hadron Collider (LHC) in CERN will begin to operate and create this energy by colliding two 7 TeV bunches of protons. The LHC is a two ring, 27 km long, superconducting accelerator and collider with center of mass collision energies of up to 14 TeV [1]. The number of events[1] per second generated in the LHC collisions is given by:

$$N_{event} = L \cdot \sigma_{event} \tag{1}$$

where L is the luminosity and σ_{event} is the total cross section of the studied physical process. The LHC ring is the home of two high luminosity experiments, ATLAS and CMS. The proton-proton collider will create a large amount of background interaction data due to the proton's complex structure. To avoid these difficulties a possible solution is to use elementary particles as colliding pairs, as in electron-positron collisions. The main problem with the use of electrons is that the energy loss due to synchrotron radiation in rings is huge therefore makes it an inefficient process. This energy loss can be avoided by using linear accelerators.

As we can see from (1), luminosity is one of the most important properties of any particle collider to generate new particles or processes. The luminosity by definition is the interaction rate per unit cross section and usually expressed in the CGS units of $cm^{-2}s^{-1}$. That is, high luminosity means better performance and a higher chance to discover new particles, and to confirm or dismiss theories. For colliders the luminosity is

$$L = f \times \frac{N_{e^-} N_{e^+}}{4\pi\sigma_x\sigma_y}, \tag{2}$$

[1]The term, event, means some interesting physical process, or production of new particles.

where N_{e^-} and N_{e^+} are the number of particles in a single bunch. $\sigma_{x,y}$ are the horizontal and vertical r.m.s. beam sizes at the interaction point and f is the repetition rate of bunch collisions. High luminosity is one of the goals of the new internationally proposed particle collider called the International Linear Collider or ILC (see Figure 1). The ILC will use electrons and positrons as colliding particles to create clean, easy to analyze experimental data. Even though the LHC will operate at higher energy than the ILC, with proposed center of mass energy around 800 GeV (Max. 1.0 TeV), it can provide more precise measurements and confirm or deny LHC discoveries. The expected discoveries are Higgs boson decays and perhaps proof of the SUSY theory. To discover and verify such new phenomena the highest luminosities will be required. Luminosity can be increased by decreasing the transverse beam sizes $\sigma_{x,y}$ of the accelerated particles. To control the beam size at the collision point, precise measurement of the beam size is needed at various locations of the beam line.

Accurate measurement of the longitudinal and transverse beam size of electron bunches and its charge distribution is also required to tune and operate a Free Electron Laser (FEL). Our research group at W. M. Keck FEL Center at Vanderbilt University is working to develop a suitable method to measure these beam parameters. Many different techniques are available or have been developed in recent years. Most of them are invasive, meaning that the measurement disturbs the beam; examples are transition radiation (TR) monitor or a wire scanner. To monitor the beam quality online, non-intercepting diagnostics are desired.

Our group decided to study two new techniques: diffraction radiation diagnostics

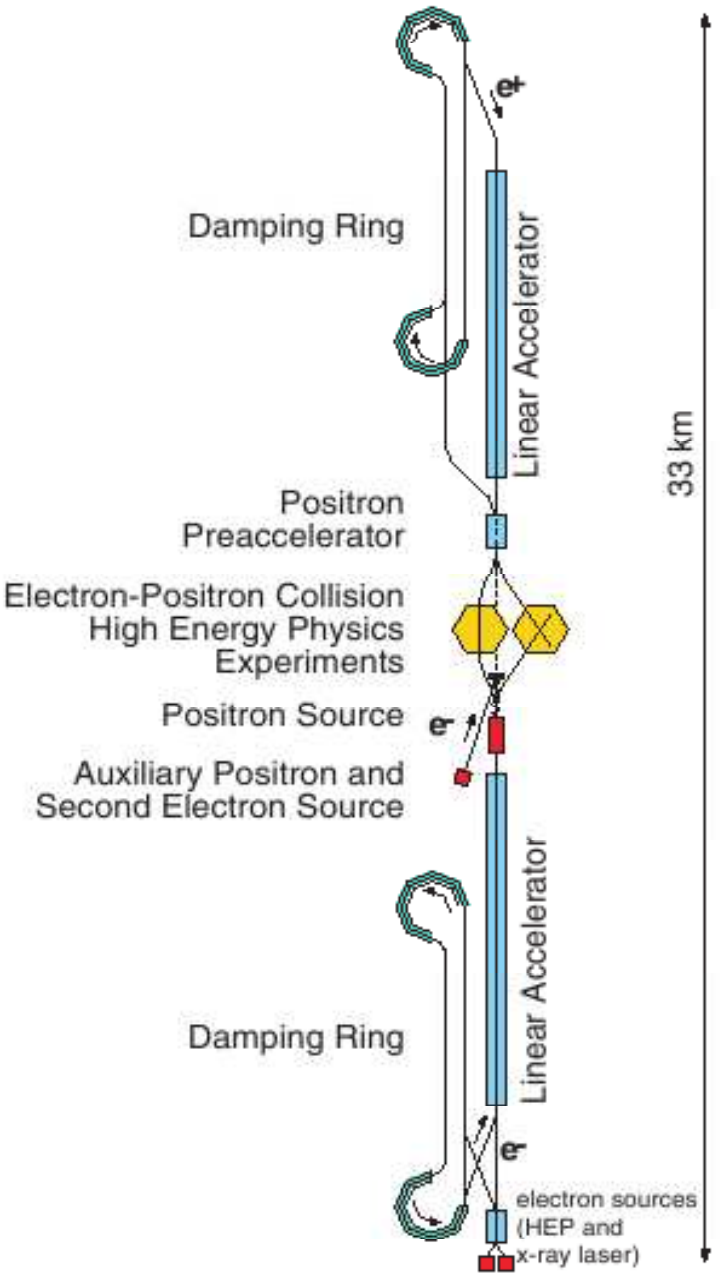

Figure 1: ILC schematic layout, TESLA design [2].

[3] and a method based on electro-optic effect [4]. By using diffraction radiation we are able to measure both the transverse and the longitudinal beam sizes, divergence and beam energy, while the electro-optic measurement is used to determine longitudinal bunch size and charge distribution.

The method to use coherent diffraction radiation generated by a slit, or slit systems is one of the most promising technique, since it allows measured longitudinal and transverse beam sizes along with beam divergence. Also diagnostic methods based on diffraction radiation are very similar to the well known and commonly used methods underlying transition radiation measurements [5, 6, 7].

1.3 Beam size measurement techniques

In this section we review the currently available methods to measure beam parameters. In general, the method of measuring longitudinal bunch sizes is completely different from obtaining the correspondent transverse beam sizes. Thus, in the following we will review first the most used techniques to measure transverse beam sizes, then we present some methods to determine longitudinal bunch lengths and/or longitudinal bunch charge distributions.

1.3.1 Transverse beam size measurements

Wire scanner

The wire scanner is one of the most available transverse beam size monitor device due to its simplicity [8, 9]. A very thin wire, usually 10 μm diameter gold plated tungsten, is moved across the beam path by a very high precision movement. Detecting the Bremsstrahlung photons produced by the electrons interacting with the thin wire can be used to measure the transverse beam profile. The number of photons is directly proportional to the number of electrons hitting the wire. The resolution of the beam profile depends strongly on the thickness of the wire. Due to the one dimensional scanning process the vertical and the horizontal beam size are measured separately. One of the disadvantages of the wire scanner is the slow scanning process, data is collected over many bunches, individual bunch size measurement is not available. At high energy, the damage to the wire could be a problem, particularly if continuous operation is required.

Laser wire scanners

The Laser Wire Scanner is considered one of the most convenient methods to measure transverse beam profiles. The basic idea comes from the wire scanner, but in this case a laser beam acts as the wire. The result of the collision of the particle beam and the laser light is Compton scattered photons. Detecting these photons one can easily determine transverse beam sizes. The change in the beam after the

collision is neglectable. The theoretical estimation for change in path of the electrons is about 10^{-6} rad [10].

The minimum beam size that can be measured with this method depends on the laser beam size at the interaction point. The laser beam size can be changed using laser interferometry. The laser beam is split to two, and front of the beam their crossing each other, creating an interference pattern front of the beam, see Figure 2. The period of the created standing wave, d, determined by the wavelength of the

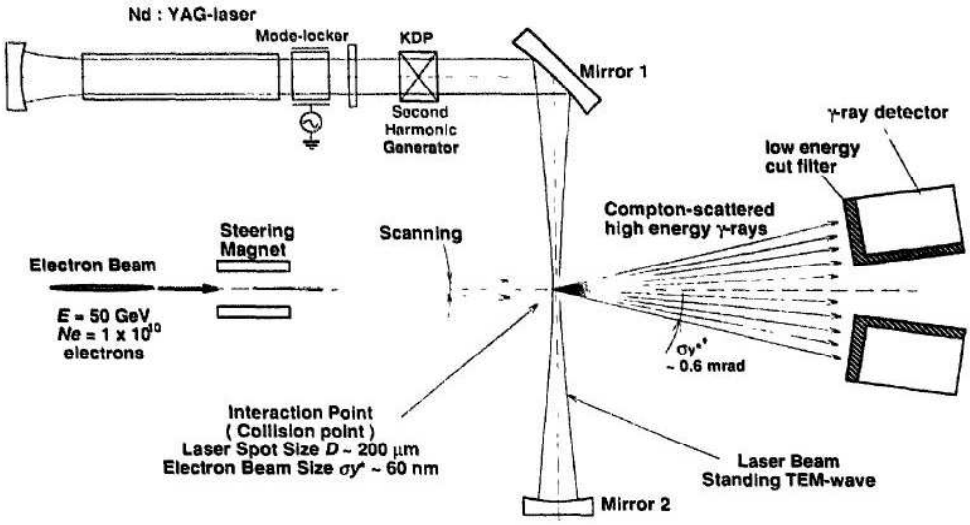

Figure 2: Using Laser interferometry nanometer beam size can be measured [11].

laser, λ, and the crossing angle, θ [11]:

$$d = \frac{\lambda}{2}\sin(\theta/2) \tag{3}$$

Using this method, nanometer beam sizes can be measured [12]. The laser beam size can be changed by the crossing angle. This method has so many positive properties,

but one of its disadvantages is same as for wire scanner, the long scanning process. Thus using this method to measure single shot beam parameters is not possible, in some cases this is deficiency.

Synchrotron radiation monitors

To avoid the drawbacks of the wire scanner, synchrotron radiation[2] can be used to determine the transverse beam size. Due to the physics of synchrotron radiation (SR), this technique works best in circular accelerators. The characteristic of the synchrotron radiation due to diffraction and depth of field limits the resolution of the SR imaging to 20 μm [13]. Recently the so-called SR interferometry (SRI) was developed to increase resolution, which uses two slits to create interference [14]. This interference increases the sensitivity of the synchrotron radiation to the transverse beam size. Around a few micron beam size measurement can be achieved with this simple method. SRI monitors are capable to measure bunch profiles on-line, but one stage can be used only to measure vertical or horizontal component, separately.

In 2001 we developed a software in a cooperative work with Cornell University to measure electron and positron vertical beam sizes at the same time continuously using SR interferometry. The front panel of this program is shown on Figure 3.

Using synchrotron radiation monitor in linear accelerators is not simple even if the beam is displaced by a magnet. The SR intensity in this case is very small compared to the intensity gain in a circular accelerator where the collection of the radiation can

[2]The radiation produced by transverse acceleration due to a perpendicular magnetic field **B** is called Synchrotron Radiation.

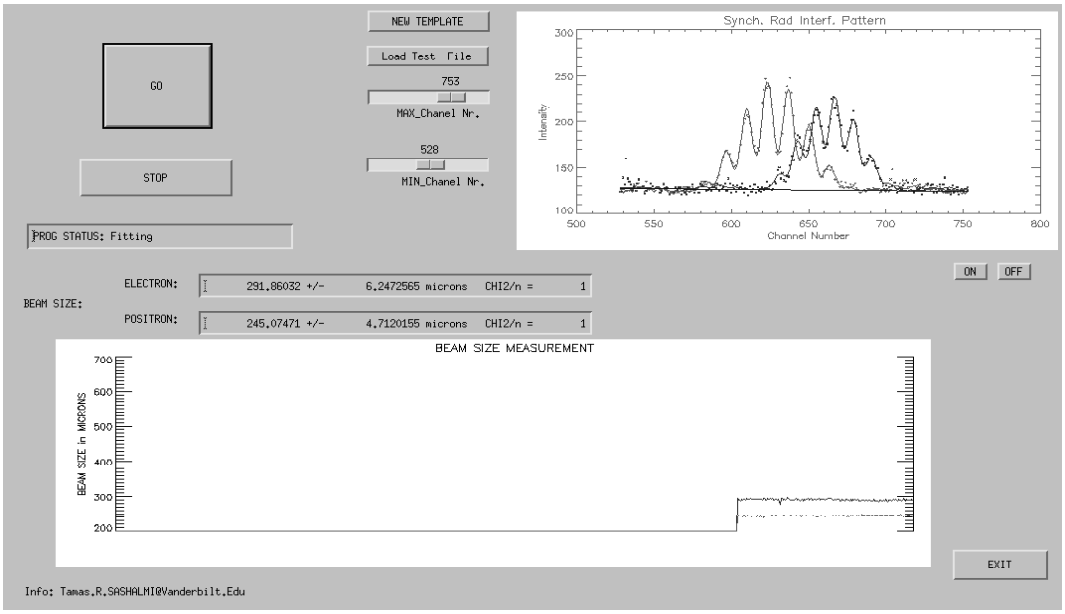

Figure 3: Syncro, the synchrotron radiation monitor program can provide simultaneously the beam vertical beam size of an electron and a positron bunch.

be made for multiple orbits as the electron bunch circulates in the beam line. Thus linear colliders and linear accelerators require a different method to obtain beam profiles online.

Optical transition radiation monitors

Optical Transition Radiation (OTR) monitors are also widely used to get transverse beam profiles in linear accelerators where the synchrotron radiation is not available or SR intensity is very small. Transition radiation (TR) is created when a charged particle crosses a boundary between two media, for example, from a vacuum into a conductor or a dielectric.

The intensity of TR is proportional to the square of γ, and it is peaked at the approximate angle $1/\gamma$, where γ is the charged particle's Lorentz factor,$\gamma = E_e/m_e c^2$.

To create this radiation usually a very thin metallic foil is used. Even so, this foil can disturb the beam and its thickness cannot be too small to prevent it from damage like melting [15]. The transition radiation is broadband and in many cases a simple optical CCD camera can be used as a detector. The transverse beam profile can then be obtained analyzing the shape of the recorded image. The biggest advantages of OTR is the instant measurement of 2D transverse beam profile for even one single bunch.

Diffraction radiation from a slit

Diffraction radiation is created by a charged particle passing by inhomogeneous boundaries, like a slit or a hole in a metallic screen. The radiation propagates in two main directions: along the beam trajectory (forward DR, FDR) and along the specular reflection direction (backward DR, BDR). The intensity of DR, like transition radiation, is proportional to the square of γ, and it is peaked at the approximate angle $1/\gamma$. If the DR radiation source is a slit, the angular distribution of the generated radiation depends on the transverse beam sizes, and beam divergence. Analyzing this angular distribution the vertical or the horizontal transverse beam size can be measured depending on the slit orientation [16]. Using two slits and their radiation interference, beam divergence along with transverse beam sizes can be measured [17].

Recently many groups around the world started to investigate the properties of the diffraction radiation to develop various methods to measure beam properties. Our group is one of them. The theoretical investigation of diffraction radiation started

over 40 years ago [18], however only a few experimental results are available so far [19, 20, 21].

1.3.2 Longitudinal bunch size and profile measurements

Streak camera

The classical way to measure longitudinal bunch size and profile is to use streak camera. A streak camera operates by transforming the profile of an emitted radiation pulse from the bunch into a spatial profile on a detector, by causing a time-varying deflection of the light across the width of the detector. The resulting image forms a "streak" of light, from which the length of the bunch can be inferred [22].

The emitted radiation can be synchrotron [23] or optical transition radiation [24], or even Cerenkov radiation using a laser wire [25].

One of the disadvantages of the streak camera is its high cost. Other disadvantages are related to radiation used to generate the light.

Coherent radiation based bunch length measurements

Coherent radiation generated from a bunch of particles can be used to measure longitudinal beam size and longitudinal beam profile.

The radiation from a bunched distribution of charges shows collective effects, which can raise the total number of radiated photons [26, 27]. For wavelengths longer than the bunch length the radiation created by the bunch is coherent, that is the

whole bunch radiates as a single, large charged particle. Using few approximations, one can show that the total energy of the radiation is proportional to the square of the number of particles:

$$W_{total}(\omega) = |f(\omega)|^2 N_e^2 \cdot W_{single}(\omega), \tag{4}$$

where $f(\omega)$ is the coherent function. By measuring this coherent function one can obtain the longitudinal bunch size and the longitudinal beam profile can be also determined.

Coherent radiation method works for many types of radiation which are created by a single particle in the bunch, such as transition radiation, synchrotron radiation [28], Smith-Purcell radiation or diffraction radiation [29, 30]. We will discuss this method further in Chapter II in the case of transition and diffraction radiation.

Smith-Purcell radiation

One radiation type listed above is worth discussing in more detail. The Smith-Purcell radiation is created in very special circumstances which is, in some senses, similar to the generation of diffraction radiation. When an electron beam passes close to the surface of a metallic grating, radiation is emitted called Smith-Purcell (S-P) radiation. The S-P radiation is due to the interaction of fields of the particle bunch with the periodic structure. The wavelength of the emitted radiation depends on the speed of the particles, β, the period of the grating, l, and the angle of the observation, θ, see Figure 4:

$$\lambda_{S-P} = \frac{l}{n}\left(\frac{1}{\beta} - \cos\theta\right) \tag{5}$$

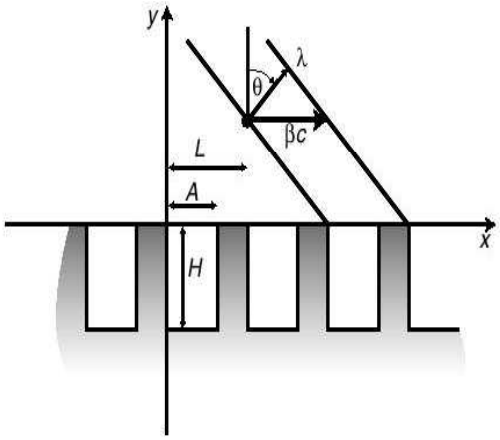

Figure 4: Formation of Smith-Purcell radiation by an electron moving parallel to the surface of a grating with rectangular grooves [31].

where n is the order of the radiation [32]. The angular distribution of the number of photons per electron radiated into the n^{th} order is

$$\frac{\mathrm{d}N}{\mathrm{d}\Omega} = \alpha\,|n|\,N_w \frac{\sin^2\theta \sin^2\Phi}{(1/\beta - \cos\theta\sin\Phi)^2}\,|R_n|^2 \times \mathrm{e}^{-\frac{d}{h_{int}}\sqrt{1+(\beta\gamma cos\Phi)^2}} \tag{6}$$

where α is the fine-structure constant, N_w the number of grating periods, and d the distance of the beam and the grating. θ and Φ are the emission angles. In (6), $|R_n|^2$ the radiation factor, which are analogous to the reflection coefficients of optical gratings, is a measure for the grating efficiency. In (6) the interaction length

$$h_{int} = \frac{\lambda\beta\gamma}{4\pi}$$

describes the characteristic finite range of the virtual photons emitted and absorbed by the electrons. By measuring the emitted photons, the longitudinal beam size can be determined [32, 33].

Electro-optic beam size measurements

The Electro-Optic beam size measurement is based on the Pockels effect, also called the electro-optic effect, that is, when in certain type of crystals birefringence[3] is induced due to an external electromagnetic field.

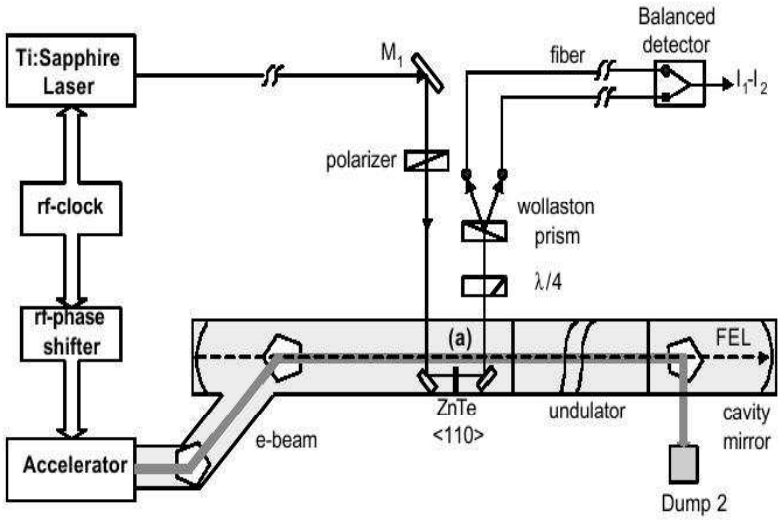

Figure 5: Experimental setup of the electro-optic measurement of the shape of relativistic bunches [34].

The electric field of a relativistic electron bunch is concentrated perpendicular to its direction of motion. This electric field can be used to create the Pockels effect in a electro-optic crystal, e.g. ZnTe, placed very close to the beam line. Then the induced birefringence can be measured by monitoring the change of polarization of a laser pulse. The induced birefringence causes the initially linearly polarized laser light, e.g.

[3]Birefringence, or double refraction, is the decomposition of a ray of light into two rays (the ordinary ray and the extraordinary ray) when it passes through certain types of material, such as calcite crystals, depending on the polarization of the light [22].

Ti:Sapphire (Ti:S) laser pulse, to acquire a phase difference between its polarization components. This phase difference then can be measured by using polarization optics. This phase will change according to the applied local electric field, that is, the electron bunch profile can be measured [34]. An experimental setup of such an electro-optic beam size monitor can be seen on Figure 5.

A single-shot electro-optic bunch shape monitor is under development at the Vanderbilt University W. M. Keck FEL center [4], parallel with a diffraction monitor, which is the subject of this thesis.

CHAPTER II

THEORETICAL APPROACH

In the following few sections we review the theory of transition and diffraction radiation generation by single charge or an electron. We will use two different approaches: the mirror charge method and the virtual photon method. As we will see the later one is very powerful tool to obtain radiation properties from any arbitrary targets.

After completing the theory of diffraction and transition radiation generation from single charged particle we discus the collective radiation generation from a bunch of these particles. We will see how the coherent radiation can be used for bunch length and profile measurements. We will also discus the theory behind the transverse beam size and divergence measurements.

2.1 Transition radiation

When a charged particle crosses a boundary between two media (for example from a vacuum into a conductor or a dielectric) it emits radiation as shown in Figure 6. This radiation is called transition radiation (TR) and it was first predicted by Ginzburg and Frank [35] in 1945. In the vacuum, or in some media, the charged particle has certain field characteristic of its motion and of that medium. In the other media this characteristic will be different if the electromagnetic properties of

the second media are not the same as in the original medium. When the particle crosses the boundary of the media, the fields must be rebuilt to the new pattern. During this process some pieces of the fields are shaken off as transition radiation [36]. A very detailed description of such a radiation can be found in Ter-Mikaelian's book [37], however we will describe it using two simplified methods.

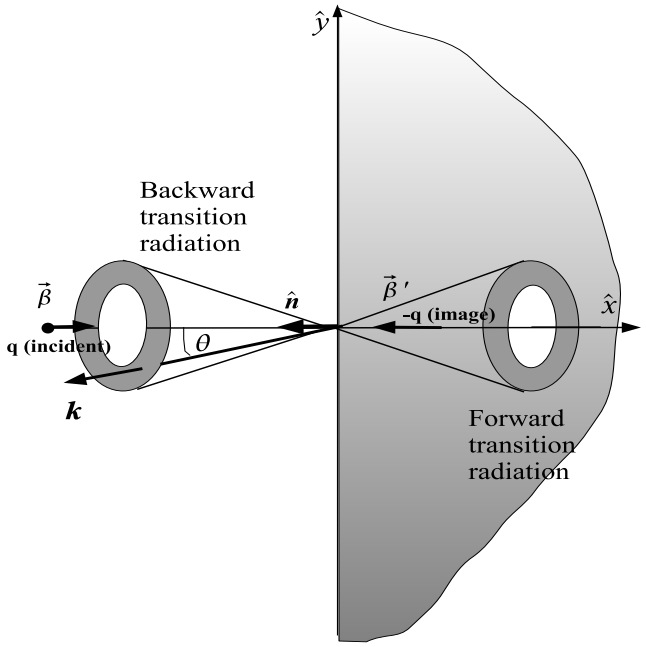

Figure 6: Transition radiation process and the method of image charge.

The process of transition radiation can be viewed as a collision of the particle with its image charge as show in Figure 6. When a charged particle is located in front of a conducting surface the electric field in the vacuum can be obtained by replacing the conductor with an image charge at the mirror image position where the surface

of the conductor is the plane of the symmetry. In a sense one can say that, the radiation, which is created by the actual charge is called forward transition radiation (FTR), while the radiation created by the image charge is called backward transition radiation (BTR) as shown in Figure 6.

Following Brau's discussion [38], the angular spectral fluence of the transition radiation in the $\hat{\mathbf{n}}$ direction can be obtained by the sum of the fields of the two charges:

$$\frac{\mathrm{d}^2W}{\mathrm{d}\omega\,\mathrm{d}\Omega} = \frac{q^2\omega^2}{16\pi^3\varepsilon_0 c}\left|\int_{-\infty}^{0}\mathrm{d}t\,\mathrm{e}^{i\omega(t-\hat{\mathbf{n}}\mathbf{r}/c)}\hat{\mathbf{n}}\times\boldsymbol{\beta} - \int_{-\infty}^{0}\mathrm{d}t\,\mathrm{e}^{i\omega(t-\hat{\mathbf{n}}\mathbf{r}'/c)}\hat{\mathbf{n}}\times\boldsymbol{\beta'}\right|^2, \qquad (7)$$

where the primes refer to the image charge and the particle reaches the surface at $t = 0$. The second term in the exponent becomes $\mathbf{n}\mathbf{r}/c = \mathbf{n}\boldsymbol{\beta}t$, since the velocity vectors are constant. After integrating (7), we get

$$\frac{\mathrm{d}^2W}{\mathrm{d}\omega\,\mathrm{d}\Omega} = \frac{q^2}{16\pi^3\varepsilon_0 c}\left|\frac{\hat{\mathbf{n}}\times\boldsymbol{\beta}}{1-\hat{\mathbf{n}}\cdot\boldsymbol{\beta}} - \frac{\hat{\mathbf{n}}\times\boldsymbol{\beta'}}{1-\hat{\mathbf{n}}\cdot\boldsymbol{\beta'}}\right|^2. \qquad (8)$$

It is important to note that the calculated fluence is independent of the frequency. This is true only in the case of a perfect conductor what we have considered. For most metals, this approximation is good at microwave and infrared frequencies but fails in the ultraviolet and beyond due to their metallic response. The acceptable frequency range is $f_{\text{skin depth}} < f \ll f_{\text{plasma}}$, due to the skin depth (minimum frequency) and the metallic response (maximum frequency). For instance, using 1.0 μm thick gold layer, this frequency range is 6.0 GHz-13.8 PHz (wavelength of 0.05m - 2.2×10^{-8}m). In the ultra-relativistic limit ($\beta \approx 1$), the denominators become very small in the forward

directions and the radiation peaks there

$$\frac{\mathrm{d}^2W}{\mathrm{d}\omega\,\mathrm{d}\Omega} = \frac{q^2}{16\pi^3\varepsilon_0 c}\left|\frac{\hat{\mathbf{n}}\times\boldsymbol{\beta'}}{1-\hat{\mathbf{n}}\cdot\boldsymbol{\beta'}}\right|^2. \tag{9}$$

Using the small angle approximation and $\beta \approx 1 - \frac{1}{2\gamma^2}$ as well as the $1 - \hat{\mathbf{n}}\cdot\boldsymbol{\beta'} \approx 1 - \frac{1}{2\gamma^2}(1+\gamma^2\theta^2)$ we get the following expression for the angular spectral fluence

$$\frac{\mathrm{d}^2W}{\mathrm{d}\omega\,\mathrm{d}\Omega} = \frac{\gamma^4 q^2}{4\pi^3\varepsilon_0 c}\frac{\theta^2}{(1+\gamma^2\theta^2)^2}. \tag{10}$$

The (10) equation indicates that there is no radiation in the forward direction, $\theta = 0$, and the intensity reaches its maximum at $\theta \approx \pm 1/\gamma$ where γ is the Lorentz factor,$\gamma = \sqrt{1-\beta^2}$. The obtained angular spectral fluence distribution is shown in Figure 7. Note that the radiation in case of normal incidence has azimuthal symmetry since it does not depend on ϕ.

2.1.1 Method of virtual quanta

The same description can be obtained by using the method of virtual quanta also described in [38]. This method in the most cases is much simpler and easier to implement than the previous theory. We will use this method in the diffraction radiation section as well.

The electric field of an electron moving at an ultrarelativistic speed ($\gamma \gg 1$) has a special behavior. Since the electric and magnetic fields are Lorentz contracted in the direction of motion, the created field is very similar to the field of a photon. This equivalence between the relativistic electron's field and a photon pulse is also known as the Weizsaker-Williams approximation. The Fourier transformations of the

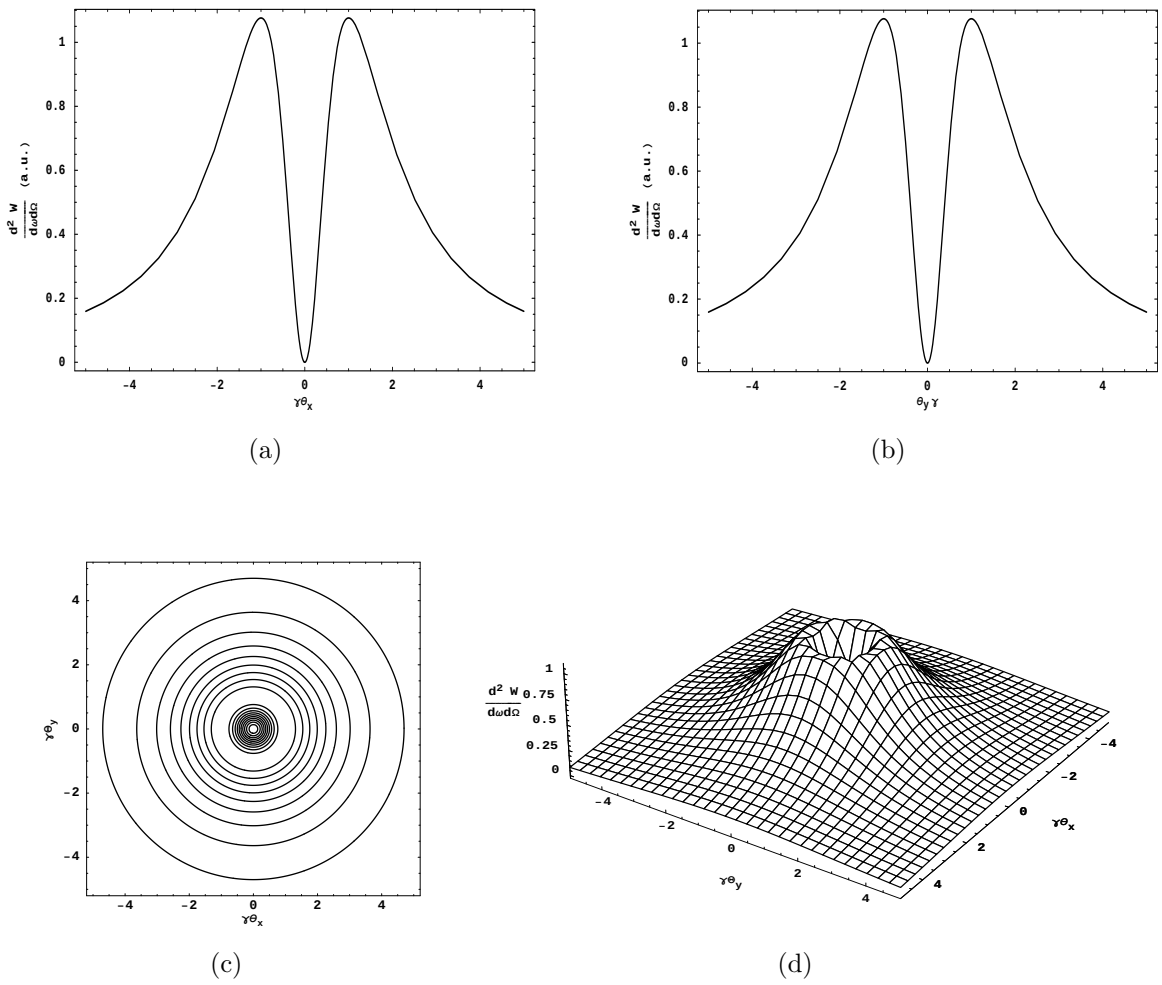

Figure 7: Transition radiation angular distribution at normal incidence. The pictures on the top show the horizontal (a) and the vertical (b) polarization components of the angular distribution of TR. The (c) and (d) pictures show the total radiation angular distribution. Note the azimuthal symmetry.

electron fields are called "virtual quanta". The Fourier decomposition of the field of a relativistic charge can be used to describe the transition radiation. First we expand the electric field into its Fourier components

$$\mathbf{E}(\mathbf{r},\mathbf{t}) = \frac{1}{(2\pi)^{3/2}}\frac{1}{\gamma}\int_{-\infty}^{\infty} \mathrm{d}^3\mathbf{k}\,\mathrm{e}^{-ik^a r_a}\tilde{\mathbf{E}}(\mathbf{k}), \tag{11}$$

where $k^a = (\omega/c, \mathbf{k})$ and $r_a = (ct, -\mathbf{r})$. The Fourier transforms of the electric field

components in (11) are

$$\tilde{E}_x(\mathbf{k},\omega) = \frac{i}{(2\pi)^{3/2}}\frac{q}{\varepsilon_0}\frac{\dfrac{\omega}{\gamma c}}{\dfrac{\omega^2}{\beta^2\gamma^2c^2} + k_y^2 + k_z^2} \tag{12}$$

and

$$\tilde{E}_{y,z}(\mathbf{k},\omega) = \frac{i}{(2\pi)^{3/2}}\frac{q}{\varepsilon_0}\frac{\gamma k_{y,z}}{\dfrac{\omega^2}{\beta^2\gamma^2c^2} + k_y^2 + k_z^2}. \tag{13}$$

In this method the transition radiation is the specular reflection of the incident virtual quanta at the interface of the medium. For perfect conductor, the entire radiation field is reflected. Therefore the total energy in the field can be obtained by

$$W = \int_{-\infty}^{\infty} \mathrm{d}^3\mathbf{r}\left(\frac{\varepsilon_0}{2}\mathbf{E}\cdot\mathbf{E} + \frac{1}{2\mu_0}\mathbf{B}\cdot\mathbf{B}\right). \tag{14}$$

In the ultra-relativistic limit the fields are very nearly electromagnetic waves as we mentioned earlier so the electric and magnetic part to the energy is equal. In this case we can use the expression for the total energy

$$W = \varepsilon_0\int_{-\infty}^{\infty} \mathrm{d}^3\mathbf{r}\mathbf{E}\cdot\mathbf{E}^*. \tag{15}$$

Inserting (11) into (15) we get

$$W = \frac{\varepsilon_0}{(2\pi)^3}\frac{1}{\gamma^2}\int_{-\infty}^{\infty}\mathrm{d}^3\mathbf{r}\int_{-\infty}^{\infty}\mathrm{d}^3\mathbf{k}\int_{-\infty}^{\infty}\mathrm{d}^3\mathbf{k}'\tilde{\mathbf{E}}(\mathbf{k})\tilde{\mathbf{E}}(\mathbf{k}')\,\mathrm{e}^{-i(k^a-k'^a)r_a}. \tag{16}$$

Using the Fourier transform fields (12) and (13) and then integrate over $\mathrm{d}^3\mathbf{r}$ and $\mathrm{d}^3\mathbf{k}'$ we obtain the total radiated energy as

$$W = \frac{q^2}{8\pi\varepsilon_0}\int_{-\infty}^{\infty}\mathrm{d}^3\mathbf{k}\frac{k_y^2+k_z^2}{\left(\dfrac{\omega^2}{\beta^2\gamma^2c^2} + k_y^2 + k_z^2\right)^2}\ . \tag{17}$$

Since in the ultra-relativistic limit $\omega \approx k_x c \approx kc$ and $\mathrm{d}^3\mathbf{k} = k^2 \mathrm{d}k\mathrm{d}\Omega$, and integrating over the possible frequencies, the total radiated energy can be written as

$$W = \frac{\gamma^4 q^2}{4\pi^3 \varepsilon_0 c} \int_0^\infty \mathrm{d}\omega \int_{2\pi} \mathrm{d}\Omega \frac{\theta^2}{(1+\gamma^2\theta^2)^2}, \tag{18}$$

where $\theta \approx \sin\theta = \frac{\sqrt{k_y^2+k_z^2}}{k}$. Comparing the obtained total radiated energy with Equation (10), one can see the two methods, virtual quanta and the method of images, yields to the same radiation fluence at normal incidence.

In more general case when the dielectric constant of the target is ϵ and the charge is moving from vacuum into this media, the angular distribution of the backward transition radiation is [39]

$$\begin{aligned} \frac{\mathrm{d}W}{\mathrm{d}\Omega \mathrm{d}\omega} =& \frac{q^2\beta^2}{16\pi^3 c\varepsilon_0} \frac{\sin^2\theta\cos^2\theta}{(1-\beta^2\cos^2\theta)^2} \\ & \times \left| \frac{(\epsilon-1)(1-\beta^2+\beta\sqrt{\epsilon-\sin^2\theta})}{(1+\beta\sqrt{\epsilon-\sin^2\theta})(\epsilon\cos\theta+\sqrt{\epsilon-\sin^2\theta})} \right|^2 . \end{aligned} \tag{19}$$

2.1.2 The transition radiation in the case of slant incidence

The transition radiation in the case of slant incidence (Ψ) has an additional component. As a consequence, the radiation has two polarized components. One has an electric field lying in the radiation plane, parallel ($\parallel$) and the second is perpendicular to it ($\perp$). In the case of normal incidence the radiation has only one component which is parallel to the radiation plane and due to the symmetry in the radiation planes, the radiation is radially polarized. The detailed derivation for oblique incidence can be found in [37]. The slant incidence is common in real TR experiments, since in this case the BTR will be radiated perpendicular to the beam line, so the BTR can be

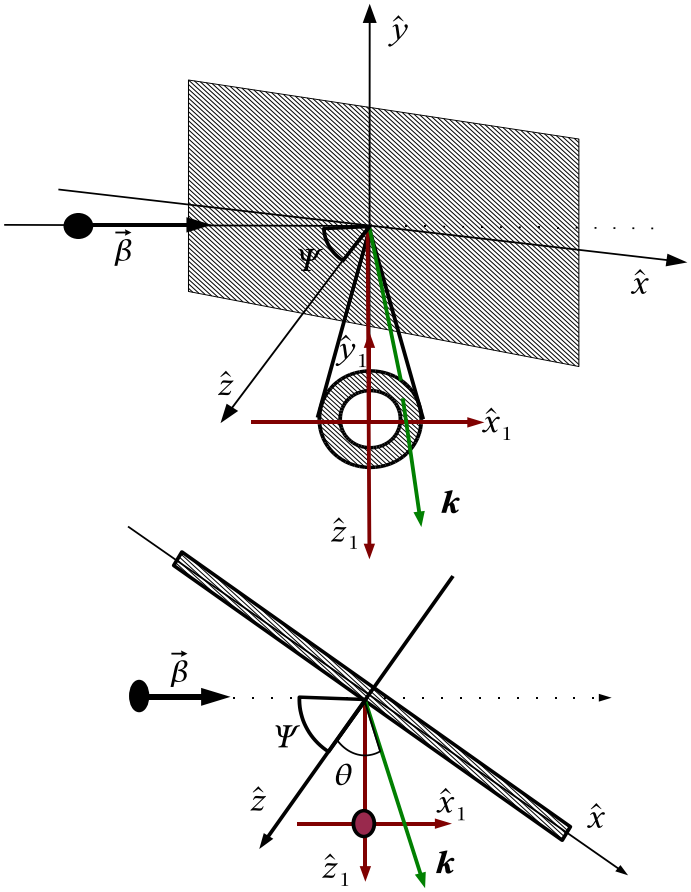

Figure 8: Transition backward radiation at Ψ-incidence, side and top view.

measured, see Figure 8.

The total radiation intensity contributed from the parallel and the perpendicular polarization components can be expressed as

$$\frac{\mathrm{d}W}{\mathrm{d}\Omega\mathrm{d}\omega} = \frac{\mathrm{d}W_{\perp}}{\mathrm{d}\Omega\mathrm{d}\omega} + \frac{\mathrm{d}W_{\parallel}}{\mathrm{d}\Omega\mathrm{d}\omega}\,. \tag{20}$$

In the above equation the two components of the radiated spectral fluence for the case of a perfect conductor are

$$\frac{\mathrm{d}W_{\perp}}{\mathrm{d}\Omega\mathrm{d}\omega} = \frac{q^2\beta^2\cos^2\Psi}{16\pi^3\varepsilon_0 c}\left[\frac{\sin\theta - \beta\cos\phi\sin\Psi}{(1-\beta\sin\theta\cos\phi\sin\Psi)^2 - \beta^2\cos^2\theta\cos^2\Psi}\right]^2 \tag{21}$$

and

$$\frac{\mathrm{d}W_{\parallel}}{\mathrm{d}\Omega \mathrm{d}\omega} = \frac{q^2\beta^2\cos^2\Psi}{16\pi^3\varepsilon_0 c}\left[\frac{\beta\cos\theta\sin\phi\sin\Psi}{(1-\beta\sin\theta\cos\phi\sin\Psi)^2-\beta^2\cos^2\theta\cos^2\Psi}\right]^2, \tag{22}$$

where θ is the angle between the direction of emitted radiation $\mathbf{k}$ and the $\hat{z}$ axis, while ϕ is the azimuthal angle defined in the $\hat{x}\hat{y}$ plane with respect to the $-\hat{x}$ axis. The horizontally ($\hat{x}$) and the vertically ($\hat{y}$) polarized components, which can be measured using a simple polarizer front of the detector, can be obtained by using the expressions

$$\begin{aligned} \cos\theta_z &= \sin\theta\cos\phi \\ \cos\theta_x &= \sin\theta\sin\phi \\ \cos\theta_y &= \cos\theta. \end{aligned} \tag{23}$$

In real measurements the coordinate system defined by $\hat{x}_1\hat{y}_1\hat{z}_1$ is more suitable, see Figure 8. The transformations in this case are $\hat{x}_1 = \hat{x}\sin\Psi$, $\hat{y}_1 = \hat{y}$ and $\hat{z}_1 = \hat{z}\cos\Psi$.

The total radiation fluence in the ultrarelativistic limit ($\theta_x, \theta_y, \gamma^{-1} \ll 1$) becomes a simple equation [40]

$$\frac{\mathrm{d}W}{\mathrm{d}\Omega \mathrm{d}\omega} = \frac{q^2}{4\pi^3\varepsilon_0 c}\frac{\theta_x^2+\theta_y^2}{(\gamma^{-2}+\theta_x^2+\theta_y^2)^2}\frac{1}{(1-\theta_y\cot\Psi)^2}, \tag{24}$$

which is almost the same as the earlier obtained fluence except the extra asymmetric term. In our experiment and in many experimental setups, the incident angle is set to the convenient $\Psi = 45°$. The transition radiation distribution in this case is shown on Figure 9.

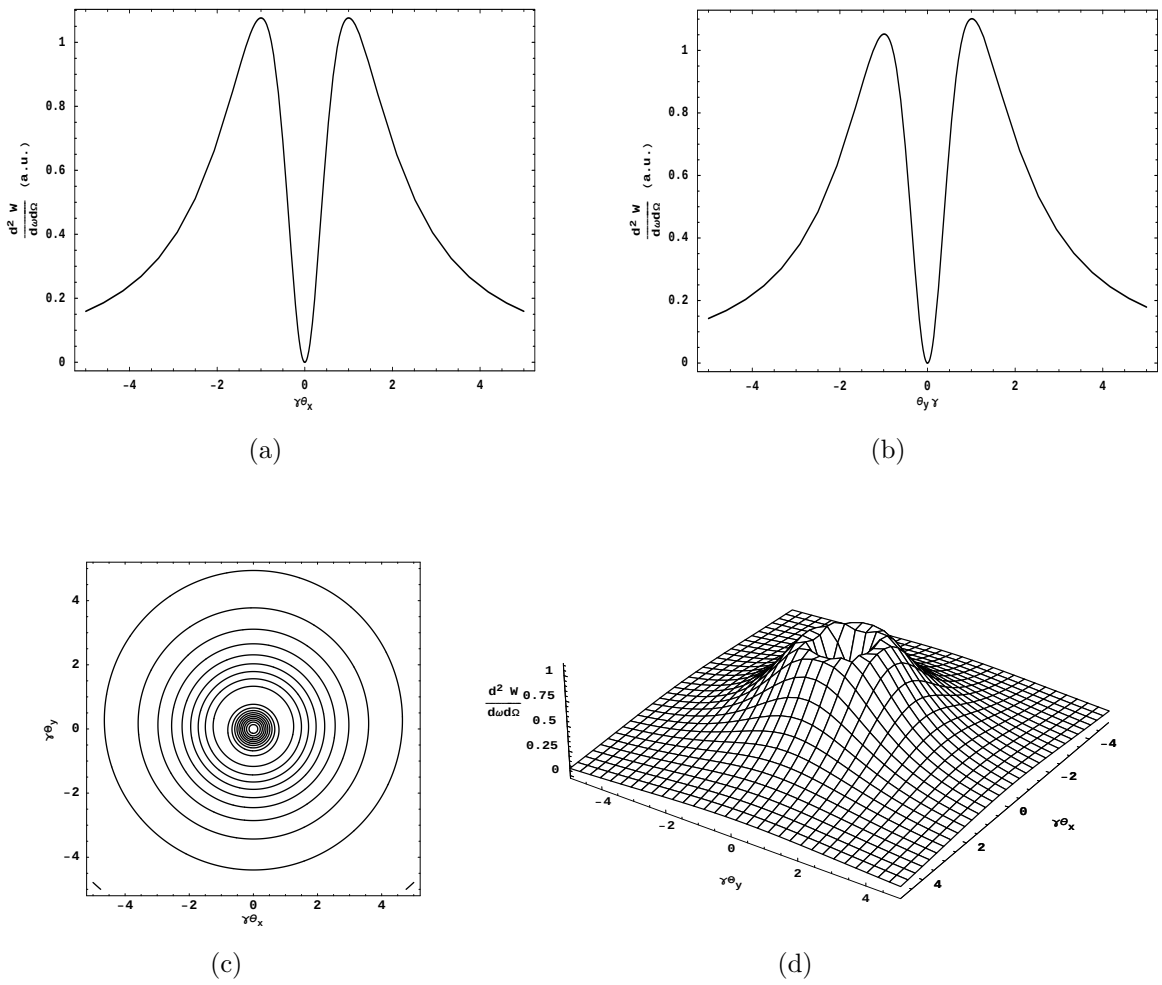

Figure 9: Transition radiation angular distribution at $\Psi = 45°$-incidence. The pictures on the top show the horizontal (a) and the vertical (b) components of the TR angular distribution. The (c) and (d) pictures show the total radiation angular distribution. Note the asymmetry on the vertical component (b).

2.1.3 Far-field vs. near field approximation

In the previous section we used the so called far-field or wave-zone approximation, meaning the radiation source is considered as a single point one. To archive this approximation the observation distance, L, must be much larger than the formation

length, where L_f is

$$L_f = \frac{\lambda}{\pi} \frac{1}{\gamma^{-2} + \theta_x^2 + \theta_y^2}. \tag{25}$$

This requirement, in some cases, gives very large observation length, for instance if the beam energy 300 GeV and the observed wavelength is 500nm, the target-to-detector distance should be around 18000m! If this approximation can not be met, we must use the so-called near-field or (pre-wave) condition [43]. In such a case, the angular distribution of the radiation changes the most as it can be seen in Figure 11. The Figure 11 also shows the dependence of the maximum position [44] in the near-field approximation.

The (11) equation in the case of forward radiation has another meaning, called coherent length, that is the particle produces another photon at the distance comparable or less than coherent length from the radiation source, those two will interfere. At longer distances than L_f the field of the charged particle and the photon's field are completely separated, the interference is not possible. In case of backward radiation the coherent length is one wavelength, the field separation is instantaneous.

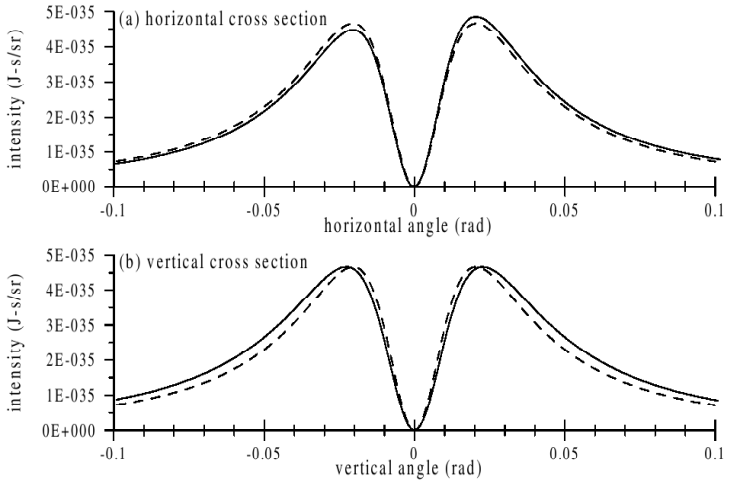

Figure 10: Transition radiation angular distribution emitted by a 25 MeV electron for the case of normal (dashed-line) and $\Psi = 45°$-incidence (solid-line) [41].

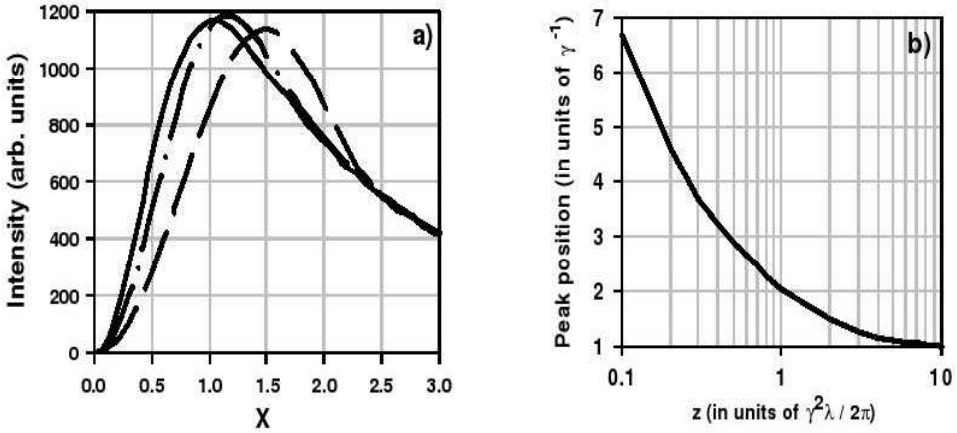

Figure 11: a) Transition radiation angular distribution in the pre-wave zone calculated for different distances from target: $z = 10\gamma^2\frac{\lambda}{2\pi}$-solid line, $z = 4\gamma^2\frac{\lambda}{2\pi}$ -dash-doted line, $z = 2\gamma^2\frac{\lambda}{2\pi}$ -dashed line. b) dependence of the maximum position as a function of the distance from the target [42].

2.2 Diffraction radiation

If we make a hole on a TR radiator to let the electron to go through freely, we still get some radiation in the backward and the forward direction. The fields of the moving charge still interact with the radiator screen. The obtained radiation, however, has different properties than the TR and it is called diffraction radiation (DR). To summarize the above, DR is generated when a charged particle passes through an aperture (slit or hole in a conductor or a dielectric material) or near at a distance a[1], with the condition

$$a \leq \frac{\lambda\gamma}{2\pi}, \tag{26}$$

where λ is the observed wavelength [40]. As the relativistic charged particle passes a metallic structure it will radiate along the particle trajectory (forward diffraction radiation, FDR) and along the spectacular reflection (backward diffraction radiation, BDR). The TR and DR have a common root since both are generated by dynamical polarization of the medium due the electromagnetic field of the charged particle.

The condition (26) can be explained by method of the virtual quanta and by the so-called spot-size of the radiation. In the Weizsaker-Williams approximation the Fourier components of the fields (13) at distance of a from the particle trajectory and the spectral fluence can be written as

$$\tilde{E}_{\perp}(\mathbf{k},\omega) \propto \left(\frac{\omega a}{\gamma c}\right) K_1\left(\frac{\omega a}{\gamma c}\right) \tag{27}$$

[1]In some literature the $a = \gamma\lambda/2\pi$ is called the radiation impact parameter.

and

$$\frac{\mathrm{d}W_{\perp}}{\mathrm{d}\Omega \mathrm{d}\omega} \propto \left(\frac{\omega a}{\gamma c}\right)^2 K_1^2\left(\frac{\omega a}{\gamma c}\right), \tag{28}$$

where K_1 is the modified Bessel function.

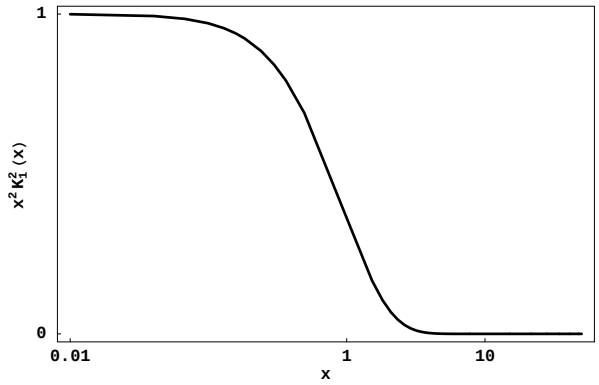

Figure 12: Properties of the modified Bessel function.

Considering the behavior of the $x^2K_1^2(x)$ function, see Figure 12, the intensity of the spectral fluence will drop rapidly around $x = O(1)$ or

$$\frac{\omega a}{\gamma c} = \frac{2\pi a}{\gamma \lambda} = O(1) \text{ or } a = \frac{\gamma \lambda}{2\pi}. \tag{29}$$

In (29) the a symbol is commonly called spot size, since the high proportion of the radiation is created in this range. From the definition of the spot size, which has wavelength dependence, the (26) condition can be interpreted immediately: The spot size must be larger than the aperture to obtain diffraction radiation.

2.2.1 Theory of diffraction radiation

The mathematical derivation of diffraction radiation properties has been extensively studied [45, 46, 37]. These calculations for different environmental conditions are usually rather complex. In the recent years, due to the increased interest in this area, new and simpler methods have been developed [17, 16]. These methods utilize the method of virtual quanta, the Huygens-Fresnel diffraction approach and the Babinet's principle. In this section we will show the method developed by Fiorito and Rule [17] to obtain backward radiation from any arbitrary shaped target.

Let consider a thin reflecting metal infinite plane S_∞. The well known and earlier described TR is created if a charge crosses this surface. If we separate an area out of this screen, S_1 and we call the rest of the area as S_2, the TR field from the infinite conducting screen can be calculated by a Huygens-Fresnel integral over the area $S_\infty = S_1 + S_2$. The TR field in this case can be expressed as $\mathbf{E}_\infty = \mathbf{E}_1 + \mathbf{E}_2$, where $\mathbf{E}_1$ and $\mathbf{E}_2$ are the fields obtained from the Huygens-Fresnel integral over the areas S_1 and S_2, respectively. If the area S_1 is removed from the screen, then the field $\mathbf{E}_2 = \mathbf{E}_\infty - \mathbf{E}_1$ is the desired backward DR radiation due to the Babinet's principle.

As is stated above, by integrating over the target surface, S_2, in the following way the field of the radiation can be calculated

$$E_{x,y}(k_x, k_y) = r_{\parallel,\perp}(\omega, \Psi)\frac{1}{4\pi^2}\int\int E_{ix,iy}(x, y)\,\mathrm{e}^{-i\mathbf{k}\boldsymbol{\rho}}\,\mathrm{d}x\,\mathrm{d}y, \tag{30}$$

where $E_{ix,iy}$ are the components of the field of the incoming charged particle and k_x and k_y are the components of the wave vector $\mathbf{k}$ in the plane normal to the direction $\mathbf{z}$ and the Ψ is target tilt angle shown in Figure 13. The fields E_x and E_y are the $\mathbf{x}$ and

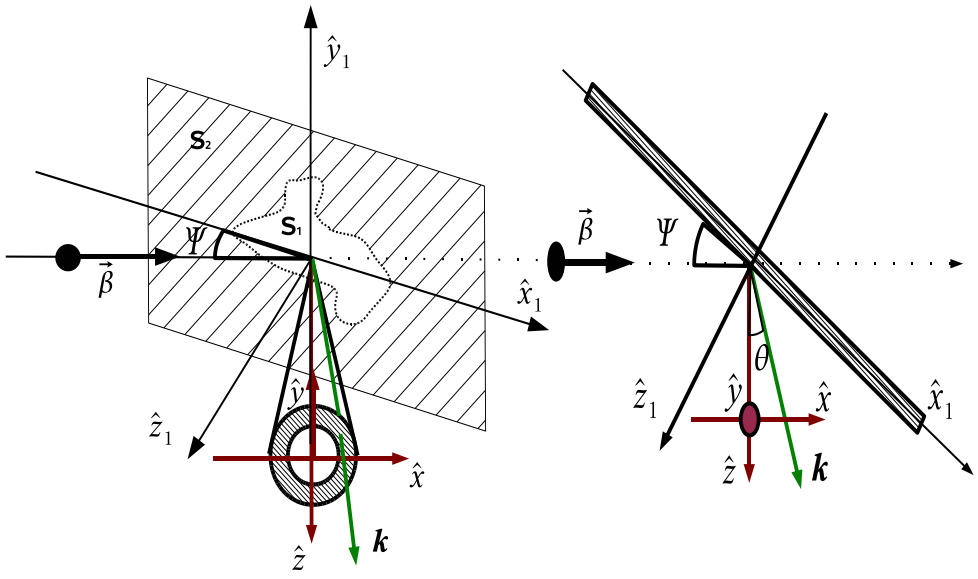

Figure 13: Diffraction radiation from an arbitrary target.

y polarized components of the backward radiation with the correspondent Fresnel reflection coefficients $r_{\parallel}$ and $r_{\perp}$, respectively. The phase term in (30), which is a function of $\boldsymbol{\rho}(x', y')$, a vector lying in the plane of the screen, can be related to the coordinates (x, y) by the transformations $x = x' \sin\Psi$, $y = y'$, and the differential elements of area $\mathrm{d}x\mathrm{d}y$=$\mathrm{d}x'\mathrm{d}y' \sin\Psi$.

In order to evaluate the (30) integral we should express the incoming fields $\mathbf{E}_{x,y}$ by its Fourier transform so that

$$E_{x,y}(k_x, k_y) = \frac{ie}{(2\pi)^2\varepsilon_0}\frac{r_{\parallel,\perp}}{4\pi^2}\int\int \frac{k'_{x,y}}{(k'^2_x + k'^2_y + \bar{\alpha}^2)}\,\mathrm{e}^{-i(\mathbf{k}'-\mathbf{k})\boldsymbol{\rho}}\,\mathrm{d}x\,\mathrm{d}y\,\mathrm{d}k'_x\,\mathrm{d}k'_y, \qquad (31)$$

where $\bar{\alpha} \equiv 2\pi/(\beta\gamma\lambda)$, and the phase term is

$$(\mathbf{k}' - \mathbf{k})\boldsymbol{\rho} = (k'_x - \bar{k}_x)x' \sin\Psi + (k'_y - k_y)y' \qquad (32)$$

where

$$\bar{k_x} \equiv k_x + \left(k_z - \frac{\boldsymbol{k'v}}{v} \right) \cot\Psi. \tag{33}$$

In ultrarelativistic limit the following relations for the wave vector components can be used

$$k_x = k \sin\theta_x \cos\theta_y \approx k\theta_x \qquad k_y = k \cos\theta_x \sin\theta_y \approx k\theta_y$$

$$k_z = k \cos\theta_x \cos\theta_y \approx k, \tag{34}$$

where $\theta_{x,y,z}$ are the projected angles of the vector $\mathbf{k}$ into the (x,z), (y,z) and (x,y) planes, respectively. For $\Psi = 45^\circ$ the (33) term becomes $\bar{k_x} \approx k(\theta_x - \gamma^{-2}/2) \approx k\theta_x$ in the above limit. Therefore, in general, the radiation pattern is shifted by an angle of $\gamma^{-2}/2 \ll 1$.

The mathematical solution of the (31) integral can be obtained only numerically in most of the cases, however for some simple geometry the analytical solution can be retrieved as well. For instance, by integrating (31) over x and y from $-\infty$ to ∞ we obtain two delta functions and finally after the remaining integration the result is nothing else, than the well known transition radiation fields from infinite boundary

$$E^{TR}_{x,y} = \frac{ie}{4\pi^2\varepsilon_0} \frac{r_{\parallel,\perp}}{k} \frac{\theta_{x,y}}{\theta_x^2 + \theta_y^2 + \gamma^{-2}}. \tag{35}$$

Since the radiation fluence can be calculated from the fields using the expression

$$\frac{\mathrm{d}^2 W}{\mathrm{d}\omega\, \mathrm{d}\Omega} = 4\pi\varepsilon_0 k^2 \left(|E_x|^2 + |E_y|^2 \right), \tag{36}$$

one can see that the obtained solution is coincides with the (10) equation for ideally reflecting target, $r_{\parallel,\perp} = 1$.

2.2.2 Diffraction radiation from a half plane

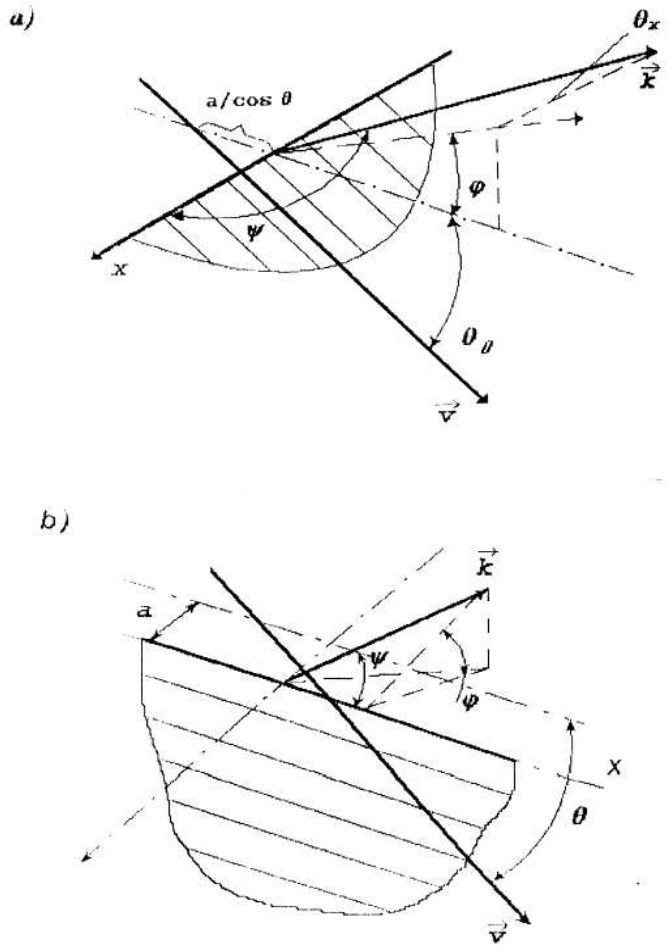

Figure 14: Diffraction radiation from a semi-infinite target ; (a) projection of electron momentum onto the target plane is perpendicular to the edge; (b) projection is parallel to the edge. In ultrarelativistic approximation the spectral angular distribution for both geometries coincide [40].

An exact solution of DR intensity was calculated by A. Kazantsev and G. Surdotovich in 1963 in case of infinitely thin and ideally flat semi plane and perfect conductor target [46]. Their obtained result for DR spectral fluence using far-field

approximation is rather complex

$$\frac{\mathrm{d}W}{\mathrm{d}\Omega\mathrm{d}\omega} = \frac{q^2}{2\pi^3\varepsilon_0 c}\frac{\mathrm{e}^{-\frac{4\pi a}{\lambda\gamma\beta}\sqrt{1+\beta^2\gamma^2\cos^2\psi}}}{\sin\psi}\frac{1}{\gamma^{-2}+\beta^2\cos^2\psi}$$
$$\times\left\{\cos^2\frac{\theta}{2}\cos^2\psi\,(1-\beta\sin\psi\cos\theta_0)+(\gamma^{-2}+\beta^2\cos^2\psi)\sin^2\frac{\theta}{2}(1+\beta\psi\cos\theta_0)\right\} \quad (37)$$
$$\times\left[\left(\sin\psi\cos\theta-\frac{cos\theta_0}{\beta}\right)^2+\frac{(\gamma^{-2}+\beta^2\cos^2\psi)\sin^2\theta_0}{\beta^2}\right]^{-1},$$

where ψ and ϕ are the azimuthal and polar outgoing angles with respect to the target plane and θ_0 is the target tilt angle respect to the particle trajectory. The angular fluence reaches its maximum value at $\cos\psi = 0$ and $\cos\phi = \frac{\cos\theta_0}{\beta}$, which is becomes $\psi = \pi/2$ and $\phi = \pm\theta_0$ in the ultrarelativistic approximation. The first condition determines the radiation plane and the second shows two DR rays. The first radiation cone is along the direction of the incoming charge (θ_0) and the second correspond to the mirror reflection from the target screen ($-\theta_0$).

To transform the (37) equation the commonly used "mirror reflection observation geometry (θ_x, θ_y)" used earlier in the TR calculations we should use the transformations below (See Figure 14)

$$\psi = \frac{\pi}{2} - \theta_x \text{ and } \theta = \theta_y + \theta_0 \quad (38)$$

In the ultrarelativistic limit ($\theta_x, \theta_y \approx \gamma^{-1} \ll 1$) the (37) equation becomes very simple [40]

$$\frac{\mathrm{d}W}{\mathrm{d}\Omega\mathrm{d}\omega} = \frac{q^2}{4\pi^3\varepsilon_0 c}\exp\left(-\frac{\omega}{\omega_c}\sqrt{1+\gamma^2\theta_x^2}\right)\frac{\gamma^{-2}+2\theta_x^2}{(\gamma^{-2}+\theta_x^2)(\gamma^{-2}+\theta_x^2+\theta_y^2)}, \quad (39)$$

where $\omega_c = \gamma/2a$ is the characteristic energy ($\hbar = c = m = 1$), which is a different form of the (26) condition.

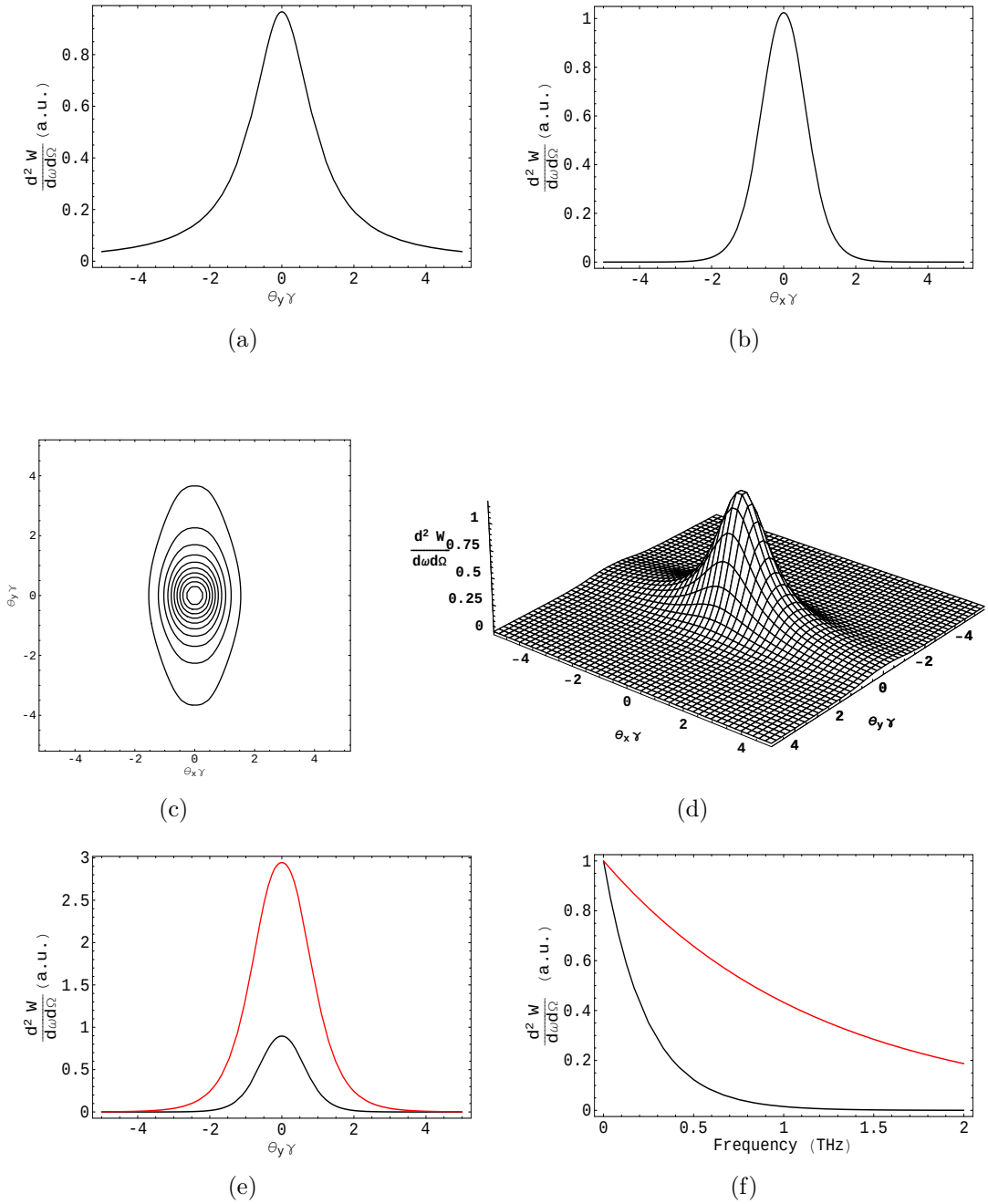

Figure 15: Diffraction Radiation from a half plane target. The angular distribution is shown on Fig. (a)-vertical;(b)-horizontal, and the total radiation angular distribution on (c) and (d) at 1THz observation wavelength. The frequency dependence of the angular distribution radiation is shown on Fig. (e) where red-$f = 0.5$THz, black-$f = 1$THz. Fig (f) shows how the total radiation fluence vs. frequency is depend on the radiator - electron trajectory distance, the black line represents $h = 5mm$, and the red $h = 1mm$

As you can see from Figure 15 the angular distribution of DR from semi plane has only one maximum at $\theta_x = \theta_y = 0$. The one of the most important difference compared to TR, the DR angular distribution is depend on the observed radiation frequency and on the distance between the target and the charge trajectory, which will play very important role in the bunch length measurements.

The half plane set up is very common to avoid co planarity problems which usually effect the slit configurations. For measurements of beam properties the slit configuration is more sensitive as we will see it in the following sections.

2.2.3 Diffraction radiation from a slit

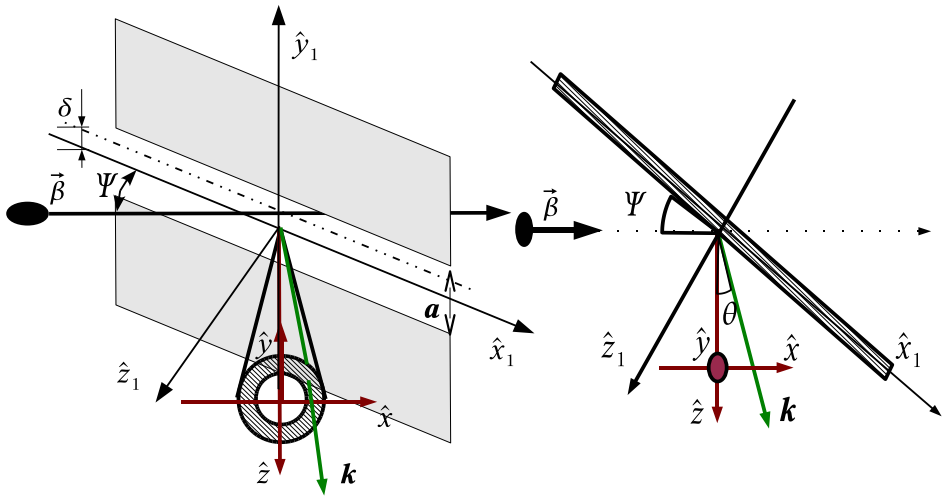

Figure 16: Diffraction radiation from a slit target in parallel orientation of the slit with respect to the plane of incidence

The solution of DR from a charged particle as it crosses a slit made from two semi-planes has been published in 1972 by Ter-Mikaelian using the rather difficult Weiner-Hopf method [37]. However in a recently published paper, Fiorito and Rule introduced a simpler method to calculate DR from arbitrary shape target as we described earlier. They also provided a solution in case of the slit target using the (30) equation. In our experimental setup the electron is passing a slit with parallel orientation respect to the plane of incidence as shown in Figure 16.

In order to evaluate the (30) integral in case of the slit target, we are using its Fourier version (31) integrating first over x, ranges from $-\infty$ to ∞, which yields to $2\pi\delta(k'_x - \bar{k}'_x)$. After the second integration over y, since the y' variable ranges from

$-\infty$ to a_1 and from a_2 to ∞, and using $\bar{k}'_x \approx k_x$ in case of $\Psi = 45^\circ$ we obtain

$$E_x(k_x, k_y) = \frac{ie}{4\pi^2\varepsilon_0} r_\parallel \left(\frac{1}{2\pi}[I_1 + I_2] + \frac{k_x}{(k_x^2 + k_y^2 + \bar{\alpha}^2)}, \right) \tag{40}$$

where

$$I_1 = (-i) \int_{-\infty}^{\infty} \mathrm{d}k'_y \frac{k_x}{(k_x^2 + k_y^2 + \bar{\alpha}^2)(k'_y - k_y)} \, \mathrm{e}^{-i(k'_y - k_y)a_1} \tag{41}$$

and

$$I_1 = (+i) \int_{-\infty}^{\infty} \mathrm{d}k'_y \frac{k_x}{(k_x^2 + k_y^2 + \bar{\alpha}^2)(k'_y - k_y)} \, \mathrm{e}^{-i(k'_y - k_y)a_2} \tag{42}$$

The I_1 and I_2 integrals can be solved using the Cauchy integral formula with poles at $k'_y = \pm i\sqrt{k_x^2 + \bar{\alpha}^2}$ and at $k'_y = k_y$. The result is

$$I_1 = \pi \left[\frac{k_x}{f(f - ik_y)} \, \mathrm{e}^{-a_1(f - ik_y)} - \frac{k_x}{(k_x^2 + k_y^2 + \bar{\alpha}^2)(k'_y - k_y)} \right] \tag{43}$$

and

$$I_2 = \pi \left[\frac{k_x}{f(f + ik_y)} \, \mathrm{e}^{-a_2(f + ik_y)} - \frac{k_x}{(k_x^2 + k_y^2 + \bar{\alpha}^2)(k'_y - k_y)} \right] \tag{44}$$

where $f^2 \equiv k_x^2 + \bar{\alpha}^2$. Substituting these expressions for I_1 and I_2 into (40) we obtain the x component of the DR fields, E_x. The other polarization component, E_y can be obtained in a similar manner. So the final results are

$$E_x(k_x, k_y) = \frac{ie}{4\pi^2\varepsilon_0} r_\parallel(\omega, \Psi) \frac{\bar{k}_x}{f} \left[\frac{1}{f - ik_y} \, \mathrm{e}^{-a_1(f - ik_y)} + \frac{1}{f + ik_y} \, \mathrm{e}^{-a_2(f + ik_y)} \right] \tag{45}$$

and

$$E_y(k_x, k_y) = \frac{e}{4\pi^2\varepsilon_0} r_\perp(\omega, \Psi) \left[\frac{1}{f - ik_y} \, \mathrm{e}^{-a_1(f - ik_y)} - \frac{1}{f + ik_y} \, \mathrm{e}^{-a_2(f + ik_y)} \right] . \tag{46}$$

One can see that in the limit of $a_{1,2} \to 0$ these give the same result as the earlier obtained solution for TR field (35).

The horizontally polarized DR intensity (i.e., parallel to the slit edge) is defined in terms of the x component of the fields, so using the results above and substitute $a_{1,2} = a/2 \pm \delta$ it becomes

$$\begin{aligned}\frac{\mathrm{d}^2 N_{horiz.}}{\mathrm{d}\Omega \mathrm{d}\omega} &= \frac{4\pi k^2 c\varepsilon_0}{\hbar\omega}) \left|E_x\right|^2 \\ &= \left|r_{\parallel}\right|^2 \frac{\alpha k^2 \bar{k}_x^2 \, \mathrm{e}^{-af}}{2\pi\omega f^2 (f^2 + k_y^2)} \left[\cosh(2f\delta) + \sin(ak_y + \Phi(k_x, k_y))\right],\end{aligned} \tag{47}$$

where

$$\Phi(k_x, k_y) = sin^{-1}[(f^2 - k_y^2)/(f^2 + k_y^2)] = cos^{-1}[-2fk_y/(f^2 + k_y^2)] \tag{48}$$

and $\alpha \equiv \frac{e^2}{4\pi\varepsilon_0 c\hbar} \simeq \frac{1}{137}$ is the fine structure constant.

Correspondingly the vertically polarized intensity (i.e., perpendicular to the slit edge) which is related to E_y becomes

$$\begin{aligned}\frac{\mathrm{d}^2 N_{vert.}}{\mathrm{d}\Omega \mathrm{d}\omega} &= \frac{4\pi\varepsilon_0 k^2 c}{\hbar\omega} \left|E_y\right|^2 \\ &= \left|r_{\perp}\right|^2 \frac{\alpha k^2 \, \mathrm{e}^{-af}}{2\pi\omega (f^2 + k_y^2)} \left[\cosh(2f\delta) - \sin(ak_y + \Phi(k_x, k_y))\right].\end{aligned} \tag{49}$$

These results are in perfect correlations with earlier obtained solutions like the semi-plane radiation or the transition radiation. One can see that if either a_1 or a_2 is set to infinity the above expression becomes the horizontal and the vertical polarized intensities of DR from semi-plane. Likewise the expression of transition radiation is obtained if $a \to 0$.

If δ, the displacement from the center of the slit, is small the two equations, (47) and (49), can be rewritten in the following forms using the first two Taylor-series of

the hyperbolic cosine function

$$\frac{\mathrm{d}^2 N_{horiz.}}{\mathrm{d}\Omega \mathrm{d}\omega} = \left|r_{\parallel}\right|^2 \frac{\alpha}{2\pi\omega}\gamma^2 \frac{X^2}{1+X^2}\frac{\mathrm{e}^{-R(1+X^2)^{1/2}}}{1+X^2+Y^2} \times \left[1+2\left(\frac{\delta}{\gamma\bar{\lambda}}\right)^2(1+X^2)+\sin(RY+\Psi(X,Y))\right] \tag{50}$$

and

$$\frac{\mathrm{d}^2 N_{vert.}}{\mathrm{d}\Omega \mathrm{d}\omega} = \left|r_{\perp}\right|^2 \frac{\alpha}{2\pi\omega}\gamma^2 \frac{\mathrm{e}^{-R(1+X^2)^{1/2}}}{1+X^2+Y^2} \times \left[1+2\left(\frac{\delta}{\gamma\bar{\lambda}}\right)^2(1+X^2)-\sin(RY+\Psi(X,Y))\right], \tag{51}$$

where $X = \gamma\theta_x$ and $Y = \gamma\theta_y$ are the x and y projected angles in units of γ^{-1}, $R \equiv a/\gamma\bar{\lambda}$ and the phase term is

$$\begin{aligned}\Psi(X,Y) &= \sin^{-1}[(1+X^2-Y^2)/(1+X^2+Y^2)] \\ &= \cos^{-1}[-2(1+X^2)^{1/2}Y/(1+X^2+Y^2)].\end{aligned} \tag{52}$$

The R value in the above equations is related to the spot size introduced in the beginning of this section. The R corresponds to the x value in Figure 12. Note that the (50) and (51) equations are valid also in the case of perpendicular orientation of the slit respect to the plane of incidence, but with the coefficients $\left|r_{\perp}\right|^2$ and $\left|r_{\parallel}\right|^2$ interchanged. As it can be seen from the above equations, the total intensity has a minimum when $\delta = 0$. So it is possible to center the beam on the slit by minimizing the measured intensity. This fact will be very useful in the later when we investigate the effect of the transversal beam sizes.

In general, the sum of the horizontal and vertical polarization component will be observed, however it is possible to measure separately both, simply by using a rotatable polarizer in front of the detector. In the next section we will show that each

of these polarization components carrying information about the beam properties, like beam divergence, transversal beam size and energy. The energy dependence is can be seen immediately due to the fact that it is proportional to γ^2.

The properties of the spectral-angular fluence of DR from a slit target can be seen on Figure 17. As you can see from the angular distribution it has two maximums at angle of $1/\gamma$. The vertically polarized part of the radiation is carrying higher intensity than the horizontally polarized radiation. The radiation has a well defined minimum at the center point which can be understand by the fact that the two slit radiation is the interference of the radiation produced by two semi-infinite plane target.

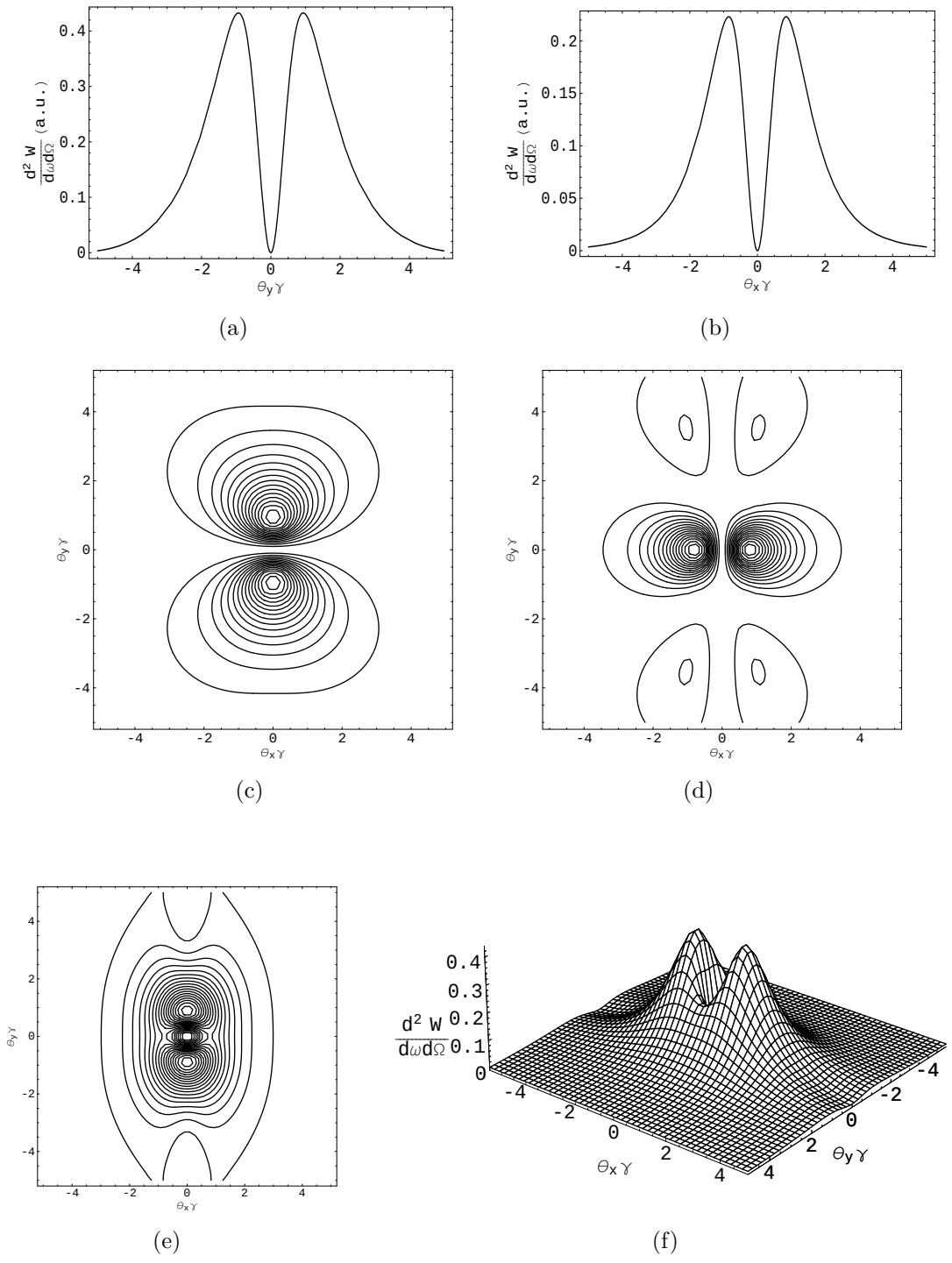

Figure 17: Diffraction Radiation from a $5mm$ wide slit. The angular distribution is shown - (a) - vertically polarized at $\theta_x\gamma = 0$; (b) - horizontally polarized at $\theta_y\gamma = 0$; (c) and (d) - the contour of vertically and horizontally polarized radiation respectively and the total radiation angular distribution on (e) and (f), at $600\mu m$ observation wavelength.

2.3 Effects of beam parameters on DR from a slit

The angular distributions of the diffraction radiation created by a single charge have been discussed in the previous sections. In general, however, the radiation is produced by a number of electrons formed by the charge generation and acceleration processes (e.g. electron gun, alpha magnet etc). These electrons are usually distributed in separated bunches, with some spatial distribution. The radiation created by these bunches is what we measure. Most of the radiation properties are affected by the bunch distributions. In the following sections we will investigate the effects of the bunch size (transverse and longitudinal) and the beam divergence on the production of diffraction radiation from a slit. Our goal is, actually the reverse process, that is to obtain beam size and beam divergence from the measured radiation.

2.3.1 Effect of transverse beam size

To investigate the effect of the transverse beam size on the DR angular distribution we will use Gaussian assumption for the beam charge distribution in the plane normal to the slit, that is

$$G(y,\sigma_y) = \frac{1}{\sqrt{2\pi}\sigma_y}\,\mathrm{e}^{-(y-\delta)^2/2\sigma_y^2}, \tag{53}$$

where δ is the slit center displacement (See Figure 16.). The effect of such a beam on the DR angular fluence can be obtained by the convolution of the two distributions. For example the vertical distribution becomes [16]

$$\begin{aligned}\frac{\mathrm{d}^2N_{vert.}}{\mathrm{d}\Omega\mathrm{d}\omega} &= |r_\perp|^2\,\frac{\alpha k^2\,\mathrm{e}^{-af}}{2\pi\omega(f^2+k_y^2)} \\ &\times\,[\,\mathrm{e}^{2f^2\sigma_y^2}\cosh(2f\delta) - \sin(ak_y+\Phi(k_x,k_y))].\end{aligned} \tag{54}$$

If $2f^2\delta^2 \ll 1$ the hyperbolic cosine can be written as

$$\cosh(2f\delta) \equiv \frac{1}{2}(e^{2f\delta} + e^{-2f\delta}) \simeq \mathrm{e}^{2f^2\delta^2} \tag{55}$$

and (54) becomes

$$\begin{aligned} \frac{\mathrm{d}^2 N_{vert.}}{\mathrm{d}\Omega \mathrm{d}\omega} &= |r_\perp|^2 \frac{\alpha k^2 \, \mathrm{e}^{-af}}{2\pi\omega(f^2 + k_y^2)} \\ &\times [\, \mathrm{e}^{2f^2(\sigma_y^2+\delta^2)} - \sin(ak_y + \Phi(k_x, k_y))]. \end{aligned} \tag{56}$$

The result is somehow surprising, the standard deviation of the Gaussian beam, σ_y and the displacement, δ have the same effect on the DR angular distributions from a slit.

Let assume that the beam has a separable spatial distribution, $S = S_1(\delta)S_2(\varepsilon)$, where δ and ε in the direction of y', x' (See Figure 16.) and the average beam sizes are $\langle\delta\rangle$ and $\langle\varepsilon\rangle$. Also assume that the beam has been centered on the slit by minimizing the observed intensity due to the effect of the displacement δ on (50) and (51), as we noted earlier. The angular distribution in this case will have the same form as (51) and (51) by only change the meaning of the δ variable to the rms vertical beam size. From now on the variables δ and ε will refer to the orthogonal rms beam size components, perpendicular and parallel respectively, to the plane of incidence. The parallel component, ε, however, can be measured only in perpendicular orientation of the slit with respect to the plane of incidence. In practice this means either rotating the slit or insert another one on the beam line, Figure 18.

The dependence of the angular distribution (AD) on the beam size, δ is shown on Figure 19. These results were obtained by using (50) and (51) equations with

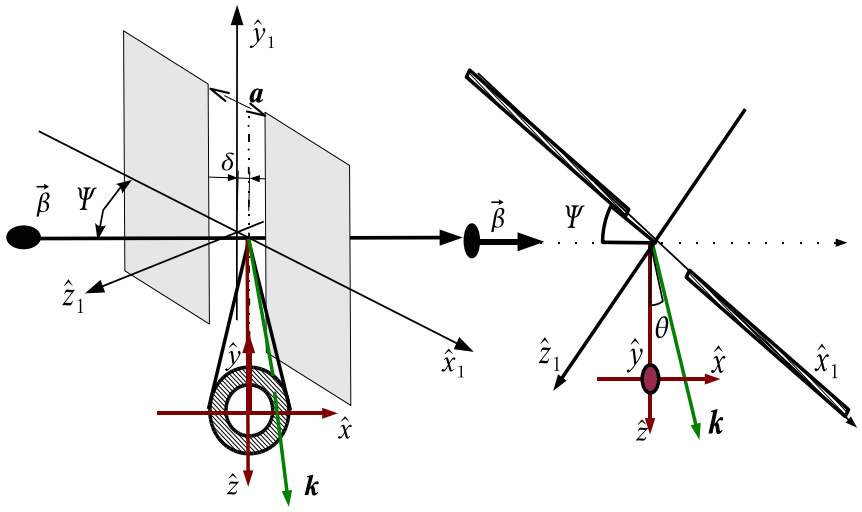

Figure 18: Diffraction radiation from a slit in perpendicular orientation of the slit with respect to the plane of incidence.

the following parameters; $\gamma = 45$, slit opening $a = 1\,mm$ and since the AD of the diffraction radiation is depend on the wavelength, in the calculations we used $\lambda = 500\,\mu m$ as observation wavelength.

To obtain the beam size from measured data is possible using the vertical component only. The horizontal polarized component of AD, as it can be seen on Figure 19a., has only small effect on the beam size, and in practice it is impossible to obtain bunch sizes from it, due to the lack of absolute calibration.

The vertical component of AD is deformed due to the variation of beam size as it can be seen on Figure 19b. To obtain the vertical beam size of the electron bunch from the measured data one can use a fit to (51), where δ is the only one free parameter not considering the normalization constant[2].

However the vertical component of AD has two clean maximums and between

[2]In general the normalization constant is also contains the overall detection efficiency.

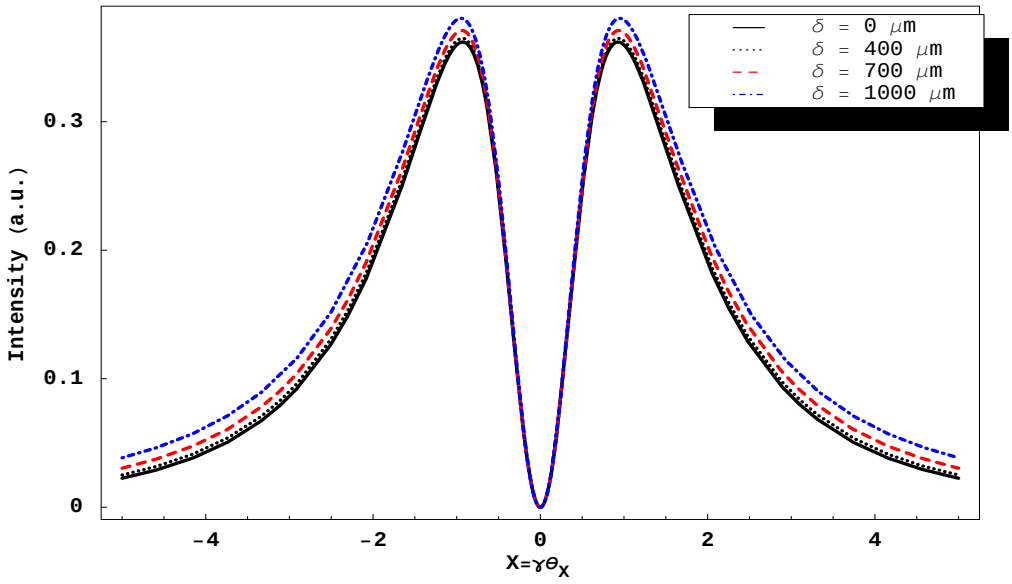

(a) The horizontal component of DR at $Y = \gamma\theta_y = 0$.

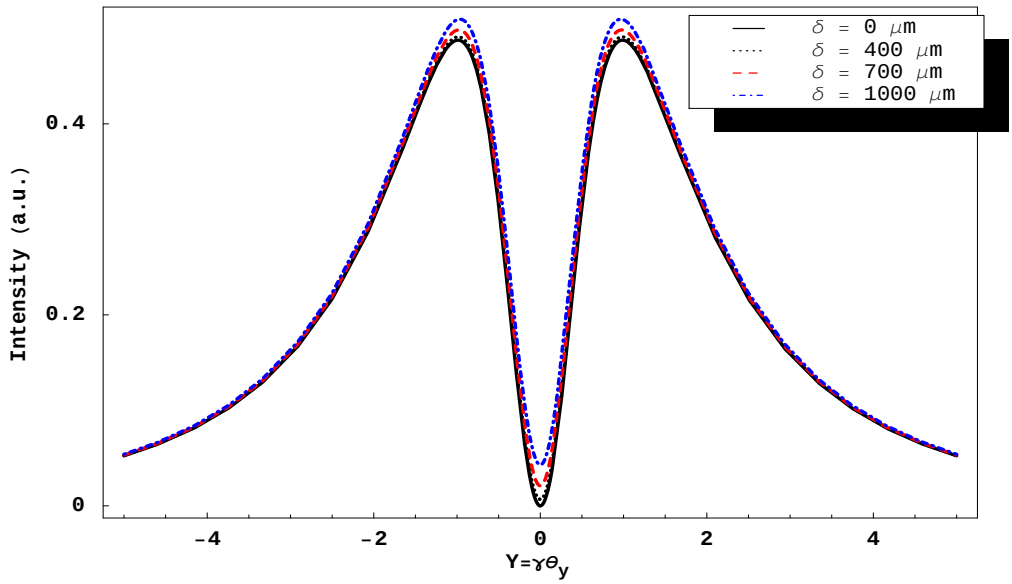

(b) The vertical component of DR at $X = \gamma\theta_x = 0$.

Figure 19: Effect of the beam size, δ, on the angular distribution of the diffraction radiation from a slit. The parameters used for the calculations: $\gamma = 45$, observation wavelengths $\lambda = 600\,\mu m$, slit opening $a = 1\,mm$.

them a clear minimum at $\theta_y = 0$ and their ratio is a function of the beam size [16], which gives another possibility to obtain the vertical beam size. In [16] the author defined a function as

$$F(Y) \equiv (1+Y^2)\frac{\mathrm{d}^2 N_{vert.}}{\mathrm{d}\Omega \mathrm{d}\omega} \sim A\left\{1 + 2\left(\frac{\delta}{\gamma\bar{\lambda}}\right)^2 - \sin(RY + \Psi(0,Y))\right\}, \tag{57}$$

where A contains all the constant factors. As it can be seen the above definition, $F(X)$ is a periodical function with minimum value of

$$F(Y)_{min} = 2A\left(\frac{\delta}{\gamma\bar{\lambda}}\right)^2, \tag{58}$$

while the maximum value is

$$F(Y)_{max} = 2A\left[1 + \left(\frac{\delta}{\gamma\bar{\lambda}}\right)^2\right]. \tag{59}$$

Therefore the minimum to maximum ratio of the $F(Y)$ function can be written as

$$R = \frac{F(Y)_{min}}{F(Y)_{max}} = \frac{\left(\frac{\delta}{\gamma\bar{\lambda}}\right)^2}{1 + \left(\frac{\delta}{\gamma\bar{\lambda}}\right)^2}, \tag{60}$$

and after simple transformations, the expression for the vertical beam size becomes

$$\delta = \frac{\gamma\lambda}{2\pi}\sqrt{\frac{R}{1-R}} \approx \frac{\gamma\lambda}{2\pi}\sqrt{R}, \text{ if } R \ll 1. \tag{61}$$

If the beam cannot be centered due to some requirement, instead of the formula above the following equation can be used to obtain the vertical beam size [47]

$$\delta = \frac{\gamma\lambda}{2\pi}\sqrt{\frac{1}{2}\ln\left[\frac{1+R'}{(1-R')\cosh\left(\frac{4\pi\delta_{ctr}}{\gamma\lambda}\right)}\right]}, \tag{62}$$

where δ_{ctr} is the slit center offset and

$$R' = \frac{\exp\left(\frac{8\pi^2\delta^2}{\gamma^2\lambda^2}\right)\cosh\left(\frac{4\pi\delta_{ctr}}{\gamma\lambda}\right) - 1}{\exp\left(\frac{8\pi^2\delta^2}{\gamma^2\lambda^2}\right)\cosh\left(\frac{4\pi\delta_{ctr}}{\gamma\lambda}\right) + 1}. \tag{63}$$

2.3.2 Polarization and transverse beam size

There is one more possibility to measure transverse beam sizes, proposed by Potylistyn, via analysis of the diffraction radiation polarization characteristics [48]. The diffraction radiation created by a single electron, as it passes through the center of the slit, is radially polarized. However, if the offset is not zero, e.g. $\delta_{ctr} \neq 0$, a circular polarization component appears. To obtain the beam size, σ, in this method we have to analyze the third Stroke parameter, ξ_3, of the DR polarization. In case of perpendicular orientation of the slit with respect to the plane of incidence the third Stroke parameter becomes

$$\xi_3 = \frac{\frac{\mathrm{d}^2W_{\parallel}}{\mathrm{d}\Omega\mathrm{d}\omega} - \frac{\mathrm{d}^2W_{\perp}}{\mathrm{d}\Omega\mathrm{d}\omega}}{\frac{\mathrm{d}^2W_{\parallel}}{\mathrm{d}\Omega\mathrm{d}\omega} + \frac{\mathrm{d}^2W_{\perp}}{\mathrm{d}\Omega\mathrm{d}\omega}} \approx \frac{-\left[1 + \frac{2\bar{\sigma}^2R^2(1+X^2)}{a\sin\Psi}\right] + (1+2X^2)[\cos(RY+\chi)]}{\left[1 + \frac{2\bar{\sigma}^2R^2(1+X^2)}{a\sin\Psi}\right](1+2X^2) - \cos(RY+\chi)}, \tag{64}$$

where $\bar{\sigma} = \sigma/a\sin\Psi$, $R = \frac{a\sin\Psi}{\gamma\lambda}$ and

$$\chi = \arccos\left[\frac{1+X^2-Y^2}{1+X^2+Y^2}\right]. \tag{65}$$

The requirement for this method is to detect the DR yield in the angular pattern minimum for two polarization positions. So there is no need a detailed angular distribution to obtain

In the previous we assumed that the divergence of the beam is zero, however in practice this is not true and it affects both the horizontal and vertical polarized angular distributions of DR, as well as the above detailed beam size measurement methods.

2.3.3 Effect of beam divergence

The beam divergence for any realistic beam is not negligible and affects both the horizontal and vertical intensities of DR. The effect of divergence can be calculated by a two dimensional convolution of a distribution of particle trajectory angles projected in the X,Z and Y,Z planes. In these calculations we used separable Gaussian distributions on θ_x with ε' rms divergence and on θ_y with δ' rms divergence

$$G(\theta_x, \varepsilon') = \frac{1}{\sqrt{2\pi}\varepsilon'} \exp\left(\frac{-\theta_x^2}{2\varepsilon'^2}\right) \tag{66}$$

and

$$G(\theta_y, \delta') = \frac{1}{\sqrt{2\pi}\delta'} \exp\left(\frac{-\theta_y^2}{2\delta'^2}\right). \tag{67}$$

To simplify our calculations we used one dimension convolution only due to the insignificant effect of ε' on the vertical and δ' on the horizontal components [17]. The calculations were performed numerically assuming a $500\mu m$ vertical beam size, δ, at $\gamma = 45$ with observation wavelength of $\lambda = 600\,\mu m$ and the slit width $a = 1\,mm$ in the case of parallel orientation of the slit with respect to the plane of incidence, Figure 16. The obtained results are shown on Figure 20. In the calculations we used four different divergence sets.

The same strategy that we used for transverse beam size measurements can be used to obtain beam divergence, e.g. the maximum-minimum ratio. However as it can be seen on Figure 20 (a) and (b) in case of increasing divergence the maximums are decreased and the minimums are increased. This is different than the effects of the beam size, see Figure 19.

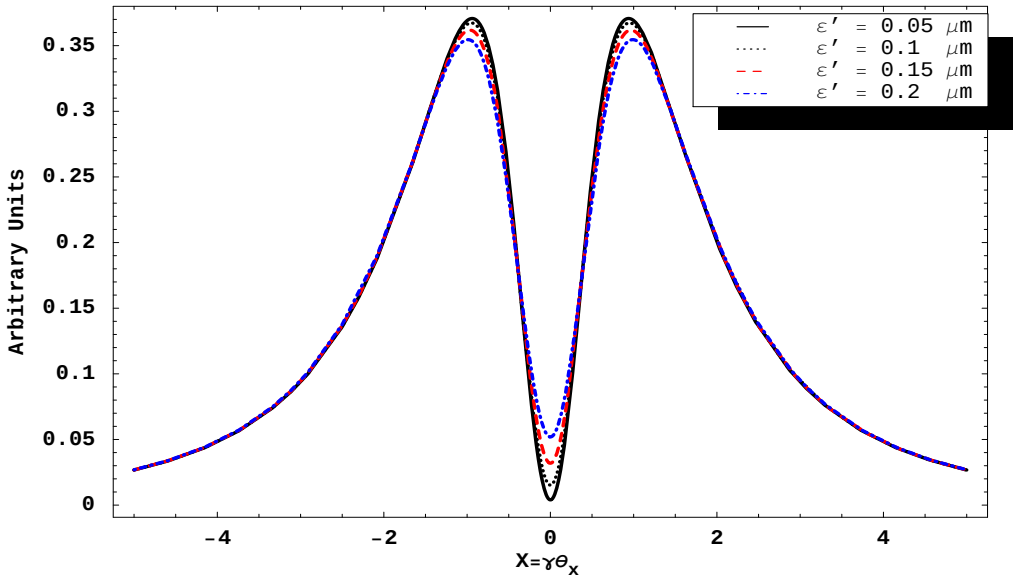

(a) The horizontal component of DR at $Y = \gamma\theta_y = 0$.

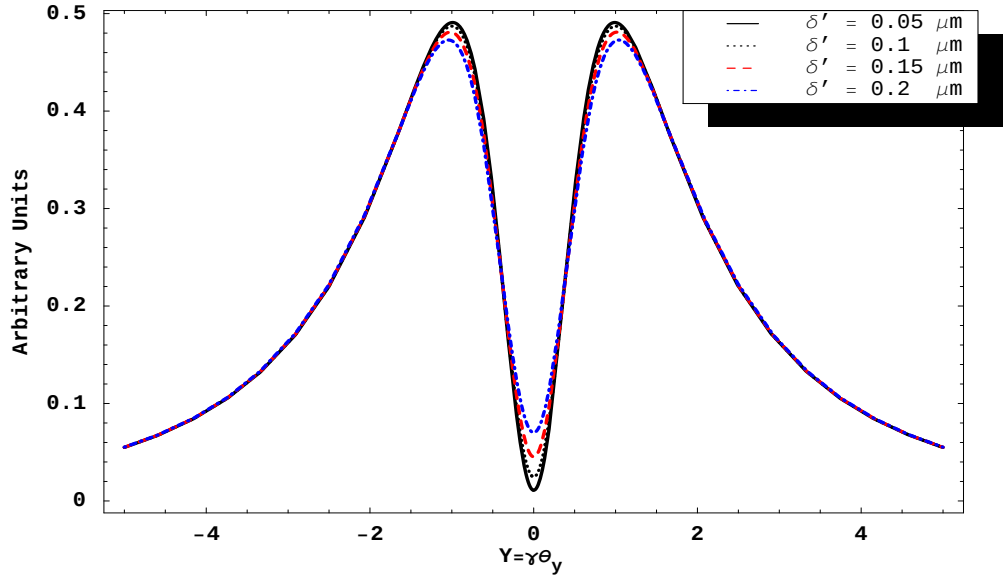

(b) The vertical component of DR at $X = \gamma\theta_x = 0$.

Figure 20: Effect of the beam divergence, ε' and δ', on the angular distribution of the diffraction radiation from a slit. The parameters used for the calculations: $\gamma = 45$, observation wavelengths $\lambda = 600\,\mu m$, slit opening $a = 1\,mm$, vertical beam size $\delta = 500\mu m$.

By comparing the horizontally polarized component of DR on Figure 19a and Figure 20a we can see that the effects of the divergence ε', and the vertical beam size can be separated by analyzing the shape of pattern in vicinity of the origin. The peak value however is not independent from the beam size. Using this method the horizontal divergence, ε' can be measured but the vertical beam size is still unknown due to some problems detailed in the previous section.

The vertically polarized components, which are used to obtain the vertical beam size by the maximum-minimum ratio, is affected by the vertical divergence, δ'. From Figure 19b and Figure 20b it is clearly seen that the effect of divergence, δ', is conflict significantly with the effect of the beam size. The maximum-minimum ratio depends on both and the two effects are not separable for this component.

There are a few solutions to measure divergence without the effect of beam sizes. In the knowledge of the vertical and the horizontal divergence the transverse beam size can be determined. As we noted earlier the horizontal divergence, ε', is measurable in case of parallel orientation of the slit with respect to the plane of incidence, see Figure 16. In the same manner the vertical divergence, δ', can be obtained in perpendicular orientation of the slit with respect to the plane of incidence, see Figure 18.[3] This can be achieved by simply rotate the slit configuration by $\pm 90^\circ$ or place another slit configuration on the beam line. However if the second slit configuration is close to the other one, the obtained AD can have a special behavior. This setup is called DR interferometer.

[3]In this case, the effects of the horizontal divergence, ε' and the horizontal beam size, ε are the non-separable pair.

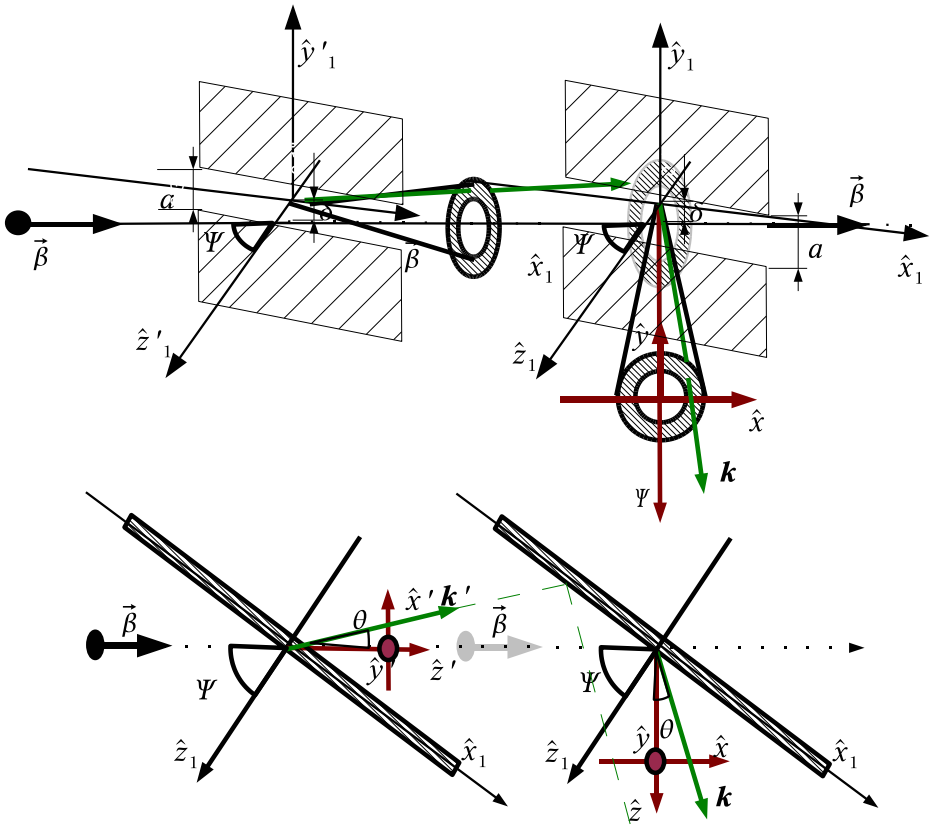

Figure 21: Diffraction radiation interferometer from two slit targets in parallel orientation respect to the plane of incidence

To measure beam divergence, one possibility is to use interference of DR produced from two slits inclined at 45° with respect to the beam trajectory in a configuration which is a direct DR analogy of TR interferometer developed by Wartski [49]. The idea is that the forward DR from the first slit reflects the second slit surface and interferes with the backward DR produced from the second slit [17]. Such a configuration

is shown of Figure 21, where the slit orientation is parallel respect to the plane of incidence.

The angular distribution created by the DR interferometer is a product of the individual ADs and the so called interference term. The interference term is coming from the difference in phase between forward and backward DR. The expression of the angular distribution obtained from a DR interferometer can be written as

$$\frac{\mathrm{d}^2 N^{(I)}_{horz.;vert.}}{\mathrm{d}\Omega \mathrm{d}\omega} = 4 \frac{\mathrm{d}^2 N^{(S)}_{horz.;vert.}}{\mathrm{d}\Omega \mathrm{d}\omega} \sin\left(\frac{L}{2L_V}\right), \tag{68}$$

where the superscript I refers to the DR interferometer (e.g. two slit configuration, or IDR), and S refers to the individual slit angular distribution and L is the path length between the two slits. The term L_V is the coherence length in vacuum for TR and DR,

$$L_V = \frac{\lambda}{\pi} \times (\gamma^{-2} + \theta^2)^{-1}, \tag{69}$$

which express the distance over which the particle's field and the TR or DR photon differ in phase by one radian.

The effects of divergence and beam size on the angular distribution of IDR can be obtained by convolutions of Equation 68 with distributions of beam angles and beam sizes. These calculations were performed numerically. The results are shown on Figure 22, where (a) represents the effects from varying the beam sizes and (b) shows the effects of divergence on AD from IDR. We used the same parameters as earlier, $\gamma = 45$, observation wavelengths $\lambda = 600\mu m$, slit opening $a = 1mm$ for both slits and the two slit separation, L, is $25cm$.

The advantage of the DR interferometer clearly manifests on Figure 22. While the beam size has nominal effects on the angular distribution, the divergence effects have increased sensitivity on the AD from IDR, and also meaning the divergence effects is completely separated from the beam sizes. The increased sensitivity is due to the sinusoidal term in Equation 68, which determine the visibility of interference fringes and it is independent of beam size effects. Measurements of the two polarized components of IDR can be used to determine orthogonal components of beam divergence, as is the case with interference TR [50].

Unfortunately the DR interferometry is not part of this dissertation work, however we can clearly see its advantage over the single slit experiment.

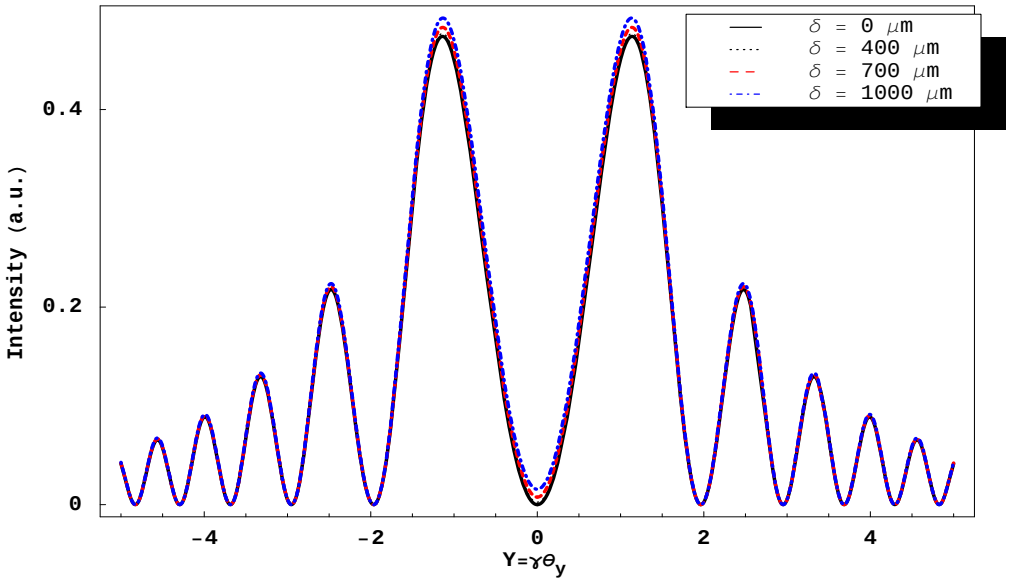

(a) The vertical component of IDR vs. beam size .

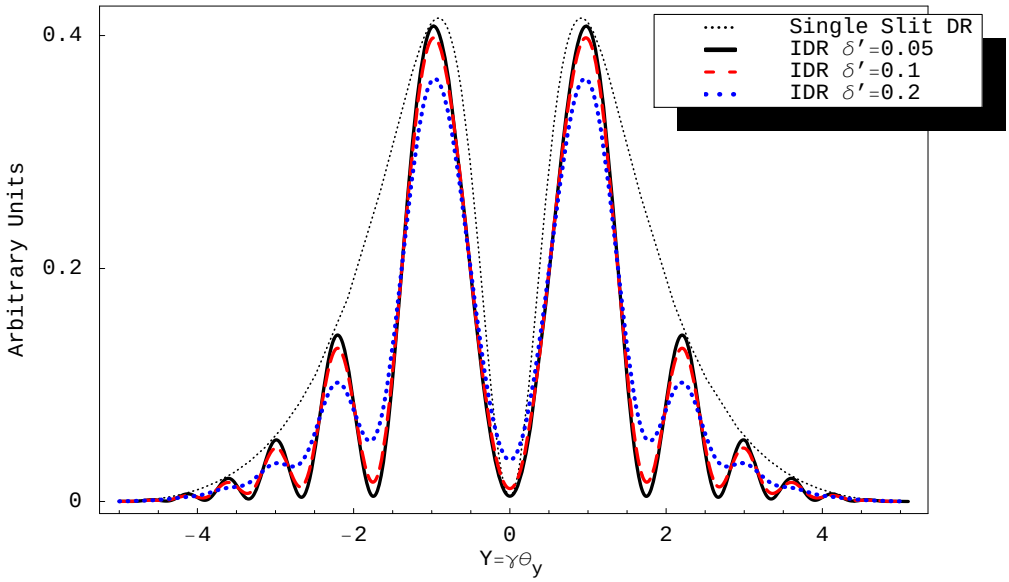

(b) The vertical component of IDR vs. divergence.

Figure 22: Effect of the beam size, δ, and the vertical divergence, δ' on the angular distribution of IDR. The parameters used in the simulation: $\gamma = 45$, observation wavelengths $\lambda = 600\mu m$, slit opening $a = 1mm$ and the two slit separation is $25cm$.

2.5 Radiation from electron bunches and coherent radiation

In this section we will investigate the effects of beam sizes on the radiation spectrum based on R. Lai and A.J. Sievers works [29, 26].

2.5.1 Coherent radiation

The total radiation spectrum[4] emitted from a bunch of charged particles can be calculated by adding all the radiation fields from each particle. Let consider a bunch of N identical particles, all with the same velocity and their positions are $\boldsymbol{r}_i'(t) = \boldsymbol{r}_0(t) + \boldsymbol{r}_i$, where $\boldsymbol{r}_i$ is the position vector from the center of the bunch, $\boldsymbol{r}_0$, to the i^{th} particle. Thus the radiation field becomes

$$\boldsymbol{E}_{total}(\omega) = \sum_{i=1}^{N} \boldsymbol{E}_i(\boldsymbol{r}_0, \omega)\, \mathrm{e}^{-i\boldsymbol{k}_i \boldsymbol{r}_i}, \tag{70}$$

where $\boldsymbol{k}_i = k * \boldsymbol{n}_i \equiv \omega * \boldsymbol{n}_i / c$ is the wavevector of the i^{th} particle with the direction, $\boldsymbol{n}_i$, to the observer. Using far-field approximation, $\boldsymbol{n}_i = \boldsymbol{n}$ and $\boldsymbol{E}_i(\omega) = E_i(\omega)\boldsymbol{n}$, the total radiation spectrum can be written as

$$\begin{aligned} I(\omega) &= I_s(\omega) \left| \sum_{i=1}^{N} \exp\left(-i\omega \frac{\boldsymbol{n}\boldsymbol{r}_i}{c}\right) \right|^2 \\ &= I_s(\omega) \sum_{i=1}^{N} \exp\left(-i\omega \frac{\boldsymbol{n}\boldsymbol{r}_i}{c}\right) \sum_{j=1}^{N} \exp\left(i\omega \frac{\boldsymbol{n}\boldsymbol{r}_j}{c}\right), \end{aligned} \tag{71}$$

where $I_s(\omega)$ is the single particle spectrum. The double sum yields unity for each $j = i$ term so the above equation becomes

$$I(\omega) = I_s(\omega) \left[N + \sum_{i \neq j}^{N} \exp\left(i\omega \frac{\boldsymbol{n}(\boldsymbol{r}_i - \boldsymbol{r}_j)}{c}\right) \right]. \tag{72}$$

[4]Note that, we do not specified what kind of radiation was created, it can be transition, diffraction, synchrotron or even Smith-Purcell radiation.

In continuum limit, the positions of the electrons are described by the bunch distribution. The bunch distribution, $\rho(\boldsymbol{r})$ is the probability density for the particles at the position $\boldsymbol{r}$ from the center. So the number of particles in the infinitesimal cube between $\boldsymbol{r}$ and $\boldsymbol{r} + \mathbf{d}\boldsymbol{r}$ is $\mathrm{d}N = \rho(\boldsymbol{r})\mathrm{d}^3\boldsymbol{r}$, then Equation (72) can be written as

$$I(\omega) = I_s(\omega)\left[N + N(N-1)\iint \rho(\boldsymbol{r})\rho(\boldsymbol{r'})\exp\left(i\omega\frac{\boldsymbol{n}(\boldsymbol{r}-\boldsymbol{r'})}{c}\right)\mathrm{d}^3\boldsymbol{r}\mathrm{d}^3\boldsymbol{r'}\right]. \quad (73)$$

If we now define the form factor $f(\omega)$ as the Fourier transform of the bunch distribution

$$f(\omega) = \int \rho(\boldsymbol{r})\exp\left(i\omega\frac{\boldsymbol{r}\cdot\boldsymbol{n}}{c}\right)\mathrm{d}^3\boldsymbol{r} \quad (74)$$

the radiation intensity from a bunch of N particles, Equation 73, can be written in a simpler form of

$$I_{total}(\omega) = NI_s(\omega) + N(N-1)\left|f(\omega)\right|^2 I_s(\omega). \quad (75)$$

Let $N \gg 1$, then there are two important cases, when

- the frequency is sufficiently high (wavelength much smaller than bunch size), the form factor vanishes and $I_{total}(\omega) = NI_s(\omega)$. This is the case of incoherent radiation.

- at low frequencies (wavelength longer than the bunch size), $f(\omega)$ approaches to unity and thus $I_{total}(\omega) = N^2 I_s(\omega)$. This radiation is called coherent.

Note that, the form factor depends on the direction $\boldsymbol{n}$ of the observer. To simplify the problem we assume separable bunch distribution to longitudinal and transverse parts

$$\rho(\boldsymbol{r}) = \rho_{\parallel}(\boldsymbol{z})\rho_{\perp}(\boldsymbol{r}_{\perp}). \quad (76)$$

If θ is the angle between $\boldsymbol{n}$ and the beam trajectory (along the z axis), then $\boldsymbol{n}\cdot\boldsymbol{z} = z\cos\theta$ and $\boldsymbol{n}\cdot\boldsymbol{r}_\perp = r_\perp \sin\theta$ and the form factor becomes

$$f(\omega,\theta) = \int \rho_\perp(r_\perp)\, \mathrm{e}^{i\omega r_\perp \sin\theta/c}\mathrm{d}r_\perp \cdot \int \rho_\parallel(z)\, \mathrm{e}^{i\omega z\cos\theta/c}\mathrm{d}z. \tag{77}$$

In cylindrical coordinate systems the bunch distribution can be expressed as

$$\rho(\boldsymbol{r}) = \rho_\parallel(\boldsymbol{z})\rho_\perp(\boldsymbol{r}_\perp) = h(z)g(\rho,\phi). \tag{78}$$

The form factor, using the above equation and assuming azimuthal bunch symmetry, has the following form [41]

$$f(\omega,\theta) = 2\pi\int_0^\infty g(\rho)J_0(i\omega\rho\sin\theta/c)\rho\mathrm{d}\rho \cdot \int_\infty^{-\infty} h(z)\, \mathrm{e}^{i\omega z\cos\theta/c}\mathrm{d}z, \tag{79}$$

where $J_0(u)$ is the zero order Bessel function.

In most cases, the effects from transverse beam size is negligible to the form factor, however we should investigate its validity. If we assume Gaussian transverse distribution

$$g(x,y) = \frac{1}{2\pi\sigma_\rho^2}\, \mathrm{e}^{-(x^2+y^2)/2\sigma_\rho^2} \tag{80}$$

and also Gaussian longitudinal distribution

$$h(z) = \frac{1}{\sqrt{2\pi}\sigma_z}\, \mathrm{e}^{-z^2/2\sigma_z^2}, \tag{81}$$

the expression for the form factor becomes a simple equation as

$$f(\omega,\theta) = \mathrm{e}^{-\left[(\omega\rho\sin\theta/c)^2+(\omega z\cos\theta/c)^2\right]}. \tag{82}$$

By look at the above form factor, one can see that the transverse distribution is negligible if

$$\rho\sin\theta \ll z\cos\theta \tag{83}$$

condition is valid. In our case the typical bunch length is $300\mu m$ and the transverse beam size is around $800\mu m$. If we choose $1/\gamma$ (16 mrad for 30 MeV beam) as the observation angle, e.g. the maximum intensity, the Equation (83) is roughly fulfilled ($12.79\mu m$ vs. $299.96\mu m$)[5]. Thus from now on we assume negligible transverse beam size in the determinations of bunch lengths.

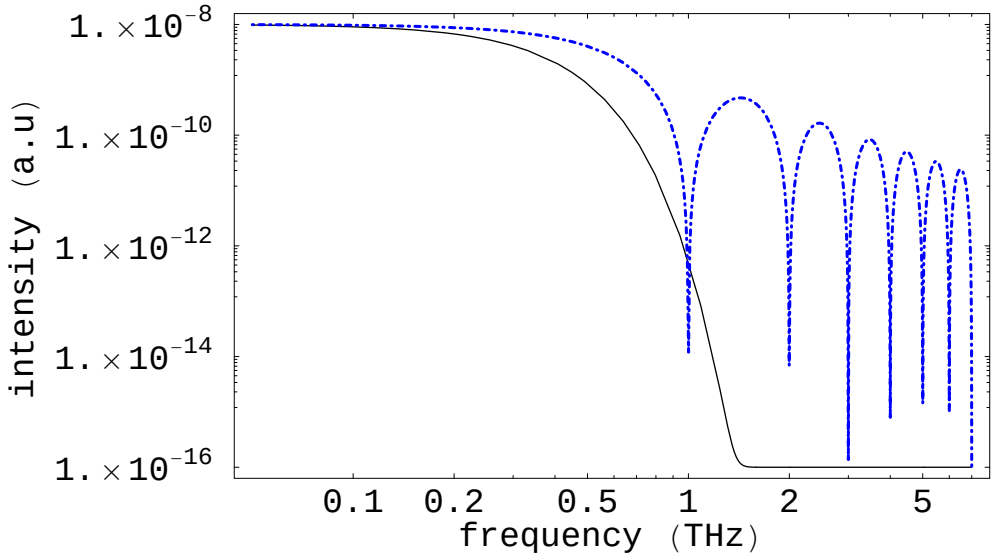

Figure 23: Coherent transition radiation spectrum from 50 MeV Gaussian (solid - $FWHM = 2\sigma_z\sqrt{2\ln 2} = 1ps$) and rectangular (doted - $l = 1ps$) electron beams

At the end of this section let see an example for coherent radiation spectrum. To simplify our case first we use TR as the radiation type generated by each particle, since this radiation is independent of frequency, $I_s(\omega) = I_s^{TR}$. We assume two dif-

[5]However in our experiment we collect the radiation in much bigger angles the spectrum is still dominated by the longitudinal form factor, since high proportion of the radiation intensity is distributed in a small angle around the z axis. Nevertheless, latter one should investigate the effect of transverse beam size contribution to the bunch length measurements.

ferent bunch distributions, Gaussian and rectangular. The form factor for Gaussian distribution becomes

$$f(\omega) = e^{-(\omega\sigma_z/c)^2}, \tag{84}$$

while the form factor from a rectangular bunch profile is

$$f(\omega) = \left[\frac{\sin(\omega l/2c)}{\omega l/2c}\right] \tag{85}$$

where l is the width of the beam. The typical number of electrons in a bunch generated by the Vanderbilt FEL is in the order of 10^8 and the average beam size is around $300\mu m$ or $1ps$. The obtained spectrum is shown on Figure 23.

As we know at wavelengths longer or comparable to the electron bunch length, the radiation emitted from the bunch is coherent. In our case these wavelengths are in the range of 300μm and longer or in frequency range of 1THz or smaller. This range is called far-infrared or FIR.

However using diffraction radiation as the base of the coherent effect the frequency independence is not valid anymore. As we saw earlier (see Equation 39.) the DR fluence depends on the observation wavelength. In this case the coherent spectrum can be more complicated. To obtain the bunch profile this effect has to be included to avoid misinterpreted results. Such dependence is shown on Figure 24. The figure shows different DR conditions with the same beam sizes. By analyzing the results shown on Figure 24 we can find that, if we ignore the DR effects we would measure different (longer) bunch lengths than the real ones. So it is very important to include these effects in the bunch length analysis. However in so many conditions these effects are very small.

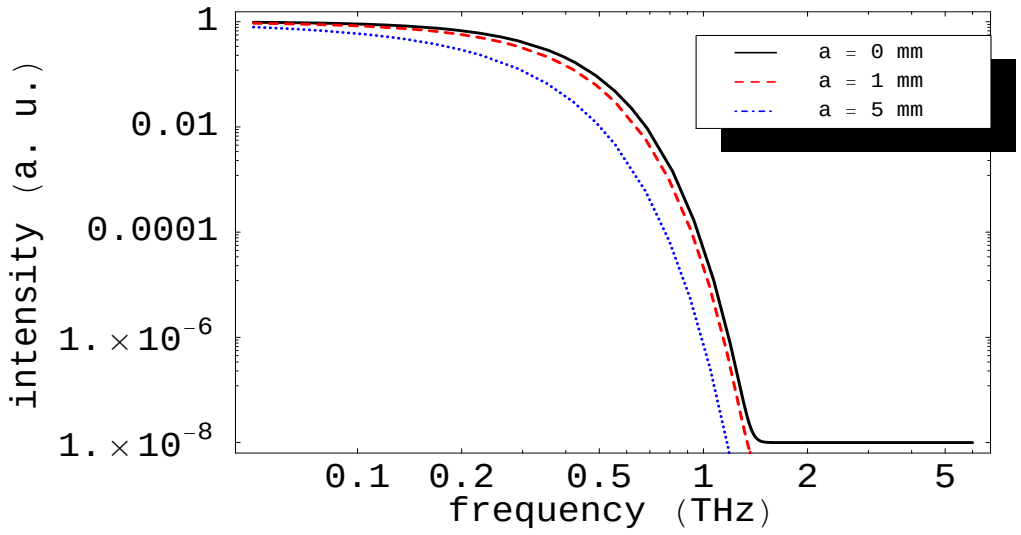

Figure 24: Coherent diffraction radiation spectrum from 50 MeV Gaussian electron beams at different beam center positions from the target edge.

2.5.2 Bunch length measurement and Kramers-Kronig analysis

As we saw in the previous section the coherent radiation spectrum is depend on the bunch length via the form factor through Equation (75), since the bunch form factor is the Fourier transform of the longitudinal bunch profile ρ(z)

$$f(\omega) = \int \rho(z)\, \mathrm{e}^{\mathrm{i}\omega z/c} \mathrm{d}z\,. \tag{86}$$

By measuring the spectrum of the coherent radiation one can obtain the longitudinal bunch profile by a simple inverse Fourier transformation. However it is not so simple, since the power spectrum $I(\omega)$ depends on the modulus of the form factor only, the phase of the $f(\omega)$ is unknown. The problem is lying in the fact that the Fourier transform of any asymmetric bunch distribution has a non-vanishing imaginary part. There is a solution to obtain the missing phase. Since the imaginary part of complex

distributions is not completely independent from its real part, the minimal phase can be reconstructed by the so called Kramers-Kronig relations [29]

$$\Psi(\omega) = -\frac{2\omega}{\pi}\int_0^\infty \mathrm{d}x \frac{\ln|f(x)/f(\omega)|}{x^2-\omega^2}. \tag{87}$$

With the knowledge of the minimal phase the normalized bunch distribution or bunch profile can now be obtained from an inverse Fourier transform

$$\rho(z) = \frac{1}{\pi c}\int_0^\infty \mathrm{d}\omega f(\omega)\cos\left[\Psi(\omega) - \frac{\omega z}{c}\right]. \tag{88}$$

However the reconstruction process using the Krames-Kronig method has some obscurities. To demonstrate these limitations we assumed a three Gaussian bunch distribution. We calculated the form factor from that, and we tried to obtain the bunch distribution back using the Kramers-Kronig analysis. Our results are shown on Figure 25. The Kramer-Kronig analysis was not able to reconstruct the original bunch profile in some cases. Note that, some distribution leads to the same form factor[6] so the above results is what we should expect.

Therefore, this analysis cannot fully retrieve the original bunch profile and some other method is needed to verify the output from the Kramers-Kronig reconstruction. This can be a streak camera or similar device. Unfortunately, due to their high price tag our lab does not have such a device. Other possibility is to use more sophisticated technique to obtain the amplitude and the phase of the radiation spectra, examples are the Frequency Domain Phase Measurement (FDPM) [51] and the Frequency Resolved Optical Grating (FROG) [52]. However these techniques are not fully developed or

[6] At least in their real part. The imaginary part of course different, However, as noted earlier, we are able to measure the real part of the complex form factor.

available in the Far-Infrared frequency range.

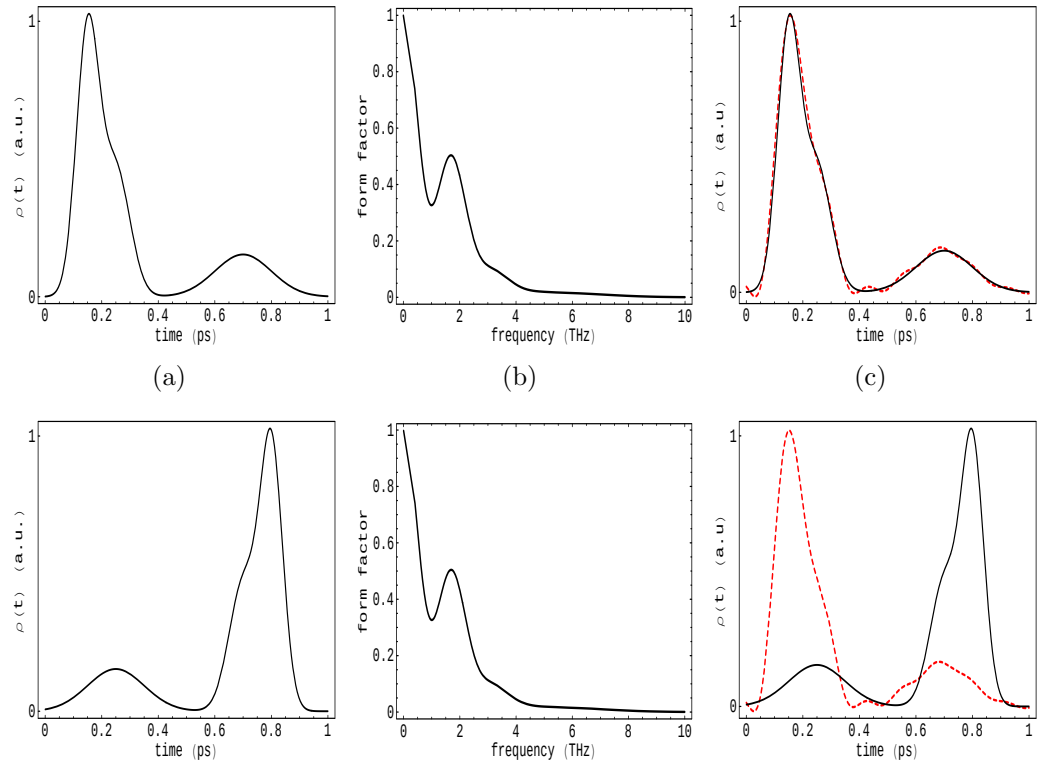

Figure 25: Limitation of bunch shape reconstruction process using Kramers-Kronig methods, the initial bunch profile (a,d); the form factor(b,e); reconstructed profile (dashed line) along with the original profile (solid line) (c,f).

CHAPTER III

EXPERIMENTAL APPARATUS

In this chapter we introduce the facility where our experiments were conducted and give a short review of the bunch generation and beam properties. We will present the experimental apparatus along with some basics of interferometry measurements.

3.1 W. M. Keck FEL Center

The W. M. Keck FEL Center at the Vanderbilt University is the home of our experimental series. The FEL facility has a Mark III type linear accelerator with average beam current of 150 mA and beam energy between 20-45 MeV.

The facility's schematic diagram is shown on Figure 26, as well as the station, where the experiments are placed.

The accelerator is very similar to the Stanford University Mk III FEL. The electron source is an RF gun, a Cu microwave cavity with a thermionic cathode operated at 2857 MHz. The cathode is LaB_6 crystal button with a 1.78 mm diameter (Kimball Physics Inc., ES440), heated with DC current to about 1800 K. Since not all the electrons leave the cavity before the electron field reverses direction, the rest are turned back and some hit the cathode causing uncontrolled "backheating". To minimize this effect, the beam is bent in the vertical plane by an unusually shaped magnet on the cathode and two following dipole magnets are used to straighten the beam out [53].

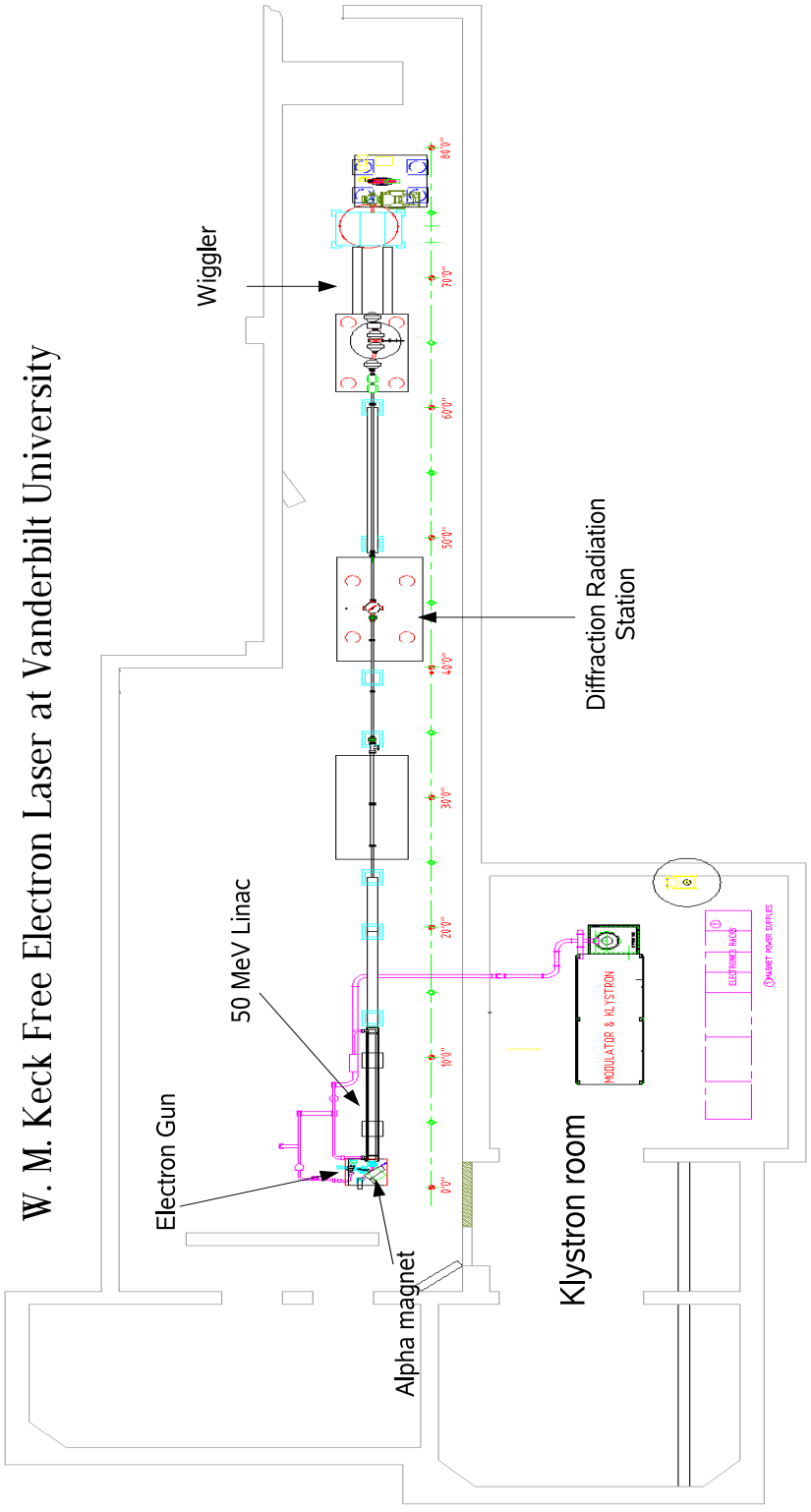

Figure 26: W.M. Keck FEL at Vanderbilt University - schematic layout.

At the exit point of the RF gun, the electrons have gained a maximum momentum of about 1.1 MeV/c. However the electrons have momentum spread from 0 to 1.1 MeV/c as they exit from the cavity, due to modulation by the RF phase during their emission.

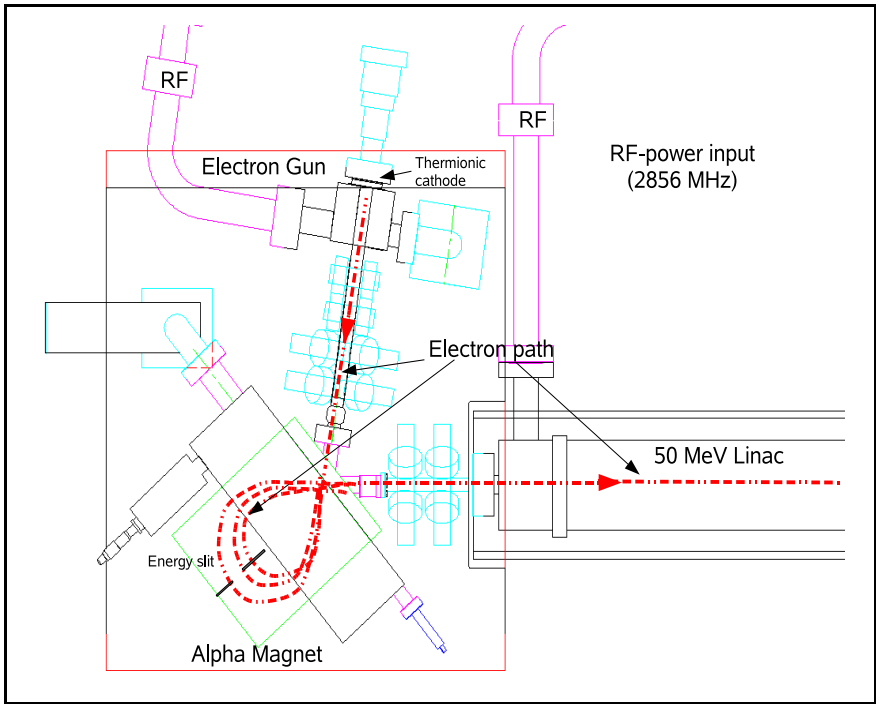

Figure 27: Schematic diagram of the electron source (rf-gun) and the alpha magnet.

The bunch immediately enters an alpha-magnet and follows an α-like path and exits again at the entrance point. In the alpha magnet there is a momentum filter or slit. The slit blocks the electrons with too low or too high momenta, see Figure 27.

The alpha magnet also acts as a bunch compressor: the higher energy particles follow longer path, while the lower energy particles follow shorter ones. The compressed bunch now has a momentum distribution from 0.9-1.1 MeV/c and a short

bunch length, so it can be efficiently accelerated to higher energies.

The filtered and compressed electron bunch is then accelerated to its final energy in a 3 m long single section S-band linear accelerator (LINAC). The LINAC has 86 cells plus one entrance and one exit cavity for the RF.

Nevertheless the bunch spreads out as it travels through the beam line due to some inequality in the electron momenta. At the end of the beam line the electron bunch enters a Wiggler to create photons and finally it will be dumped.

The PARMELA simulation of the acceleration process indicates that the bunch leaving the RF gun is about 1.1 cm long (35 ps) and after the LINAC is about 1.0 ps (FWHM).

3.1.1 The electron beam

Table 1: FEL parameters

Characteristic of the W.M. Keck FEL electron beam	
Maximum Energy	45 MeV ($\gamma = 80$)
Beam emittance	
Vertical	10π mm·mrad
Horizontal	30π mm·mrad
Beam size	
Vertical	0.5 mm
Horizontal	1-2 mm
Bunch length	1 ps or 0.3 mm
Single bunch population	3×10^8
Energy spread	0.50%

The beam parameters of the Vanderbilt FEL are shown on Table 1. The highest energy is 45 MeV, however most of the experiments were conducted at 30 MeV.

The time structure of the beam is complex, built up from macro- and micropulses. A macropulse is about 6 μs long, and the separation between two macropulse is adjustable from 1 s to 33 ms. Within each macropulse, there are micropulses, or bunches, repeated at the RF frequency of 2857 MHz. Therefore the spacing between each bunch is 350ps, or 10.5 cm in length, and each bunch consists about 10^8 electrons or 50 pC charge. One macropulse contains about 23,000 bunches. The summarized structure of the beam is shown in Figure 28.

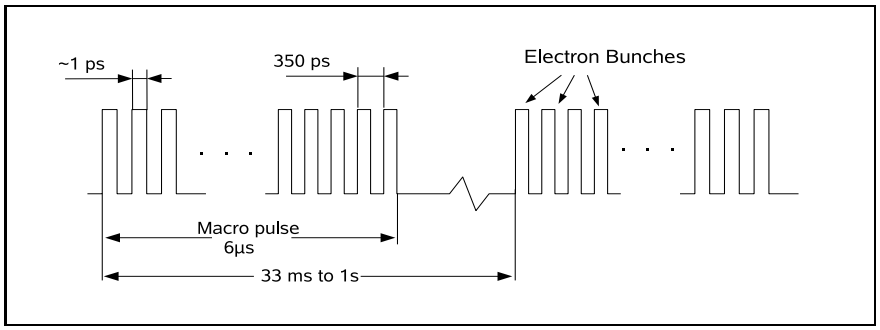

Figure 28: Vanderbilt FEL macropulse and micropulse structure

3.2 The radiation target

To study the diffraction radiation as well as the transition radiation a special target was developed at the Vanderbilt FEL. The idea was to design a movable slit so when the slit is closed TR is generated, when opened DR is generated. The movable slit is also allowing us to investigate DR under different conditions, e.g. different

opening width.

The slit design is shown on Figure 29. The slit plates are driven on two parallel axles. These axles are rotated by a stepping motor via a couple of gears, which move the two plates up and down, causing the slit to close, or by changing the direction of rotation, to open. Since the slit is in vacuum a special transmission was designed to actuate the slit-movement from outside of the vacuum chamber. The stepping motor works in air and its steps are controlled by a microcontroller and computer. The movement of the slits is calibrated. The smallest step is $1.25\mu m$ and the slit can be opened as wide as 10 cm. However during operation we had many problems in closing the slit perfectly and opening it after closing. These problems are related to the connection between the axles and the target plate holder by screws that are subject to jamming very easily in vacuum.

For the target screen we used two 3" silicon wafers with thickness of $500\mu m$. These wafers are not just very flat but rigid as well, so bending and surface problems are minimal, however not negligible (see later in Chapter 5 in more detail). To increase the reflection of these wafers, as well as the DR(TR) intensity generated via these plates, we have gold-coated these wafers. The gold coating is around $1\mu m$ thick. One screen is mounted on an adjustable frame so the co-planarity can be kept.

The slit is oriented near 45° to the beam trajectory, but the screen holder position is not in the center of the slit chamber. The offset is around 30 mm, in this case the outgoing radiation makes an angle larger than 45° to the slit plane (around 50°).

Recently a new slit assembly was developed to solve all these problems including

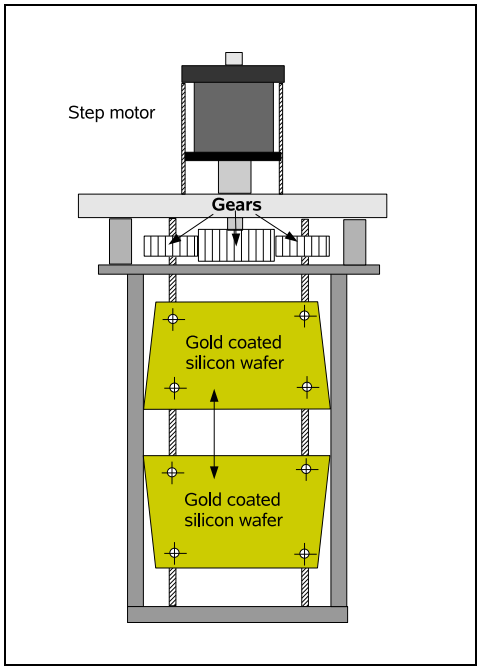

(a)

(b)

(c)

Figure 29: Slit assembly. a.) Schematic view of the movable slit design. b-c.) Pictures of the slit plates and the slit assembly. The plates are 3" silicon wafers with thickness of $500\mu m$ with $1\mu m$ thick gold coating.

some others that showed up during operation, such as centering the beam. In addition, the new model is capable of moving the two plates independently.

3.3 Detectors

The most common detector types used in the far-infrared frequency range are pyroelectric detectors, photonmultipliers, Golay-cells and bolometers. Our lab is equipped with two pyroelectric detectors from Molectron Inc. (P4-45) and one Golay-cell detector from QMC Ltd. Since we used both in our measurements these two types of detectors will be described in this section.

3.3.1 Pyroelectric detector

The most common far IR detector is the pyroelectric detector, due to its simplicity and low price. The detector consist two separable parts; the amplifier and the pyroelectric sensor. Two different type of pyroelectric crystals are commonly built into these detectors; Lithium-Tantalate ($LiTaO_3$) or the slightly expensive Deuterated Triglycine Sulphate (DTGS). When a pyroelectric crystal absorbs the FIR radiation, it will heat up, expand and finally generate a polarization current [54]. By measuring this polarization current the incident radiation energy can be determined.

Our pyroelectric detectors are made by Coherent Inc, Type P4-45, and they use ~ 130 μm thick $LiTaO_3$ crystals. During our experiment we found a strange behavior with these detectors. Multiple reflections in the crystal can cause some interference behavior and deform our measured radiation spectrum. These problems were

confirmed by other groups as well, and they managed to even measure the index of reflection of the $LiTaO_3$ crystal in the FIR range with result in accordance with theoretical calculations [41]. Due to interference effect the determination of the real radiation spectrum can be very complicated. Moreover in our experiment we found many other components, which can cause a very similar interference effects. We will discus those in later in this work. To avoid these problems we do not used the pyroelectric detectors to obtain the radiation spectrum.

3.3.2 Golay-cell detector

The primary detector in our experiment is a Golay-cell (OAD-7, from QMC Instruments Ltd.). Golay-cell detectors have a very unique operation principle to detect radiation intensity.

The name OAD stands for Optical Acoustic Device. In the detector there is a sealed, gas-filled absorption chamber, an optical microphone section, and a preamplifier. A sketch of a Galay detector is shown on Figure 30.

If a radiation passes through the window of the device (1) and is incident upon the semi-transparent film (2) located in the center of a sealed chamber, the energy absorbed in the film heats the gas in the chamber, causing the pressure to rise. This pressure change distorts the membrane (3) forming the wall of the chamber. A light emitting diode (LED) (8) sends a signal through re-focusing optics (5) and onto the mirrored back surface of the chamber containing the absorbing membrane. This radiation is reflected back through the lower half of the optics via a grating as shown

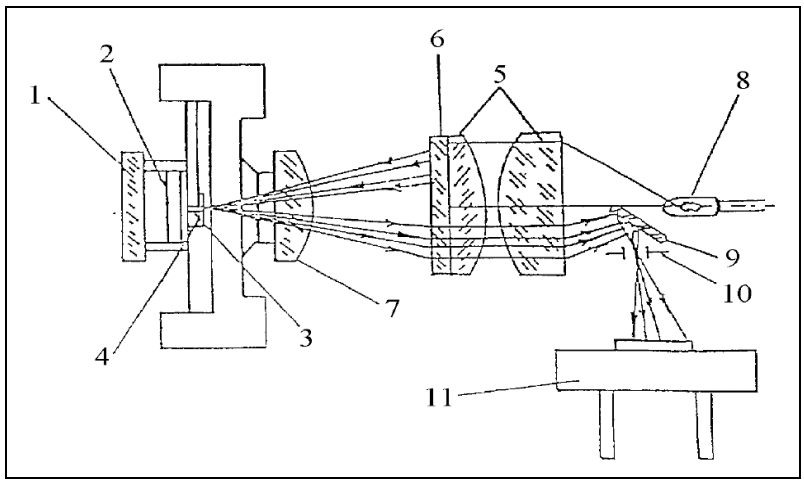

Figure 30: Schematic view of the Golay-cell detector. (1) Diamond window; (2) semi-transparent film; (3) membrane; (4) gas chamber; (5) refocusing optics; (6) collimator; (7) lens; (8) LED, (9) grating; (10) collimator; (11) photodiode [55].

on the Figure 30, and re-focused onto a photodiode (11).

The degree of illumination of the photodiode by radiation from the LED is a function of the shape of the front chamber and a function of the entered radiation energy [55].

Our detector has a 6mm diameter diamond window. It is designed to respond to signals at wavelengths in the range from 1μm up to a few millimeters. Due to the diamond window the Golay-cell's responsivity is almost a perfect flat curve in these wavelengths.

The Golay detector's responsivity is much higher than that of any pyroelectric detectors, in numbers it means, 33kV/W for the Golay cell and 4kV/W of average responsivity for the pyroelectric detectors [55, 56].

Golay cell detectors, however, cannot be exposed to high radiation power to avoid the damage of the absorbing membrane. The maximum power that the unit can

handle is less then 10μW.

Also due to its mechanical operation the Golay detector is very sensitive to vibration. Vibration can be caused by the translation stages and stepping motors.

3.4 Interferometer

To obtain the generated radiation spectral intensity we used conventional Michelson interferometer.

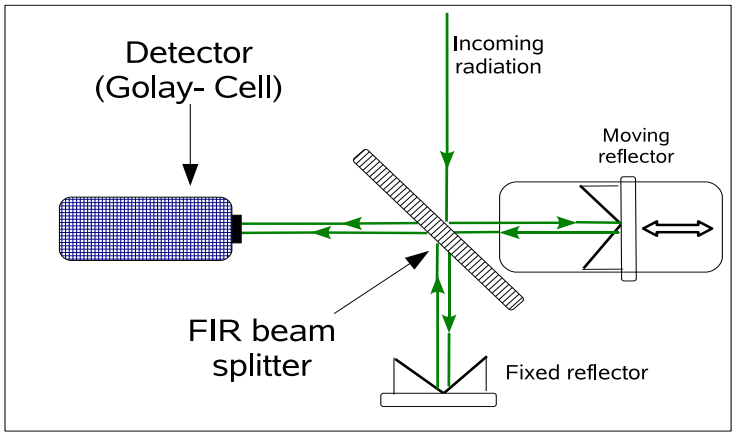

Figure 31: A sketch of a Michelson-type interferometer.

A simple diagram of a Michelson interferometer is shown on Figure 31. The incoming radiation is split into two parts by a beam splitter. Both parts are then reflected back from the retroreflectors[1] and recombine at the beam splitter. The combined radiation then enters to the detector.

[1] A retroreflector is a device that sends light or other radiation back where it came from regardless of the angle of incidence, unlike a mirror, which does that only if the mirror is exactly perpendicular to the light beam.[22]

The beam splitter used in our experiments is specially made for far-infrared radiation (THz beam splitter, Radiabeam Inc.). The retroreflectors are made from three mutually perpendicular mirrors which form a corner (corner reflector).

One of the retroreflectors is movable by a motorized high precision translator, so the relative path length of the two combined beams can be changed. As the moving mirror changes positions, it causes the waves that compose the far-infrared radiation beam undergo constructive and destructive interference when they recombine at the beamsplitter, producing an interferogram, a plot of the detector response, intensity(usually in volts) vs. the position of the moving mirror or retardation (in seconds).

If the optical path difference is δ, then the electric field of the radiation is sum of two fields, the field from the fixed mirror, $E_f = RTE(t)$, and the field from the moving mirror with a delayed time of δ/c, $E_m = TRE(t + \delta/c)$, where T is the transmission and R is the reflection coefficient of the beam splitter. Consequently, the radiation intensity measured by the detector as function of path difference is

$$\begin{aligned} S_D(\delta) &\propto \int \left| RTE(t) + TRE\left(t + \frac{\delta}{c}\right) \right|^2 \mathrm{d}t \\ &= 2\int |TR|^2 E(t)E^*\left(t + \frac{\delta}{c}\right) \mathrm{d}t + 2\int |TRE(t)|^2 \mathrm{d}t \end{aligned} \tag{89}$$

The first term of the above expression is the well known autocorrelation function, while the path difference independent second term is just the background or baseline. Therefore an interferogram is just a representation of the autocorrelation function. Due to the properties of the autocorrelation, the radiation power spectrum is then the Fourier transformation of the interferogram [38].

The Michelson interferometer is just one type out of many designs, and its advantage is the simple structure. The other common type of interferometers is the Martin-Puplett design. The Martin-Puplett interferometer uses two detectors and at least two polarizers. One detector is recording the interferogram while the second one is normalizing the measurement. This feature is very useful if the beam charge or other accelerator parameters are not stable. Since we have only one Golay detector, we used the Michelson design. Originally we have constructed a Martin-Puplett interferometer using two pyroelectric detectors, however due to the internal interference problem of these detectors we decided not to use them.

3.5 Layout of the longitudinal bunch shape measurements

On the beam line, all our experiments are placed on the 2nd Station (see Figure 26). For the longitudinal bunch shape measurements we used the Michelson-type interferometer, described earlier, to obtain the radiation interferograms and (from it) the power spectrum. The schematic drawing of the experimental setup is shown on Figure 32.

The slit is placed in the center of a 6 port chamber with 2 quartz crystal output windows. The generated DR(TR) radiation leaves the chamber trough the quartz window, with $\sim 50^\circ$ angle respect to the beam line, as we mentioned earlier. The radiation is then collimated with a 7" focal length parabolic mirror with 1" diameter. The parabolic mirror is placed one focal length below the radiator and its focal length aligns at the center of the slit. Such an alignment can convert the divergent radiation

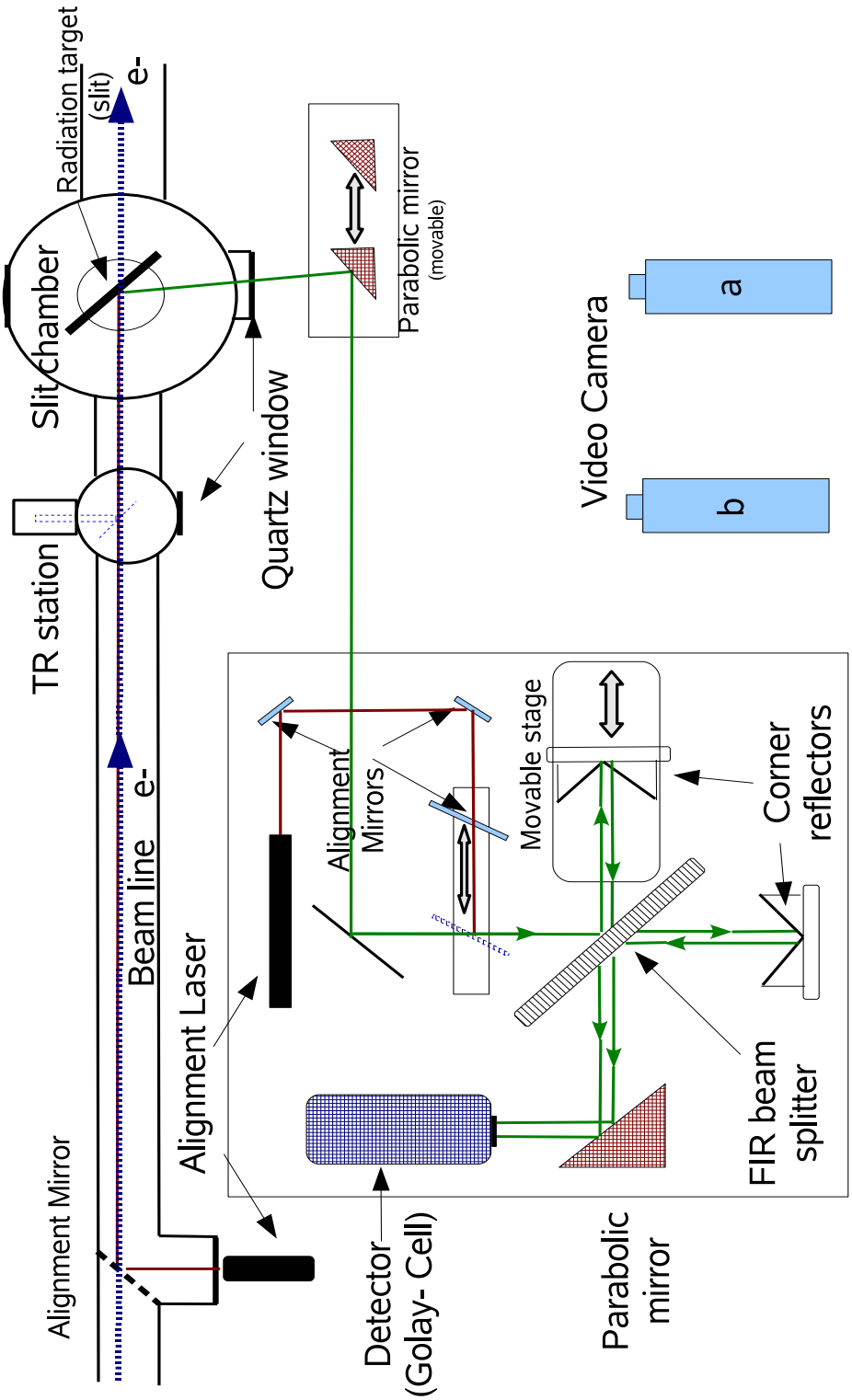

Figure 32: Experimental setup of the bunch length and shape measurement.

into a parallel beam. The collimated and parallel radiation beam is then projected into the Michelson interferometer trough a three mirror periscope, which is placed 120 cm away from the parabolic mirror. The periscope is used to lower the DR radiation from the beam line by 3" and to drive the radiation into the optical center of the interferometer. The dimensions of the mirrors used in the periscope are 2" $\times$ 3". In the interferometer we used an additional 6" focal length parabolic mirror to focus the radiation into the Golay detector.

We used two optical lasers to alignment the components of the experiment . The first laser light follows the electron beam trajectory and is reflected out from the beam line from the slit plates (closed position) into the interferometer via the parabolic mirror and the periscope. The second laser light is used to alignment the components of interferometer. By placing an additional movable beam splitter in front of the interferometer's beam splitter we are able to use this laser light not only to align the interferometer itself but the whole system by overlapping with the other laser beam, (see Figure 32). During operation this alignment system is shut down, however we can align the electron beam to the laser path by using optical transition radiation and optical cameras. Two of the cameras are shown on Figure 32. One points to an OTR station to adjust the beam before the slit chamber, while the other is to adjust and check the electron beam position on the slit plates. Through the beam line there is a couple of more OTR stations to align the beam during operation.

3.6 Layout of the angular distribution measurements

To determine the transverse beam size and/or the beam divergence we must measure the angular distribution of the emitted DR(TR) radiation. To measure, or to map, the angular distribution of a given radiation emitted by bunch of electrons a detector array or CCD would be the best choice. If those are not available due to some problems, like in our case, due to the inefficient sensitivity in a given frequency range, the angular distribution can be measured by scanning with a single high sensitive detector. However this process is rather slow, single shot measurements cannot be performed. Since the most radiated energy is in the FIR range, due to the coherent effect, we used a Golay-cell detector on XY translation stage. The setup of this angular distribution measurement is shown on Figure 33.

We changed the Golay-cell original 6mm pupil to 2mm to achieve higher resolution. Unfortunately we cannot use too small pupil to increase scan resolution due to the weak radiation energy.

The distance of the detector and the radiation source have to be longer than the formation length, $L_f \approx \lambda\gamma^2/2\pi$, to avoid any deformations due to the near-field effect, as described earlier. For $\gamma = 66$ and radiation wavelength of 500 micron this distance means at least 35 cm from the radiator.

The XY stage contains two translation stages, each with maximum movement of 10 cm. Due to the maximum movement of these stages we cannot place them too far, otherwise we cannot obtain wide angular distribution. We expect at least $\pm 5 \times 1/\gamma$ angle scan in both horizontal (X) and vertical (Y) directions. At $\gamma = 66$ or $30\,MeV$

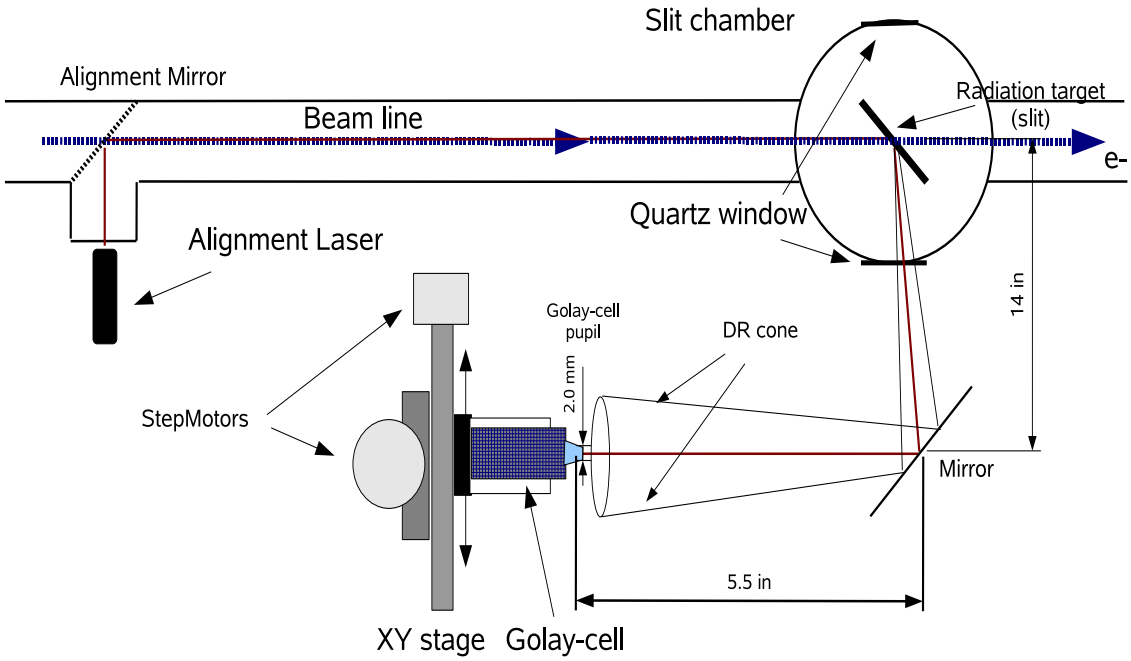

Figure 33: Experimental setup of the angular distribution measurement -the XY stage.

this means a maximum 59 cm (23") distance from the radiation source to the XY stage.

3.7 Translation stages and controllers

We used translation stages to move different components during the experiments like the moving retroreflector in the Michelson interferometer or the Golay detector in the angular distribution measurement. The translation stage in the Michelson interferometer is made by AEROTHECH (ATS-5025) and capable of moving as small as 0.1 μm in one step. To control this stage we used a Lindex 511 controller. The maximum movement of this stage is 4 cm. The two linear stages in the angular scan are made by Newport and its smallest steps are 0.5 mm with 10 cm maxi-

mum movement. These stages are controlled by programmable microcontrollers with ethernet interfaces (Rabbit Core-3700). Data recording, component controlling and synchronizing processes are made by a few computer programs written in LabView environment.

CHAPTER IV

MEASUREMENT OF THE RADIATION SPECTRUM AND THE ELECTRON BUNCH LENGTH

Let's briefly summarize how to measure bunch length. First we have to obtain the generated radiation spectrum, since as we proved earlier, the coherent radiation is closely related to the longitudinal charge density distribution via the bunch form factor. By measuring the coherent spectrum distribution, $I_{coh.}(\omega)$, the bunch form factor, $f(\omega)$ can be calculated using

$$|f(\omega)| \propto \sqrt{\frac{I_{coh.}(\omega)}{I_s(\omega)}}, \tag{90}$$

where I_s is the single-particle spectrum. Finally the charge distribution is computed from the Fourier transformation of the form factor

$$\rho(z) = \frac{1}{\pi c}\int_0^\infty \mathrm{d}\omega f(\omega)\cos\left[\Psi(\omega) - \frac{\omega z}{c}\right], \tag{91}$$

using the reconstructed minimal phase from the Kramers-Kronig relations

$$\Psi(\omega) = -\frac{2\omega}{\pi}\int_0^\infty \mathrm{d}x \frac{\ln|f(x)/f(\omega)|}{x^2-\omega^2}. \tag{92}$$

4.1 Interferogram

In the previous chapter we pointed out that the radiation spectrum can be measured with a Michelson interferometer, since the spectrum is the Fourier transformation of the produced interferogram. A sample interferogram that we measured using

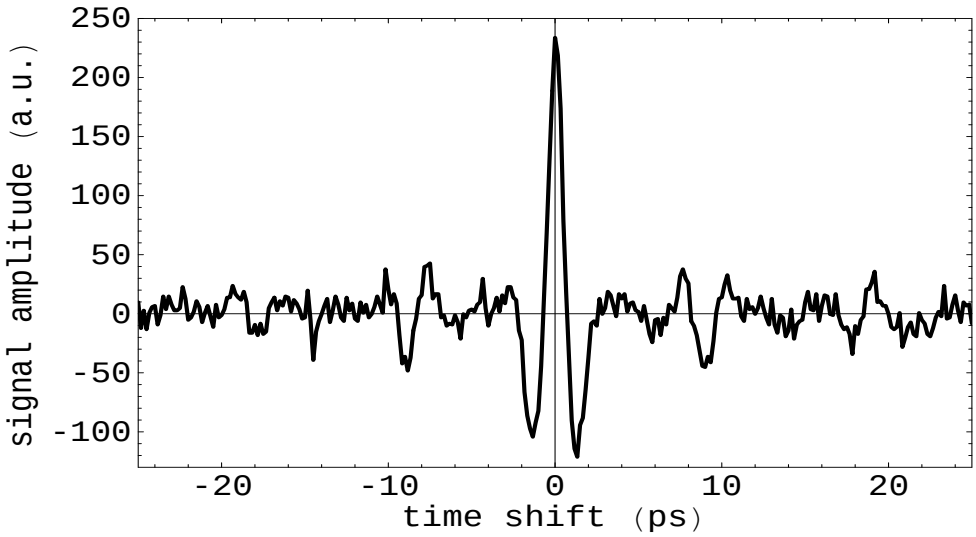

Figure 34: Interferogram of a coherent TR radiation obtained from the Michelson interferometer.

transition radiation (with closed slit) is shown on Figure 34.

The way to record an interferogram is to measure the amplitude of the radiation pulses for each position of the moving retroreflector. The highest amplitude point, or center burst, corresponds to the zero delay position. In general the zero level amplitude of an interferogram corresponds to the background or the base-level signal. First the interferogram is recorded as amplitude vs. position, but in general, the x-axis of an interferogram shows the time delay in picoseconds of the two interfere pulses in the Michelson interferometer, so we transformed it using $\Delta t = \Delta x/c$, where c is the speed of light.

In each position of the moving retroreflector we measure the FIR radiation intensity with a Golay cell detector. The detector output is connected to a HP oscilloscope and the measurement is triggered with the accelerator "kicking" pulse. A screen shot of the HP oscilloscope is shown on Figure 35. The screen shows the Golay output

signal together with the trigger and the reference detector signal output.

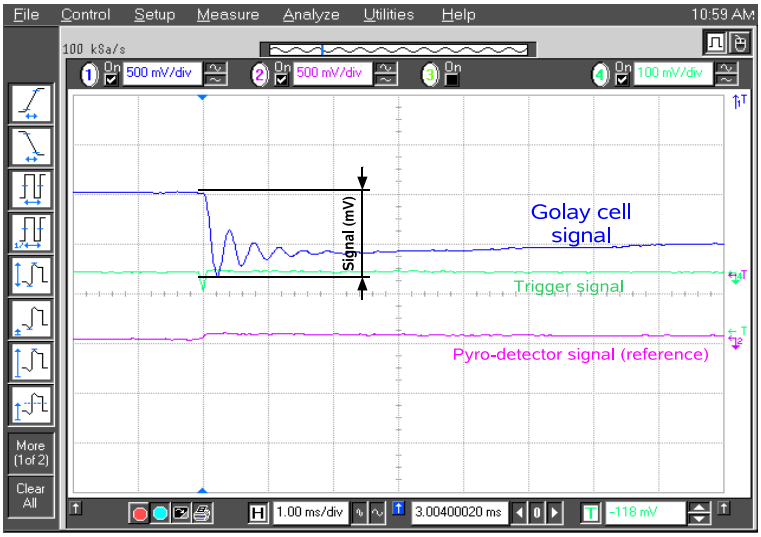

Figure 35: Detector signals during data acquisition on a HP oscilloscope.

The oscillation of the Golay cell signal, as we believe, is coming from the vibration of the absorber membrane. During data acquisition we record the Golay cell's peak to peak signal as the detector signal. As you can see on the oscilloscope's screen the Golay detector is much more sensitive than the pyroelectric detector.[1]

The recording process for the interferogram is quite time-consuming. To obtain an interferogram of 800 points given a linac repetition rate of 10 Hz, the scanning process takes about 30 minutes. Since the Golay cell is vibration sensitive, we have to power down the step motor of the translation stage at each data acquisition. This vibration decreasing process takes the most time during data recording. Therefore our bunch

[1]The screen shot was taken using the two detector Martin-Puplett interferometer. Due to the inefficient reference detector signal, we used the one detector Michelson interferometer later.

length measurement should be called average bunch length and profile measurement instead. Single bunch length measurement can be achieved by obtaining the spectrum directly, or by using diffraction grating with a detector array to avoid the lengthy scanning process.

4.2 Spectrum

As we noted earlier the radiation spectrum can be obtained from the interferogram by a simple Fourier transformation. Since the data is recorded in equally spaced intervals the Fourier transformation can be calculated with any Discrete Fourier Transformation (DFT) algorithms. We used the built-in FFT function of the Wolfram's Mathematica package, which is based on the FFTW[2] algorithm.

A common problem of DFT algorithms is the picket fence effect, which is related to the finite or relatively small number of recorded data points. The general solution is to add N number of zeros each side of the interferogram. Of course this method does not increase the physical resolution, it only smooths the result of DFT. The N is called the zero filling number and we chose N to be 2 times of the number of recorded data points.

The obtained radiation spectrum is shown on Figure 36. As you can see on the obtained spectrum, the whole low frequency range below 200 GHz is suppressed (compare with Figure 23). Also, a periodic oscillation can be observed through the whole spectrum. The signal above 800 GHz is coming from the detector noise.

[2]For more details see: www.fftw.org.

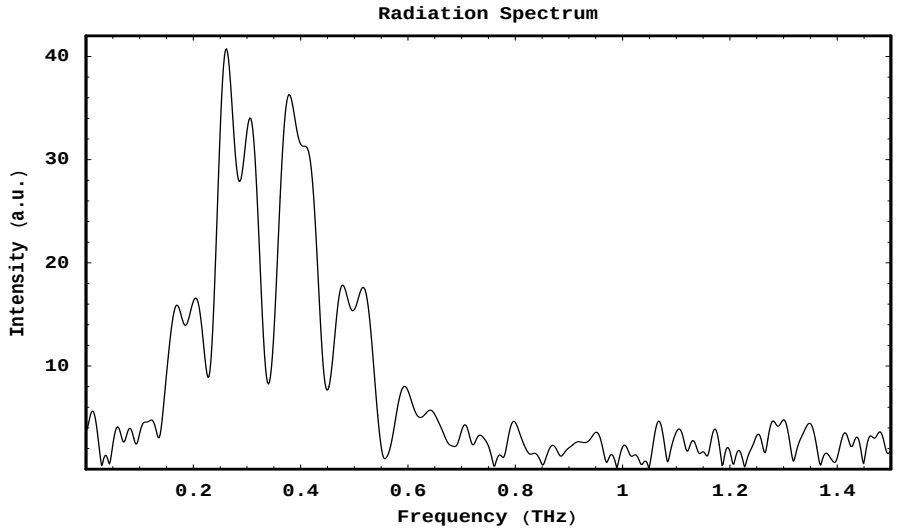

Figure 36: Spectrum of a measured coherent transition radiation.

4.3 Calibration and transfer function

To understand the obtained spectrum in Figure 36. we should investigate our experimental design to find the transfer function of the whole system. That is to calibrate our system in the far-infrared frequency range, specifically from 0.1 THz to 1.5 THz.

In order to measure the frequency response of our system a well know radiation source is needed. For this reason we have built a 1000K blackbody radiator. However, the intensity of the far-infrared radiation of the 1000K blackbody source was too weak to obtain a transfer function.[3] Still we can estimate the transfer function by investigating the possible spectral distortion.

[3]In future our plan is to use a mercury vapor lamp (HPK-125) to provide much higher temperature ($\sim 5000K$) and much higher intensity in the far-infrared radiation range.

4.3.1 Diffraction losses

In the low frequency range the highest proportion of the spectrum distortion is coming from the diffraction losses due to the finite size of optical elements like the three flat mirrors in the periscope, the two parabolic mirrors and the small detector pupil. The low frequency suppression of the system can be estimated by calculating the diffraction losses between the two parabolic mirrors, see Figure 32.

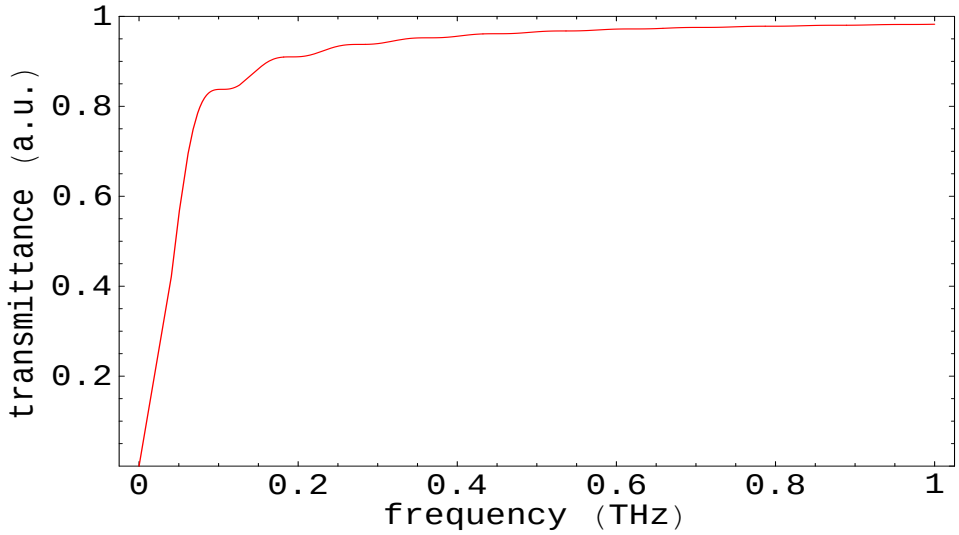

Figure 37: Transmittance function due to diffraction losses. Using $a_s = 5$cm, $a_r = 7.5$cm as apertures and $d = 200$cm as distance between the two optical elements.

The diffraction from the first parabolic mirror causes a decreased intensity of the radiation on the second parabolic mirror's aperture. The fraction of the total radiated energy contained within the effective area of the farest parabolic mirror can be calculated considering Fraunhofer diffraction [57]

$$T_{diff.} \approx 1 - J_0^2(ka_s w) - J_1^2(ka_s w), \tag{93}$$

where J_0 the zeroth and J_1 the first Bessel function of the first kind. The k is the wavenumber, a_s is the aperture of the parabolic mirror close to the source, and $w = \sin a_r/d$, where a_r is the aperture of the other parabolic mirror and d is the distance between the two optical elements. The result of the calculation is shown on Figure 37.

In this calculation we assumed that the radiation source is point-like and located in the focal point of the first parabolic mirror, and the detector pupil is also located in the focal point of the second parabolic mirror. Since the first mirror is very close to the radiator the point-like source assumption is not fulfilled. Also, in our setup the first mirror is further from the radiation source than the focal length by 2.5 cm. These effects can cause even stronger losses than what we estimated. A more detailed explanation of diffraction losses can be found in [58].

4.3.2 Absorption by the vacuum chamber window

The coherent radiation from the electron bunch is generated in vacuum and transferred from the slit chamber through a vacuum window into the interferometer. Therefore some radiation could be absorbed in the material of the vacuum window. The window, that we used in our experiments, is a 5 mm thick fused quartz window. The transmittance of such a vacuum window is shown on Figure 38 along with a more expensive 8.5 mm thick crystalline quartz vacuum viewport in the far-infrared frequency range [59].

As shown on the transmittance graph, the transmission coefficient of the fused

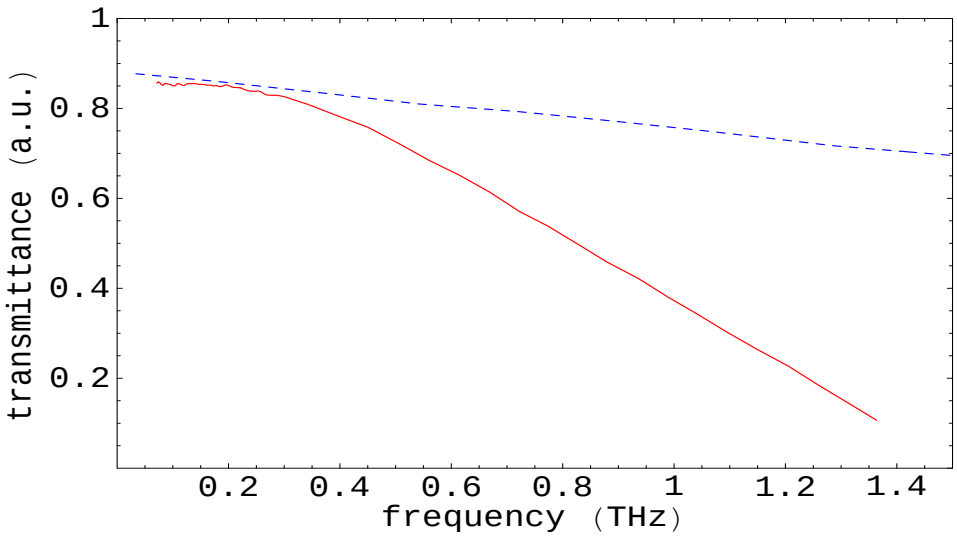

Figure 38: Transmission of quartz made viewports in the FIR frequency range. The solid line shows the transmittance of a 5 mm thick fused quartz vacuum window, while the dotted line shows the transmittance of 8.5 mm thick Crystalline Quartz window.

quartz is constant (T $\approx$ 0.8) below 125 GHz, however in the 0.125 THz-1.5 THz range it is linearly decreasing below T $\approx$ 0.2 transmittance. From the graph we can see that in this frequency range the crystalline quartz window would be a better choice to obtain the coherent radiation spectrum.

4.3.3 Absorption by humid air

The coherent radiation is transferred through vacuum window to the interferometer through normal humid air. The path length in the humid air is around 2 m. Therefore we should take account the radiation absorption due to (mainly) the water vapor. The transmission of humid air under normal conditions in the far-infrared range [28] is shown on Figure 39.

Comparing the transmittance curve above to our coherent spectrum, Figure 36.,

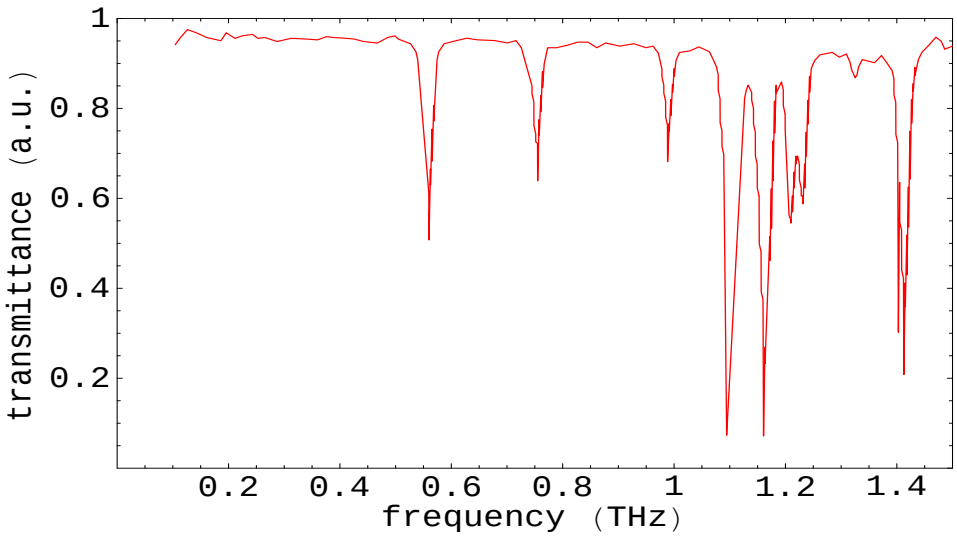

Figure 39: Transmission of humid air for an optical path of 50 cm.

the high radiation loss at 0.55 THz clearly can be seen. However the other high frequency absorption points are less observable due to the small measured intensity and high noise. In the frequency range of our interest (0.1 THz-1.0 THz) the noticeable absorption frequencies are ~ 0.55 THz, ~ 0.75 THz and ~ 1.0 THz.

4.3.4 Transfer function and correction process

In the previous sections we have attempted to quantify each spectral distortion of our experimental setup. We found three important possibilities to take account into the transfer function, namely the absorption of humid air and the absorption in the fused quartz window and finally the diffraction losses due to the finite size of the optical components.

The combined transmission spectrum is obtained as the product of all transmission

functions,

$$T_{com.}(\nu) = \prod_i T_i(\nu) = T_{air}(\nu) T_{window}(\nu) T_{diff.}(\nu) \tag{94}$$

Since the Michelson interferometer has a finite spectral resolution, the combined transmission function has to be convolved with the instrumental line shape (ILS) of the measurement to adjust it to its resolution. We used Fourier transformation of the very common four-term Blackmann-Harris (BH) apodization window to approximate the ILS of the Michelson interferometer,

$$BH(\tau) = a_0 + a_1 \cos\frac{\pi\tau}{\tau_{max}} + a_2 \cos\frac{2\pi\tau}{\tau_{max}} + a_3 \cos\frac{3\pi\tau}{\tau_{max}}, \tag{95}$$

where the BH coefficients of the window are

$$a_0 = 0.358875 \qquad a_1 = 0.48829 \qquad a_2 = 0.14128 \qquad a_3 = 0.01168\,. \tag{96}$$

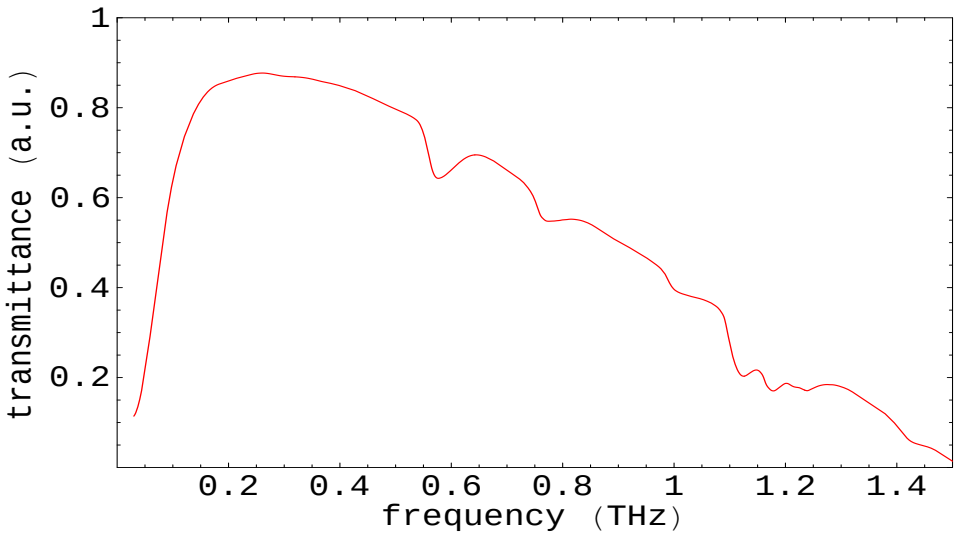

Figure 40: Approximated transfer function of the experiment.

In our case the τ_{max} is 75 ps due to the 45 mm maximum interferogram scan.

This is related to the maximum displacement of the translation stage used in the Michelson interferometer. Therefore the corrected radiation spectrum is obtained as

$$I_{corr}(\nu) = \frac{I_{measured}(\nu)}{T_{\Sigma}(\nu)}, \tag{97}$$

where

$$T_{\Sigma}(\nu) = T_{com.}(\nu) \otimes \tilde{BH}(\nu). \tag{98}$$

The final result, that is, the corrected transmission function is shown on Figure 40.

4.4 Gaussian assumption

4.4.1 Time-domain fitting approach

In the previous section we obtained the transfer function of our experiment, however in some cases we need a very fast method to obtain bunch length. To avoid complex calculations we take account only the low frequency loss and we assume Gaussian bunch profile. In this section we review a method proposed by Murokh et al. to obtain bunch length using time-domain (interferogram) analysis [60].

The low frequency distortion can be approximated by an exponential filter function

$$g(\omega) = 1 - \mathrm{e}^{-\xi^2\omega^2} \tag{99}$$

which removes the low frequency signals with a characteristic frequency cut-off, ξ^{-1}.

We further assume that the autocorrelation of the signal in the frequency domain is a product of a Gaussian spectral beam density (Gaussian form factor), see Equation (86), and the filter function only. So we also assumed that the coherent radiation does

not depend on the single particle spectrum, which is valid for transition radiation only. Thus the spectrum of the measured signal becomes

$$\begin{aligned}\tilde{S}(\omega) \propto |\rho_{Gauss}(\omega)g(\omega)|^2 &= \left|e^{-(\omega\sigma_z/c)^2}(1-\mathrm{e}^{-\xi^2\omega^2})\right|^2 \\ &= e^{-2(\omega\sigma_z/c)^2}\left[1-2e^{-\xi^2\omega^2}+e^{-2\xi^2\omega^2}\right].\end{aligned} \tag{100}$$

The analytical expression of the signal in the time-domain, the Inverse-Fourier transformation of the above expression, is then

$$S(t) \propto \sigma\left[\mathrm{e}^{-\frac{t^2}{4\sigma^2}}+\frac{\sigma}{\sqrt{2\xi^2+\sigma^2}}\,\mathrm{e}^{-\frac{t^2}{4(2\xi^2+\sigma^2)}}-\frac{2\sigma}{\sqrt{\xi^2+\sigma^2}}\,\mathrm{e}^{-\frac{t^2}{4(\xi^2+\sigma^2)}}\right]. \tag{101}$$

The above expression can be used to find the r.m.s. beam pulse length, σ and the cut-off frequency of the experimental setup by a simple two parameter fit (σ,ξ) directly to our measured interferogram.

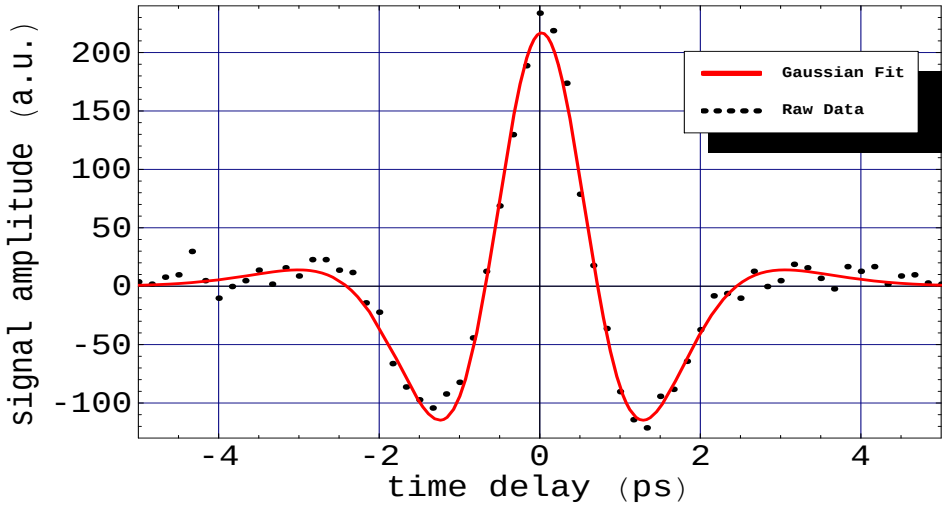

Figure 41: The measured interferogram and the Gaussian assumption fit.

An example of such a fit is shown on Figure 41. The raw data is a coherent transition radiation (slit closed) interferogram. The measured Gaussian r.m.s. beam

size obtained from the fit is $\sigma = 0.44$ ps, which corresponds to 1.03 ps FWHM bunch length. The obtained result is in very good correlation with our expected bunch length estimated by PARMELA simulation.

The cut-off frequency, ξ^{-1}, obtained from the fit is 1.5 THz.

4.4.2 Internal reflections and frequency-domain analysis

In the previous section we obtained an approximated electron bunch size using Gaussian assumption directly from the measured interferogram. It is also possible to use the calculated coherent radiation spectrum to obtain the bunch length by fitting Equation (100) to the measured spectral intensity. The fitting is shown on Figure 42.

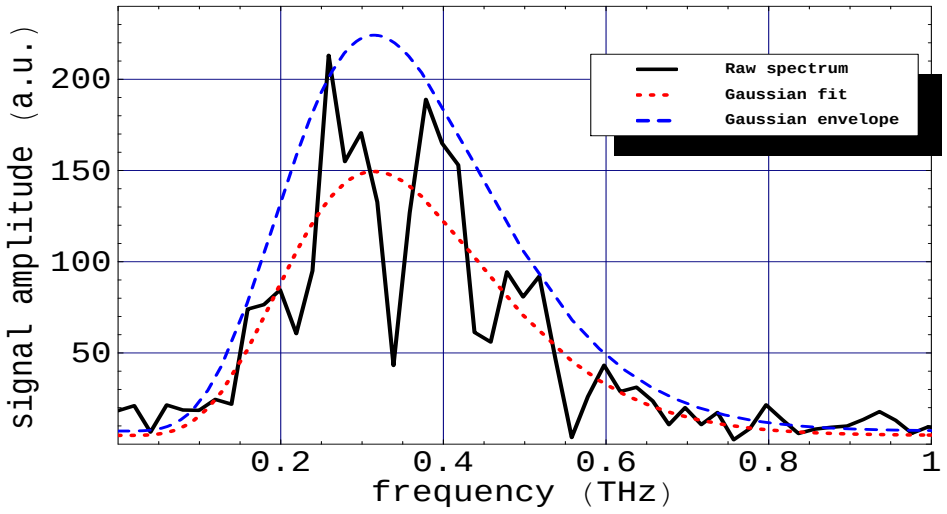

Figure 42: Transition radiation spectrum -solid line- along with Gaussian assumption fit -red doted line- and Gassian envelope -blue dashed line. The envelope is 1.5 times the Gaussian fit, which shows very good agreement with the measured data.

We obtained the same values as in the time-domain fit, however, as it can be seen on the plot, there is a periodic structure inside the Gaussian envelope. This structure is possibly related to interferences. Actually the effect of these interferences is clearly seen also on both sides of the interferogram around 9 ps, see Figure 34. The main peak, at 0 ps position is the result of the autocorrelation of the radiation pulse while the others are signatures of cross-correlations of the radiation pulse and reflected pulses.

These effects are known to be cause by pyroelectric detectors, where inside of the pyroelectric crystal multiple reflections occur at FIR frequencies [41]. However we have used Golay-cell detectors, which suppose to be free of these problems.

To take account the interferences in the fitting process a sinusoidal term should be added to Equation (100) as suggested in [61]. This way we can obtain more information on the reflection process: the period of the spectral response depends on the optical path length, nd,

$$|E_r(\omega)|^2 \propto \sin^2 \frac{\omega n_r d}{c}, \tag{102}$$

where n_r is the index of refraction of the material where the process is occurred, d is the thickness of the material and c is the speed of light. Therefore our estimated spectrum function becomes

$$\tilde{S}(\omega) \propto e^{-2(\omega\sigma_z/c)^2} \left[1 - 2e^{-\xi^2\omega^2} + e^{-2\xi^2\omega^2}\right] \sin^2 \frac{\omega n_r d}{c} \tag{103}$$

The fitting result is shown on Figure 43. We obtained a much better fit to the measured spectral response. The process gives the Gaussian beam size of $\sigma = 0.44$

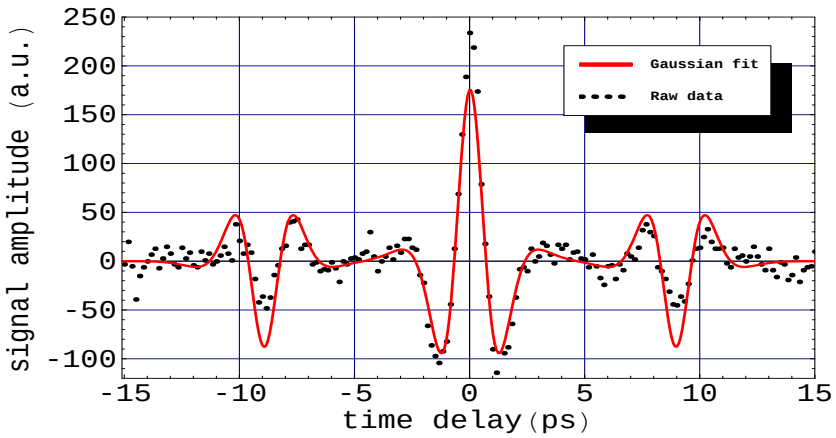

(a)

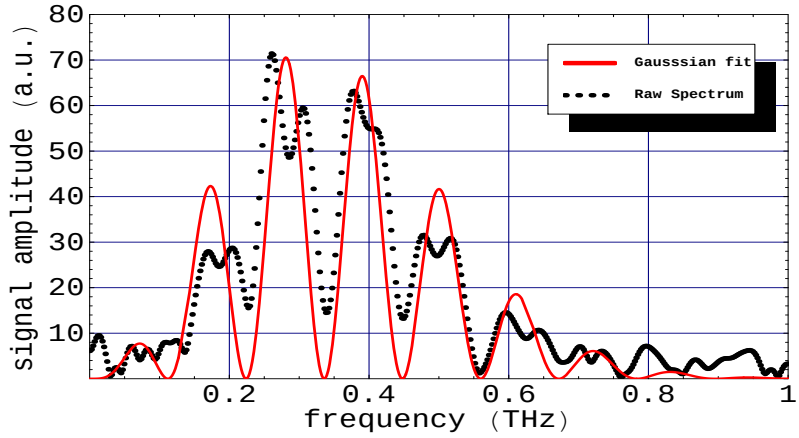

(b)

Figure 43: Coherent radiation interferogram and spectrum fit assuming Gaussian form factor and internal reflection.

ps and filter parameter of $\xi = 0.64$ ps, same values as before. So this effect does not interact with our bunch length measurement using Gaussian assumption. The optical pathlength obtained from the fit is $n_r d = 1.34$ mm, which can be used to find the source of this effect.

The source of interference is still unknown. One of the possible candidates was the quartz vacuum window, however due to the thickness of this window (3mm) and

the measured optical pathlength (1.34mm) this is not possible, in case the index of reflections of the crystal would be less than 1. Also, multiple reflections in the diamond window of the Golay could be another source, but we observed the same effect using a pyro-electric (Molectron P4-45) sensor as well (along with the reflections caused by the 130μm thick $LiTaO_3$ crystal).

Another source of this interference effect could be the silicon wafer that we used for radiation screen. If the layer of gold coating on the wafer is less then what we expect, some TR radiation pulses can be created on the inner side of the silicon wafer. They produce an interference with the original radiation pulse generated on the outer side of the radiator [62]. The thickness of the silicon wafer is 500μm, using the obtained pathlength the index of refraction of the silicon is verifiable. By this calculation the index of reflection of the silicon wafer is 2.68 in FIR frequency range, which is close to the expected 3.36 [63]. However this process is questionable due to the gold-coating on the silicon wafer. To test the above statement one should use very thin and rigid material as transition (and diffraction) radiation screen instead of the thick silicon wafer.

As we pointed out, the bunch length measurement using the Gaussian assumption is not sensitive to this effect. In the following we will use the original method to obtain electron bunch lengths from the coherent radiation. However further investigation is needed to find the source of the interference fingers and to avoid it, by example using different materials.

4.4.3 Coherent diffraction radiation and Gaussian beam profile

As we noted, the previously used fitting method assumes constant single particle radiation spectrum. To use this method on coherent diffraction radiation we have to include the singe diffraction radiation dependence in Equation (100) as it was described in Section 2.5.1. Therefore the measured spectrum of the coherent diffraction radiation becomes

$$\tilde{S}_{measured}(\omega) \propto |g(\omega) \cdot \rho_G(\omega)|^2 \, I_s(\omega), \tag{104}$$

where $I_s^{DR}(\omega)$ is the single particle diffraction radiation intensity, $\rho_G(\omega)$ is the assumed Gaussian form-factor and $g(\omega)$ is the filter function, Equation (99).

The radiation spectrum of DR created by a single particle has a complicated form, as described earlier, see Equation (47-49). The main contribution of the frequency dependence is coming from the exponential part in (47). Thus a simplified frequency dependence of DR from a slit can be written as

$$I_s(\omega) \propto \int_{X_{min}}^{X_{max}} \mathrm{e}^{-\frac{a\omega}{c\gamma}\sqrt{1+X^2}} \mathrm{d}X, \tag{105}$$

where a is the slit width, X is the horizontal observation angle (in units of γ), c is the speed of light and γ is the Lorentz factor of the electron beam.

The measured interferograms and calculated spectrums for different slit positions are shown on Figure 44. We used three different slit width positions, while the beam energy was set to 28 MeV, a : 0 mm (transition radiation), 1.25 mm, 1.88 mm and 2.5 mm. To compare the shape of the obtained data we also plotted the transition radiation interferogram and spectrum on the same graph. The effect of the slit width on the interferogram is clearly seen: the intensity decreases and the mean

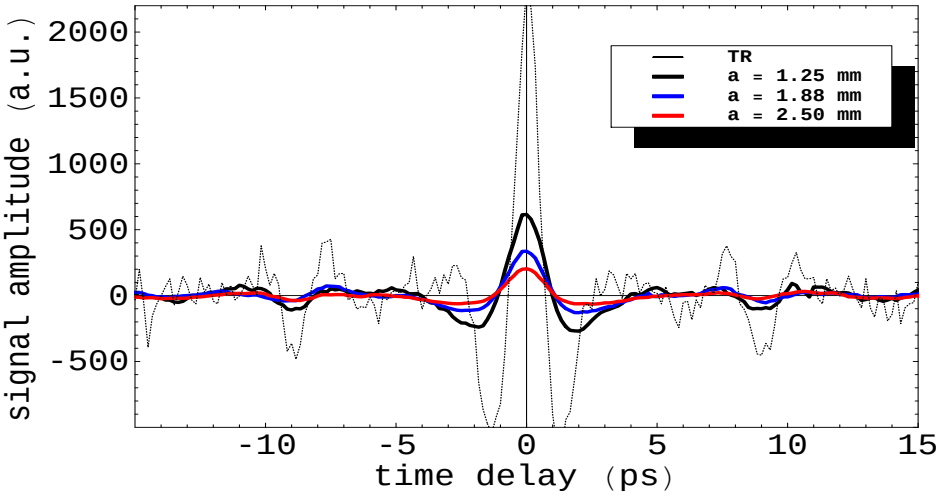

(a)

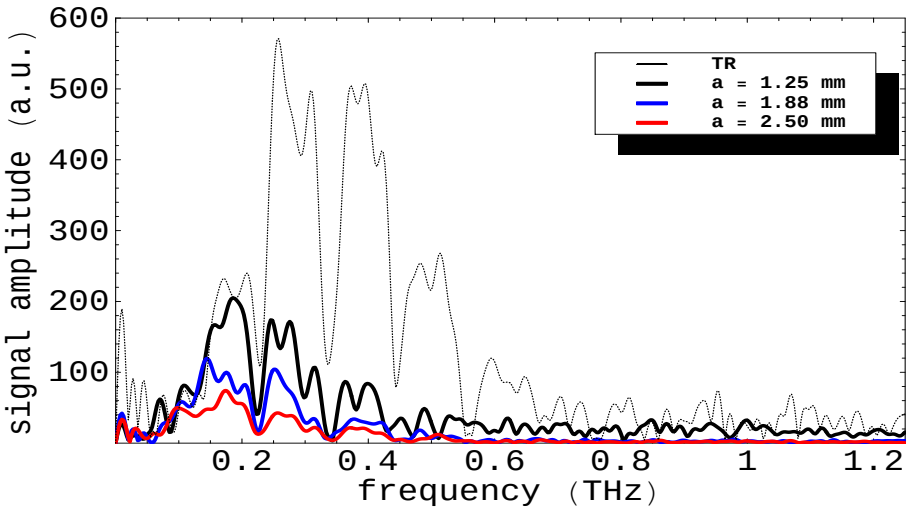

(b)

Figure 44: Coherent diffraction radiation interferogram (a) and spectrum (b) at various slit width positions created by 33 MeV electron bunch.

peak becomes wider as the slit opens.

The spectrum of the diffraction radiation from a slit behaves as we expected: the high frequency radiation part is cut of with increasing slit width.

The bunch length can be determined by fitting the measured coherent diffraction radiation spectrum using Equation (104). In our experiment we used three different slit width positions and we determined the longitudinal bunch length for each position. We showed the Gaussian r.m.s size σ_{DR} and also the more convenient FWHM bunch length, $l_{FWHM} = 2\sqrt{2\ln 2}\cdot\sigma_{DR}$. The summarized results are shown in Table 2, where the slit width $a = 0mm$ indicates the result obtained for coherent transition radiation. We calculated the Gaussian r.m.s. sizes without the $I_s^{DR}(\omega)$ dependence as well, σ_{TR}, that is assuming coherent transition radiation, to see the importance of the single particle radiation spectrum of diffraction radiation in our fitting process.

Table 2: Measured beam sizes assuming Gaussian beam distribution and simple low frequency filter function. The σ_{TR} is the r.m.s. beam size assuming constant single particle spectral distribution, while σ_{DR} is the real measured beam r.m.s. size.

Measured e$^-$ bunch lengths using coherent TR and DR radiation assuming Gaussian beam profile

Slit width	Gaussian r.m.s. length		Measured bunch length	Filter parameter
(mm)	σ_{TR} (ps)	σ_{DR} (ps)	FWHM (ps)	ξ (ps)
0.00	0.44±0.03	0.44 ±0.03	1.04 ±0.07	0.65±0.06
1.25	0.51±0.02	0.45 ±0.02	1.06 ±0.05	1.37±0.07
1.88	0.57±0.02	0.49 ±0.02	1.18 ±0.05	1.58±0.06
2.50	0.56±0.02	0.44 ±0.02	1.04 ±0.05	1.85±0.07

The result of measuring Gaussian longitudinal bunch sizes shows high agreement

with the PARMELA simulation, a 1 ps FWHM longitudinal bunch length. We were able to obtain almost the same size in each slit position. Our measured average beam size is 1.08 ± 0.05 ps. Our results are indicating, that the diffraction radiation is suitable to use as a non-intercepting bunch size measurement technique. As it can be seen on Table 2, disregarding the effects of the single particle diffraction radiation spectrum would yield higher Gaussian r.m.s sizes.[4]

One interesting observation is the increasing filter parameter, ξ, or what it means, the increasing low frequency contribution. The cut-off parameter dependence on slit width is in qualitative agreement with theoretical calculation, using diffraction losses and far-field approximation, predicting continuous shift toward lower frequencies as the slit width increases [64].

4.5 Bunch profile reconstruction process

In this section we detail the process of electron bunch profile reconstruction from coherent spectrum. In this process we used the coherent spectrum from transition radiation, since it provides broader spectrum, thus more information in the high frequency range, see Figure 44b.

4.5.1 Corrected spectrum

The first step in the reconstruction process is to obtain the corrected coherent spectrum using the calculated transfer function. The method to obtain the transfer

[4]The errors in Table 2 are coming from the fitting process.

function was detailed in Section 4.3.4. The transfer function of our experiment, $T_\Sigma(f)$, including the internal interference effect (described in Section 4.4.2) are shown on Figure 45.

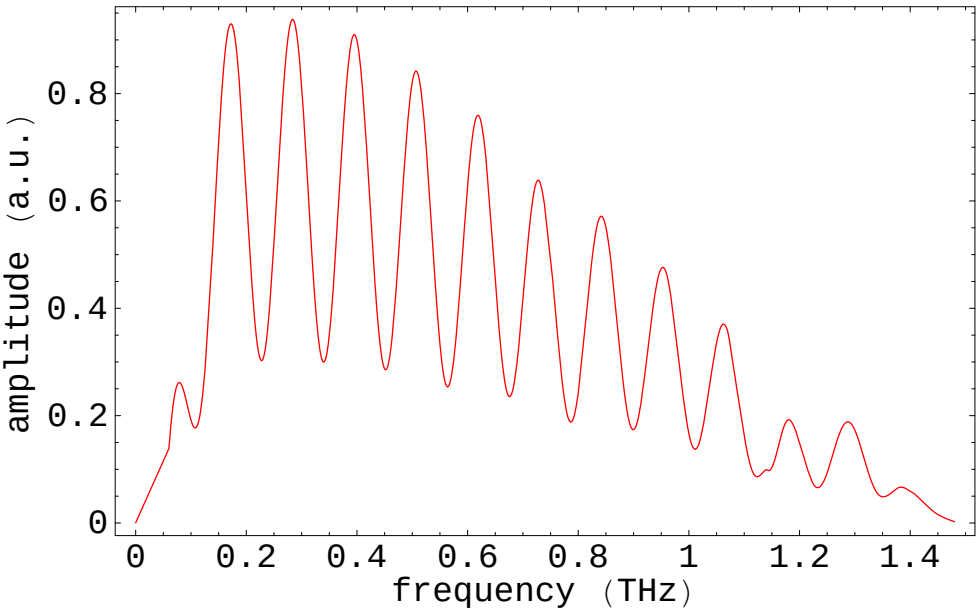

Figure 45: Corrected transfer function with internal interference effect.

The corrected coherent spectrum is then calculated using

$$S_{corr}(f) = \frac{S_{measured}(f)}{T_\Sigma(f)}. \tag{106}$$

Note that, at some region the correction process will fail, like in range above 1 THz or at very low frequencies. Therefore we excluded these points from the corrected spectrum.

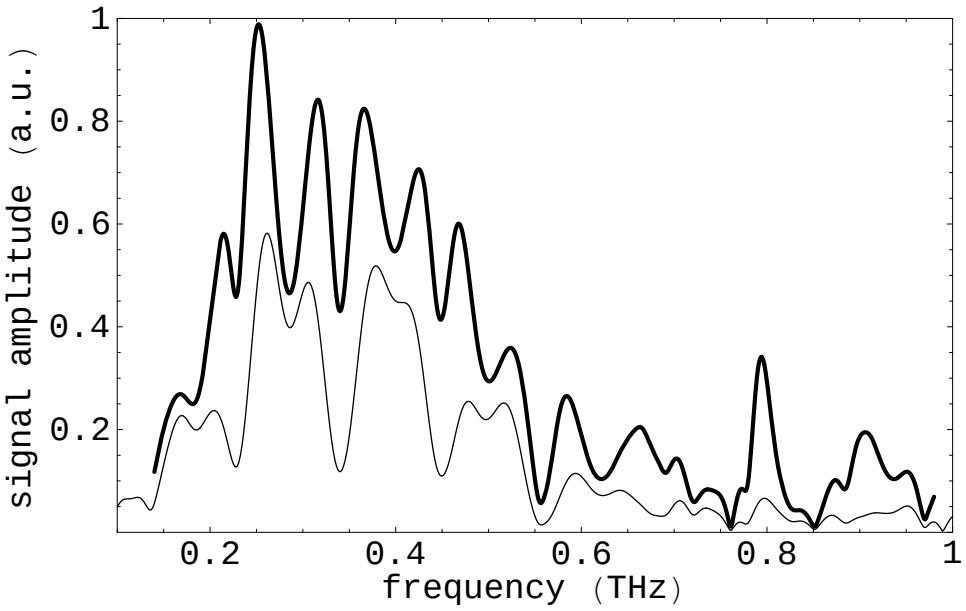

Figure 46: The original measured - thin line - and the corrected - thick line -coherent transition radiation spectrum.

4.5.2 Form Factor

As we showed earlier, the bunch profile is the Fourier transformation of the form factor. The form factor, $f(\omega)$ can be obtained from the coherent spectrum using

$$|f(\omega)| \propto \sqrt{\frac{I_{coh.}(\omega)}{I_s(\omega)}}, \tag{107}$$

process.

The coherent spectrum was measured using transition radiation, therefore the single particle radiation is frequency independent. The form factor is then the normalized corrected spectrum. However, a few more corrections must be added to the form factor to obtain reasonable bunch profile.

At low frequencies, $f < 250$ GHz, the spectrum is strongly suppressed, any beam profile information is lost there. To obtain reasonable form function we must correct

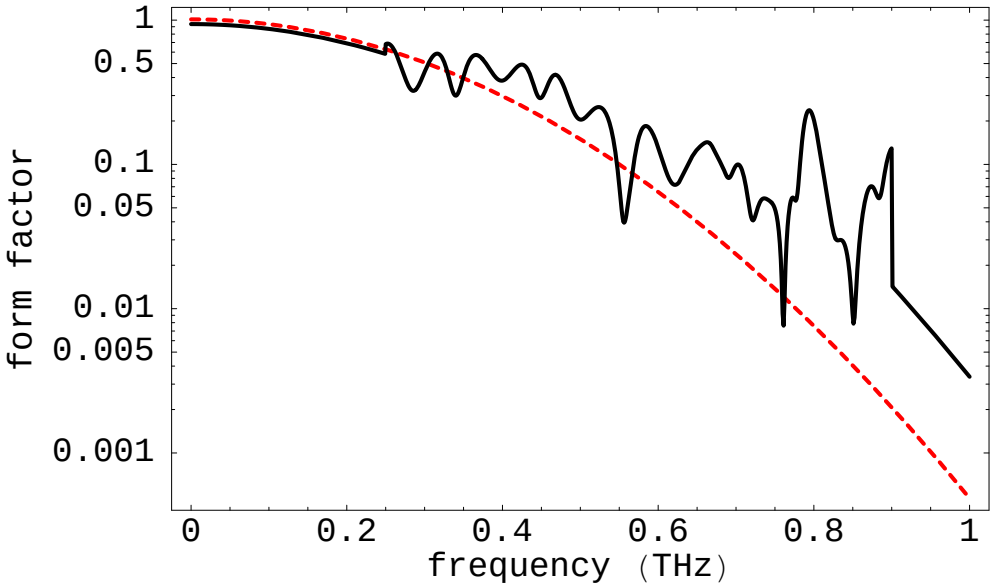

Figure 47: Corrected form factor with low frequency $f < 0.23$ THz and high frequency $f > 1.0$ THz Gaussian extrapolation - solid black line - and the Gaussian donor - dashed red line.

the spectrum using assumptions. The most obvious solution is to use the Gaussian extrapolation.

At frequencies higher than $f > 1.0$ THz, the measured spectrum is mostly detector noise. To avoid including this noise to the form factor we used again Gaussian extrapolation for this frequency range.

We used the same Gaussian function, what we obtain during the fitting method, as the donor in the extrapolation The corrected form factor is shown on Figure 47, along with the extrapolation "donor".

4.5.3 Minimal Phase

The next step to obtain the bunch profile is to calculate the minimal phase. The phase is needed to the final Fourier transformation of the form factor to determine the longitudinal bunch profile. During the measurement the phase information is lost, but using the so called Kramers-Kronig method, it can be reconstructed. That is to compute

$$\Psi(\omega) = -\frac{2\omega}{\pi} \int_0^\infty \mathrm{d}x \frac{\ln |f(x)/f(\omega)|}{x^2 - \omega^2}. \tag{108}$$

We used numerical integration to calculate the phase over frequency range of 0 - 1.5 THz. The obtained Kramers-Kronig minimal phase is plotted on Figure 48.

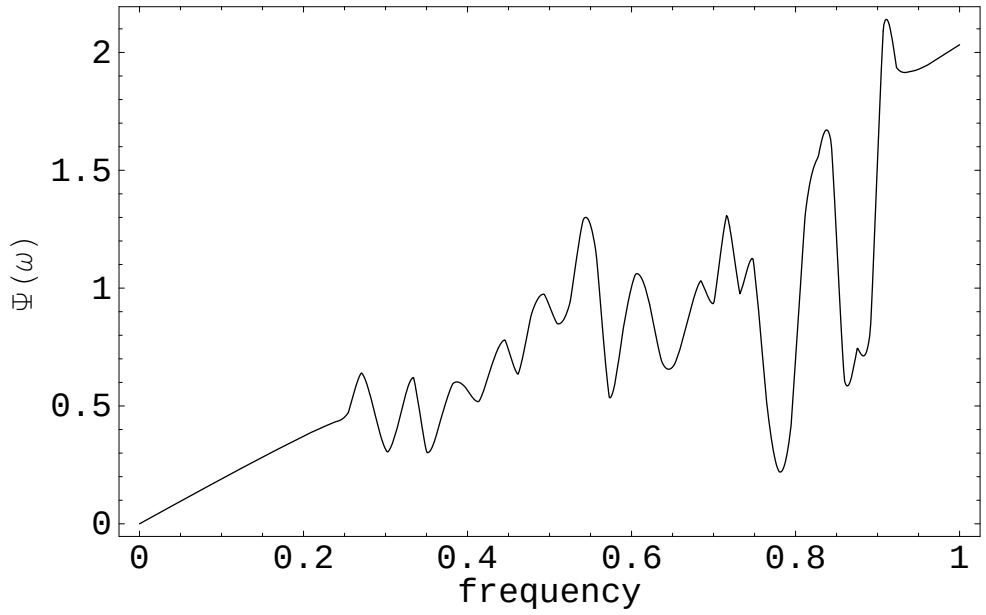

Figure 48: The minimal phase calculated by Kramers-Kronig analysis.

4.5.4 Bunch shape

The final step to calculate the longitudinal bunch profile is to Fourier transform the form factor using the minimal phase that is to obtain

$$\rho(t) = \frac{1}{\pi c} \int_0^\infty \mathrm{d}\omega f(\omega) \cos\left[\Psi(\omega) - \omega t\right]. \tag{109}$$

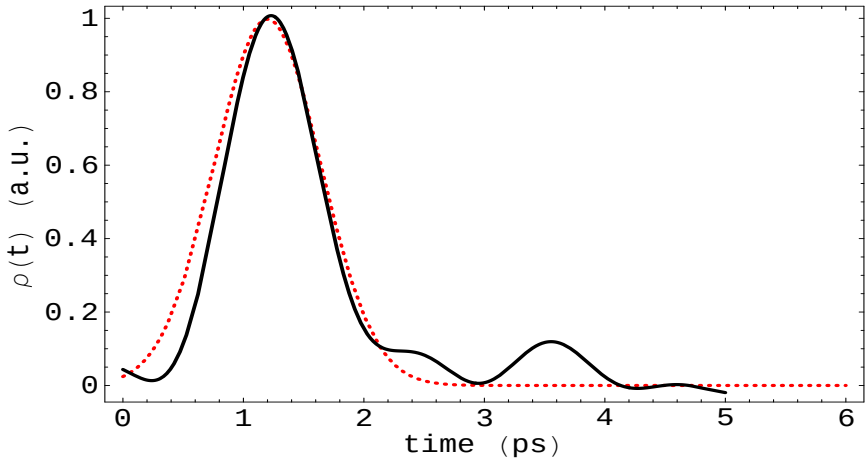

Figure 49: Bunch shape reconstructed from the extrapolated form factor -solid black line-, and the Gaussian bunch obtained from fitting process, $\sigma = 0.44$ps.

The constructed longitudinal bunch profile is shown on Figure 49 along with the Gaussian bunch profile obtained from the fitting process. The result is a reasonable 1 ps FWHM long Gaussian like bunch with 2 small tail bunches.

We would like to emphasize that the reconstruction process has many uncertainties due to the spectrum corrections, the extrapolation processes, etc. However the existence of satellite beam is absolutely reasonable. The location of the second bunch, due to the obscurities of Krames-Kronig method, as we showed earlier, is indefinite.

CHAPTER V

MEASUREMENT OF THE ANGULAR DISTRIBUTION

Our secondary plan was to measure the angular distribution of the coherent diffraction radiation. The experimental set-up was detailed in Section 3.6. We used an XY-movable stage to obtain the angular distribution. This process is very lengthy, it takes around 40 minutes to complete one 2D scan. We should note that, during this time, small change may occur in the quality of the electron beam.

For the measurement we used 1.25 mm slit width, at 30 MeV beam energy. We have measured the vertically polarized component of the angular distribution (AD) using a wire grid polarizer. As we showed earlier only the vertically polarized component contains information about the transverse beam size.

5.1 Measurement of the vertically polarized component of the angular distribution

The measured vertically polarized AD is shown on Figure 51a. The ideal angular distribution from a slit would be symmetric, see Figure 17. The obtained AD is asymmetric, which could be caused by the DR target deformations. That is the two plates of the slit is shifted or inclined to each other, see Figure 50.

The discussions of these kind of deformations is explained in details in [42]. After taking account of these effects in the angular distribution of the DR via simulations we found a very good match to our measured data, see Figure 51b. The inclination

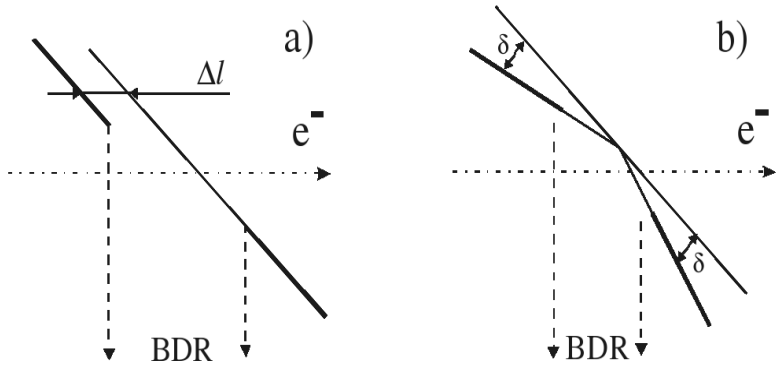

Figure 50: Two types of possible slit target deformations [42].

angle in simulation plot are $\delta_{horz.} = 0.004$ and $\delta_{vert.} = 0.025$ radians. They are very small. The shift between the two plates of the slit in the simulation plot is also small, $\Delta l = 100\mu$m.

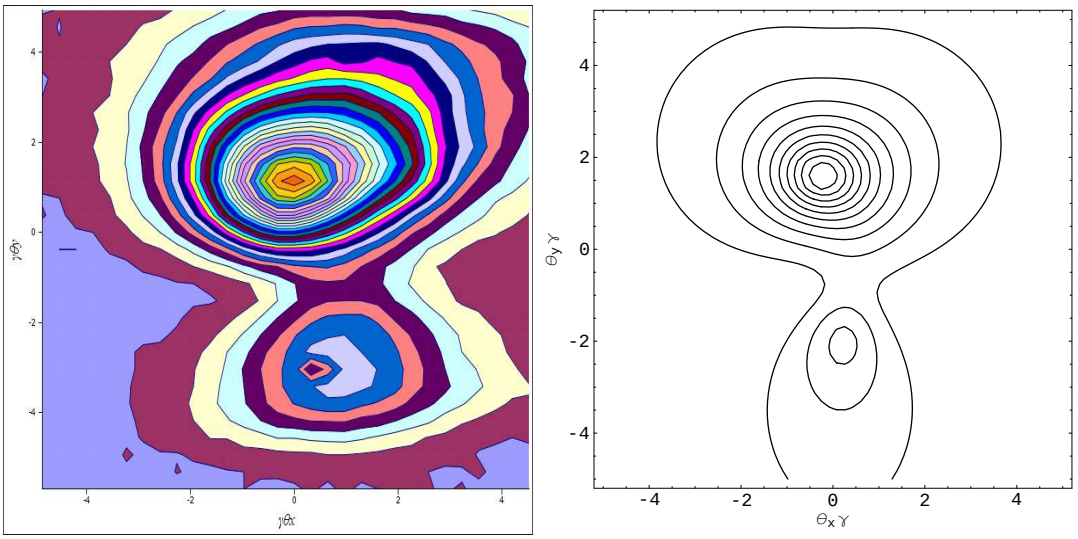

(a) Measured distribution.

(b) Simulated distribution.

Figure 51: The vertically polarized component of the angular distribution of DR, slit width 1.25 mm, 30 MeV beam.

To verify these slit deformations obtained from the simulated AD, we tried to measure these parameters using our slit assembly. We were able to confirm that these deformations are valid. Also during these tests we saw other deformations like bending and uneven edges of the silicon wafers. In a future work one should modify these plates to decrease these effects.

5.1.1 Transverse beam size measurement

In this section we show an attempt to obtain transverse beam size from the angular distribution of DR from a slit. Although we showed earlier these measurements may be not providing good results due to coupling between the transverse beam size and the divergence, see Section 2.3.3.

To obtain the vertical beam size we used the method described in Section 2.3.1. That is to analyze the vertical part ($\gamma\theta_Y$ at $\gamma\theta_X = 0$) of the vertically polarized AD, the vertical scan part of Figure 51, where the intensity reaches its maximum.

We used fitting method to obtain the vertical beam size. The fitting function is very complicated to be included here, it contains the distortions from the inclined and shifted slit target and all the parameters of the diffraction radiation angular distribution, see Equation 56 for more detail. Figure 51 shows the measured angular distribution along with our fit, to obtain the transverse beam size.

The obtained vertical transverse beam size from the fit is $\delta_y = 810\mu$m, which is reasonable, but further analysis and experiments are needed to show the validity of this method. The transverse beam size can be changed during the FEL operation by

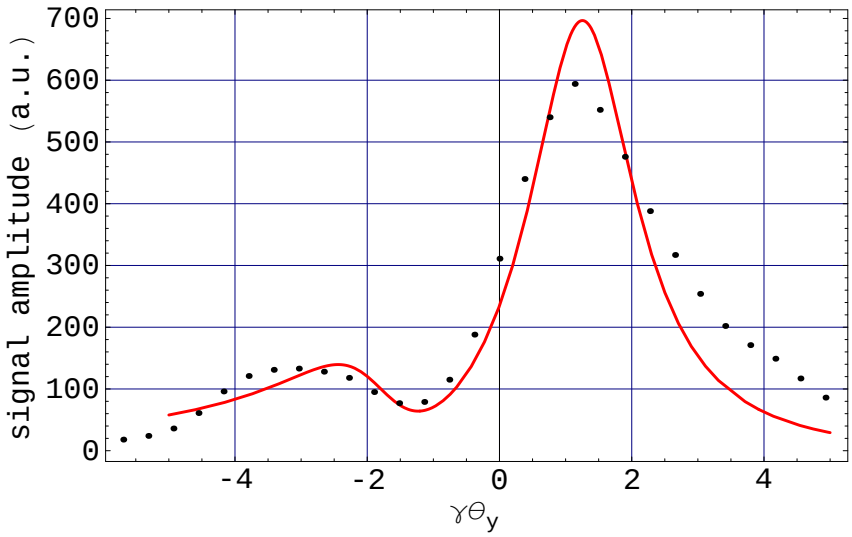

Figure 52: The measured $\gamma\theta_Y$ component of the vertically polarized AD at $\gamma\theta_X = 0$ - dots- and the AD fit - solid line.

(de)focusing the beam, so the above method can be tested with various beam sizes . However at this time this method is unusable with its 40 minutes scans. Other methods are much quicker. A solution would be to adopt a detector array or a FIR CCD camera to measure the angular distribution much faster.

At the end of this chapter I would like to emphasize that this angular distribution measurement is not the main part of this work. Our plan was to show how the bunch length can be measured using coherent diffraction radiation and coherent transition radiation.

CHAPTER VI

CONCLUSION AND FUTURE WORK

In this thesis we presented our work on developing new beam monitoring methods for linear accelerators and for free-electron lasers. We concentrated on the coherent diffraction radiation based beam monitoring technique and compare it with the well-known transition radiation method. We developed a movable slit to generate and to investigate the properties of diffraction radiation generated from various radiator configurations.

We measured the electron bunch profile of the W. M. Keck FEL using coherent radiation. We performed bunch length measurements using coherent diffraction and transition radiation. The results were in good agreement with PARMELA simulations and observations of the quality of the FEL IR output. We showed that the diffraction radiation generated from a slit can be used as a non-intercepting bunch length monitor. These measurements are a good basis of the upcoming development of a single shot electro-optic bunch length monitoring system at the Vanderbilt FEL.

We measured the angular distribution of single slit diffraction radiation. We identified a few sources of angular distortions, like slit shifting and bending. We showed an example of the measurement of transverse beam size, although this measurement is not complete without addition divergence measurements. These experiments are the initial steps to the diffraction radiation interferometry to obtain real transverse

beam sizes and beam divergence.

Hopefully this thesis work is a beginning of experiment series at the Vanderbilt University to develop new beam size monitoring techniques. The next step on this way would be to use two slit configurations to measure beam divergence and transverse sizes using diffraction radiation interferometry.

The electro-optic longitudinal bunch profile and length measurements would provide a good comparison with our measured data and could be used to develop more efficient methods for these kind of experiments.

REFERENCES

[1] "LHC Design Report," tech. rep., CERN, 2004. CERN Report No. CERN-2004-003.

[2] "International Linear Collider - Technical Review Report," tech. rep., 2003.

[3] B. Feng and et al., "Non-intercepting electron beam diagnostics using diffraction radiation." UCLC Proposals, 2003.

[4] B. Gabella and et al., "Single-shot electro-optic measurement of a picosecond electron bunch length." UCLC Proposals, 2003.

[5] F. Amirmadhi, C. A. Brau, M. Mendenhall, J. R. Engholm, and U. Happek, "Electron bunch length measurements at the Vanderbilt FEL," *Nucl. Inst. and Meth. A*, vol. 375, p. 95, 1995.

[6] U. Happek, A. J. Sievers, and E. B. Blum, "Observation of coherent transition radiation," *Phys. Rev. Lett.*, vol. 67, p. 2962, 1991.

[7] D. Mihalcea, C. Bohn, U. Happek, and P. Piot, "Longitudinal electron bunch diagnostics using coherent transition radiation," in *in Proceedings of 2005 Particle Accelerator Conference*, 2005.

[8] B. Bouchet, "In proceedings of the 1991 IEEE particle acc. conf.," in *8th Advanced Accelerator Concepts Workshop, 1998*, p. 1186, 1991.

[9] M. Ross and E. S. McRory (Ed.), "In proceedings of the workshop on accel. inst. 2," in *8th Advanced Accelerator Concepts Workshop, 1998*, no. 229 in AIP Conference Proceedings, p. 88, AIP, New York,, 1995.

[10] V. I. Telnov, "Is a laser wire a non-invasive method," *Nucl. Inst. and Meth. A*, vol. 513, pp. 647–650, 2003.

[11] T. Shintake, "Proposal of a nanometer beam size monitor for e+e- linear colliders," *Nucl. Inst. and Meth. A*, vol. 311, pp. 453–464, 1992.

[12] T. Shintake and K. Oide et al., "Experiments of nanometer spot size monitor at Fftb using laser interferometry." citeseer.ist.psu.edu/257324.html.

[13] M. Ferianis, "Optical Techniques in beam diagnostics," in *in Proceedings of the 1998 EPAC*, (Stockholm), p. 159, June 1998.

[14] M. Katoh and T. Mitsuhashi, "Measurement of beam size at the photon factory with the sr interferometer," in *In: Proc. of the 1999 Particle Accelerator Conference, 1999*, vol. 4, pp. 2307–9, IEEE, NJ, USA,, 1999.

[15] M. Ross, S. Anderson, and J. Frisch, et al., "A very high resolution optical transition radiation beam profile monitor," in *in Proceedings of* 10^{th} *Beam Intr. Workshop, SLAC-PUB-9280*, 2002.

[16] M. Castellano, "A new non-intercepting beam size diagnostics using diffraction radiation from a slit," *Nucl. Inst. and Meth. A*, vol. 394, pp. 275–280, 1997.

[17] R. B. Fiorito and D. W. Rule, "Diffraction radiation diagnostics for moderate to high energy charged particle beams," *Nucl. Inst. and Meth. B*, vol. 173, p. 67, 2001.

[18] Y. N. Dnestrovsky and D. P. Kostomarov *Doklady Akad. Nauk. SSSR*, vol. 124, p. 1026, 1959.

[19] P. Karataev, S. Araki, R. Hamatsu, H. Hayano, T. Hirose, T. Muto, G. Naumenko, A. Potylitsyn, and J. Urakawa, "Status of optical diffraction radiation experiment at KEK-ATF extraction line," *Nucl. Inst. and Meth. B*, vol. 201, pp. 140–152, 2003.

[20] B. Feng, M. Oyamada, F. Hinode, S. Sato, Y. Kondo, Y. Shibata, and M. Ikezawa, "Electron bunch shape measurement using coherent diffraction radiation," *Nucl. Inst. and Meth. A*, vol. 475, pp. 492–497, 2001.

[21] A. H. Lumpkin, N. S. Sereno, and D. W. Rule, "First measurements of subpicosecond electron beam structure by autocorrelation of coherent diffraction radiation," *Nucl. Inst. and Meth. A*, vol. 475, pp. 470–475, 2001.

[22] "Wikipedia." http://en.wikipedia.org.

[23] K. Honkavaara, P. Piot, S. Schreiber, and D. Sertore, "Bunch length measurements at ttf with a streak camera," DESY-TESLA-2000-38.

[24] J. Bahr, D. Lipka, and H. Ludecke, "Optical transmission line for streak camera measurements at PITZ," Prepared for 6th European Workshop on Beam Diagnostic and Instrumentation for Particle Accelerators (DIPAC 2003), Mainz, Germany, 5-7 May 2003.

[25] G. Hairapetian *et al.*, "Streak camera measurements of electron bunch length from a copper photocathode in an RF gun," Prepared for 1993 IEEE Particle Accelerator Conference (PAC 93), Washington, DC, 17-20 May 1993.

[26] R. Lai and A. Sievers, "On using the coherent far ir radiation produced by a charged-partice bunch to determine its shape: I Analysis," *Nucl. Inst. and Meth. A*, vol. 397, pp. 221–231, 1997.

[27] J. B. Rosenzweig, G. Travish, and A. Tremaine, "Coherent transition radiation diagnosis of electron beam microbunching," *Nucl. Inst. and Meth. A*, vol. 365, pp. 255–259, 1995.

[28] L. Fröhlich, "Bunch Lenght Measurements Using a Martin-Pupplet Interferometer at the VUV-FEL," Master's thesis, Department of Physics of the University of Hamburg, June 2005.

[29] R. Lai, U. Happek, and A. J. Sievers, "Measurement of the longitudinal asymmetry of the charged particle bunch from the coherent syncrotron or trasition radiation spectrum," *Phys. Rev. E*, vol. 50, p. R4294, 1994.

[30] G. Schneider, R. Lai, A. Sievers, and W. Walecki, "On using the coherent far ir radiation produced by a charged-partice bunch to determine its shape: II Measurement with syncrotron and transition radiation," *Nucl. Inst. and Meth. A*, vol. 396, pp. 283–292, 1997.

[31] H. L. Andrews and C. A. Brau, "Gain of a Smith-Purcell free-electron laser," *Phys. Rev, ST*, vol. 7, p. 070701, 2004.

[32] G. Kube, H. Backe, H. Euteneuer, and A. Grendel, et al., "Observation of optical Smith-Purcell radiation at an electron beam energy of 855 MeV," *Phys. Rev. E.*, vol. 65, p. 056501, 2002.

[33] A. Doria, G. P. Gallermo, E. Giovenale, G. Messina, G. Doucas, F. K. M, H. Andrews, and J. H. Brownell, "Can coherent Smith-Purcell radiation be used to determine the shape of an electron bunch?," *Nucl. Inst. and Meth. A*, vol. 483, pp. 263–267, 2002.

[34] X. Yan and A.M. MacLeod et al., "Application of electro-optic sampling in FEL diagnostics," *Nucl. Inst. and Meth. A*, vol. 475, pp. 504–508, 2001.

[35] V. Ginsburg and I. Frank, "Radiation of a uniformly moving electron due to its transition from one medium to another," *Journal of Physics*, vol. 9, p. 353, 1945.

[36] J. D. Jackson, *Classical Electrodynamics*. No. 21 November 2006, Wiley-Intersience, New York, third ed., 1998.

[37] M. L. Ter-Mikaelian, *High Energy Electromagnetic Processes in Condesed Media*. Wiley-Intersience, New York, 1972.

[38] C. A. Brau, *Modern Problems in Classical Electrodynamics*. Oxford University Press, 2004.

[39] L. D. Landau and E. M. Lifshitz, *Electrodynamics of Continuous Media*. Pergamon Press, Oxford, 2nd ed., 1984.

[40] A. Potylitsyn, "Transition radiation and diffraction radiation. similarities and differences," *Nucl. Inst. and Meth. B*, vol. 145, pp. 169–179, 1998.

[41] C. Settakorn, *Generation and Use of Coherent Transition Radiation from Short Electron Bunches*. PhD thesis, SLAC Stanford University, 2001.

[42] P. V. Karataev, *Investigation of Optical Diffraction Radiation for Non-Invasive Low-Emittance Beam Diagnostics*. PhD thesis, Tokyo Metropolitan University, 2004.

[43] V. A. Verzilov *Physics Letters A*, vol. 273, p. 135, 2000.

[44] M. Castellano, V. A. Verzilov, and L. Catani et al. *Phys. Rev. E*, vol. 67, p. 015501, 2003.

[45] B. M. Bolotovskii and G. V. Voskresenskii *Sov. Phys. Usp.*, vol. 9, p. 73, 1966.

[46] A. Kazantsev and G. Surdotovich *Doklady Akad. Nauk. SSSR*, vol. 7, p. 990, 1963.

[47] P. Karataev, S. Araki, R. Hamatsu, H. Hayano, T. Hirose, T. Muto, G. Naumenko, A. Potylitsyn, and J. Urakawa, "Grating optical diffraction radiation - Promising technique for non-invasive beam diagnostics," *Nucl. Inst. and Meth. B*, vol. 201, pp. 201–211, 2003.

[48] A. Potylitsyn, "Linear polarization of diffraction radiation from slit and beam size determination," *Nucl. Inst. and Meth. B*, vol. 201, pp. 161–171, 2003.

[49] L. Wartski et al. *J. Appl. Phys.*, vol. 46, p. 3644, 1975.

[50] R. B. Fiorito and D. W. Rule, "OTR beam emittance diagnostics," in *Conference Proceedings No. 319 Beam. Inst. Workshop* (R. E. Shafer, ed.), p. 21, AIP, 1994.

[51] J. L. A. Chilla and O. Martinez, "Analysis of a method of phase measurement of ultrashort pulses in the frequency domain," *IEEE Journal of Quantum Electronics*, vol. 27, no. 5, pp. 1228–1235, 1991.

[52] D. J. Kane and R. Trebino, "Characterization of arbitary femtosecond pulses using frequency-resolved optical gating," *IEEE Journal of Quantum Electronics*, vol. 29, no. 2, pp. 571–579, 1993.

[53] B. Gabella, "FEL gun primer." Personal communication, 2006.

[54] W. B. Tiffany, *The Amazing Versatile Pyroelectric, A Coherent Application Note*. Coherent Inc.

[55] QMC Ltd, *Golay Detector Operating Manual*, 2005.

[56] Molectron Inc., *P4-30/P4-40 Datasheets*, 2005.

[57] M. Born and E. Wolf, *Principles of Optics*. Cambridge University Press, 1999.

[58] M. Castellano, A. Cianchi, V. A. Verzilov, and G. Orlandi, "Effects of diffraction and target finite size on coherent transition radiation spectra in bunch length measurements," *Nucl. Instrum. Meth.*, vol. A435, pp. 297–307, 1999.

[59] A. Eberhagen and H. U. Fahrbach, "Transmittion of neutron and γ-irradiated fused quartz, crystalline quartz, teflon, polyethelen and TPX at mm- and sub-mm wavelengths," *International Journal of Infrared and Millimeter waves*, vol. 3, no. 3, pp. 297–307, 1982.

[60] A. Murokh, J. Rosenzweig, and U. Happek et. al, "Coherent transition radiation diagnosis of electron beam microbunching," *Nucl. Inst. and Meth. A*, vol. 410, p. 452, 1998.

[61] D. Michalcea, "Longitudinal electron bunch diagnostics using coherent transition radiation." Vicoria Linear Collider Workshop; Presentation; 28-31 July, 2004.

[62] D. W. Rule and R. B. Fiorito, "Comparative analyst of optical-transition-radiation-based electron-beam emittance measurements for the Los Alamos Free-Electron Laser," *Nucl. Inst. and Meth. A*, vol. 296, pp. 739–743, 1990.

[63] M. Herrmann, M. Tani, K. Sakai, and R. Fukasawa, "Terahertz imaging of silicon wafers," *Journal of Applied Physics*, vol. 91, pp. 1247–1250, Feb. 2002.

[64] M. Castellano, L. C. V. A. Verzilov, A. Cianchi, G. Orlandi, and M. Geitz, "Measurements of coherent diffraction radiation and its application for bunch length diagnostics in particle accelerators," *Phys. Rev. E*, vol. 63, no. 056501-8, 2001.